Integration of Conductive Materials and SMD-Components into the FDM Printing Process for Direct Embedding of Electronic Circuits

Dissertation
zur Erlangung des akademischen Grades
Dr. rer. nat
an der Fakultät für Mathematik, Informatik und
Naturwissenschaften
der Universität Hamburg

Eingereicht beim Fachbereich Informatik
von Florens Wasserfall

Oktober 2019

Gutachter:
Prof. Dr. Jianwei Zhang
Prof. Dr. Eric MacDonald

Tag der Disputation: 27.01.2020

Abstract

Additive manufacturing has changed the way we develop and prototype things. It has opened up a new perspective to solve technical problems or sometimes just allows for a more appealing design, as fabricating complex and intricate structures does not require additional effort or machinery. Additive processes are increasingly used to actually produce parts in small lot sizes, replacing traditional manufacturing methods.

This thesis reports on the successful development of a Fused Deposition Modelling (FDM) 3D printer that combines processing of plastic and conductive materials with a pick and place system to build objects with integrated electronics in a single production step. The printer has been extended with a syringe extruder for conductive paste and a vacuum gripper; both mounted on individual micro z-stages to avoid collisions. Two cameras and a feeding system for electronic components were integrated, along with a new control software for vision aided placing of components. In addition to the description of all individual hardware solutions, the selection and characterization of suitable materials is presented.

The core contribution of this work is a combined slicing and design software to support the arrangement of printable 3D circuits inside of physical objects. The software allows to position electronic components from imported existing schematics in a preview of the tool path, which is then executed by the printer. Cavities, solid surfaces around components, and channels for conductive wires are automatically generated under consideration of important process parameters (layer thickness, extrusion width, etc.).

Based on the component positions and additional user-defined waypoints a novel routing algorithm generates collision-free 3D wire routes. The trajectories follow the object contour where possible and are optimized for the parameters of the current printer configuration. After the basic slicing step, the routing algorithm translates the contour information of all layers into a graph representation. An A*-based search algorithm is then employed to find suitable paths within that graph. The search algorithm is modified to use only eligible, i.e., printable transitions between adjacent layers.

As the electronics are mostly covered by plastic once the object is printed, testing often is not possible. The integrated camera is used to record high-resolution images of each layer automatically. A vision algorithm compares these images with the G-code to identify potential defects before the next layer is printed.

Several objects with 3D electronics have been successfully printed. Among them are two case studies for an academic research project and an industrial application.

Kurzfassung

Die additive Fertigung verändert die Art und Weise wie Dinge entworfen und entwickelt werden. Sie eröffnet ganz neue Möglichkeiten um technische Probleme zu lösen oder auch nur Dinge ansprechender zu gestalten, da keine aufwändigen zusätzlichen Arbeitsschritte und Geräte nötig sind um komplexe oder aufwändige Strukturen herzustellen. Additiv gefertigte Bauteile werden, zumindest für kleine Stückzahlen, zunehmend häufig in Endprodukten eingesetzt.

Diese Dissertation berichtet von der Entwicklung eines Fused Deposition Modelling (FDM) 3D Druckers, der sowohl Kunststoff als auch leitfähiges Material verarbeiten kann und über ein Bestückungssystem verfügt um Gegenstände mit integrierter Elektronik in einem einzelnen Produktionsschritt herzustellen. Der Drucker wurde zu diesem Zweck um einen Spritzenextruder für leitfähige Paste und einen Vakuumgreifer erweitert, die beide auf zusätzlichen Mikro-z-Achsen montiert sind um Kollisionen zu vermeiden. Zusätzlich wurden zwei Kameras und eine Ablage für elektronische Komponenten integriert, zusammen mit einer Software für das kameragestützte Positionieren der Bauteile. Neben der Beschreibung der einzelnen Hardwarekomponenten wird die Auswahl und Charakterisierung geeigneter Materialien beschrieben.

Ein zentraler Teil dieser Arbeit ist die Entwicklung einer kombinierten Slicing- und Design-Software, die bei der Anordnung druckbarer 3D Schaltungen in physischen Objekten unterstützt. Diese Software ermöglicht das räumliche Positionieren elektronischer Bauteile in einer Vorschau des Druckpfades, wie er später von der Maschine ausgeführt werde. Für die Bauteile und elektrischen Leitungen werden automatisch Aussparungen und geschlossene Oberflächen über- und unterhalb der Objekte erzeugt, dabei werden wichtige Prozessparameter wie Schichtdicke oder Extrusionsbreite berücksichtigt.

Basierend auf den Positionen der vom Benutzer platzierten Komponenten und zusätzlicher Wegpunkte generiert ein neuer Routing-Algorithmus kollisionsfreie 3D Pfade für die verbindenden Leitungen. Wo es möglich ist folgen die so erzeugten Trajektorien den vorhandenen Konturen des Objekts. Sie werden dabei für die Prozessparameter des Druckers optimiert, mit dem das Objekt gebaut wird. Nach dem Slicing-Schritt erzeugt der Routing-Algorithmus aus den Konturen der einzelnen Schichten eine Graphenrepräsentation des Objekts. Auf diesem Graphen wird anschließend ein A*-basierter Suchalgorithmus ausgeführt um geeignete Pfade für die Leitungen zu finden. Dabei werden nur solche Übergänge zwischen benachbarten Schichten berücksichtigt die auch tatsächlich druckbar sind.

Die fertig gedruckten Schaltungen sind meistens mit Kunststoff überdeckt, daher ist eine Funktionsprüfung in vielen Fällen nachträglich nicht mehr möglich. Um trotzdem eine Überprüfung durchzuführen werden nach jeder Schicht mit der im Drucker integrierten Kamera hoch auf-

lösende Bilder der Oberfläche aufgenommen. Diese Bilder werden automatisiert mit dem zu druckenden G-code abgeglichen, um potenzielle Defekte zu finden bevor die nächste Schicht gedruckt wird.

Mit der entwickelten Technik wurden erfolgreich mehrere Gegenstände mit integrierter 3D Elektronik gedruckt. Darunter zwei Fallstudien mit Objekten für ein wissenschaftliches Forschungsprojekt und eine industrielle Anwendung.

Contents

Chapter 1

Introduction

1.1 Motivation

Throughout the history of mankind, humans have created necessary, useful or just beautiful things, shaping them from raw material by removing all unwanted matter. Subtractive manufacturing has evolved from simple carving to modern, multi-axis high precision CNC machining. The opposite approach of assembling an object from very small quantities of material, deposited right into the desired shape, is a relatively young concept.

As has been the case often, the idea was first contemplated in science fiction literature. In 1945, George O. Smith's *Special Delivery* pictures the dystopian effect of a "duplicator", developed based on martian technology, disrupting the production processes of an entire interplanetary manufacturing industry within only a few weeks [A77]. The device is capable to scan an existing object and create exact copies from the recorded information, which can also be transmitted to other devices somewhere in the galaxy. The "replicator" was brought to a wider audience by the popular Star Trek TV-show, where it developed from a simple food synthesizer into a universal tool to produce, copy and recycle objects. In Neal Stephenson's *The Diamond Age* every household owns a *matter compiler* to synthesize almost everything, from food to computers from a set of basic molecules [A80]. The matter compiler draws a stream of energy and molecules from the Feed, a system of tubes, similar to public water or network supplies.

Contrary to the systems imagined in science fiction, the first actual additive manufacturing machines were not able to assemble an item atom by atom or molecule by molecule. In fact, only a single material could be used and the resolution was rather coarse.

The widely used Stereolithography (SLA) and FDM methods were mainly developed in the late 70s and 80s of the last century and patented in 1984 (SLA) and 1992 (FDM). A variety of powder based processes was developed in parallel, starting with Selective Laser Sintering (SLS) in the 1980s and followed by Selective Laser Melting (SLM) and inkjet based binder jetting in the early 1990s.

The term "3D printing" was originally used by MIT researchers for their binder jetting process, but increasingly recognized by a wider public when the RepRap project [A38] ignited a tremendous movement to build low cost, mostly FDM based 3D printers, easily available to professionals, researchers and interested hobbyists. In this thesis, "3D printing" is used in a broad sense, as synonym for different additive processes, including but not limited to binder jetting technology.

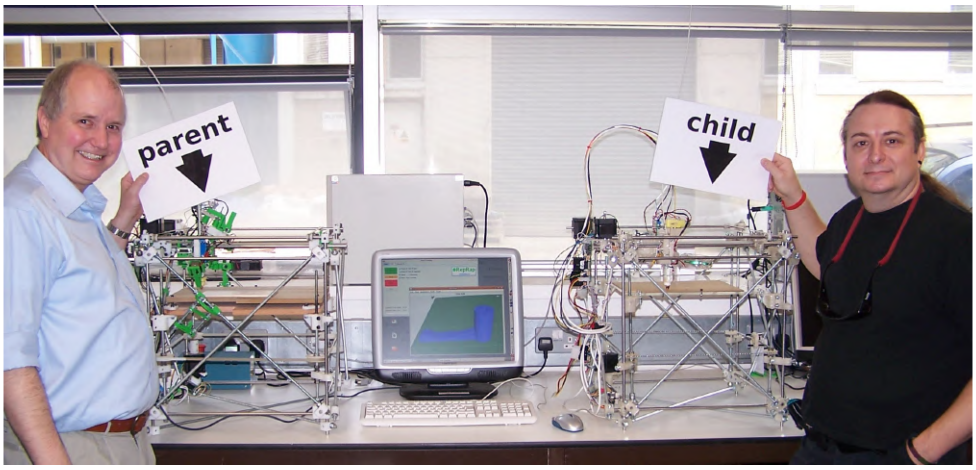

Figure 1.1 – Adrian Bowyer (left) and Vik Olliver (right) with a rapid prototyper, replicating itself by printing the required plastic parts. Image ©: TheOtherRob under GNU Free Documentation License.

The term RepRap itself is a short form of *Replicating Rapid prototyper*, which describes a machine that is essentially capable to reproduce itself. Figure 1.1 shows the first version of an FDM-printer which was assembled in 2008 from as many printed parts as possible, manufactured on the "parent" machine. Self replication, as well as many other tasks, obviously requires the combination of various materials with different properties. An important aspect for the additive manufacturing of functional parts is the integration of electric connections, motors, sensors and other components. Early research in that field was conducted in 2004 by Sells and Bowyer [A73], pursuing the idea to manufacture as many parts as possible, getting closer to the fully self replicating machine. They attempted to deposit conductive metal alloys on FDM-fabricated parts with limited success (fig. 1.2). Many technical approaches for the integration of electronics into additively manufactured parts have been successfully developed since then, an overview is given in the next chapter.

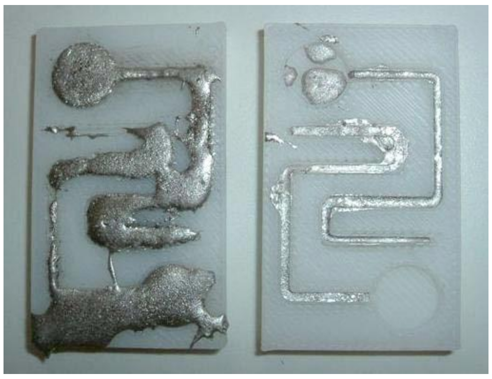

Figure 1.2 – Early experiments with electronic connections from conductive metal alloys. Reprinted image courtesy of [A73].

Besides the question of electrical conductivity, a number of other properties are essential: color, stiffness, elasticity, surface quality or transparency, to name a few important examples. Many problems are solved better by a combination of additive and established, traditional methods, e.g. by drilling a precise hole, inserting a screw or embedding an integrated microcontroller instead of printing single transistors. A major trend in recent years therefore is the integration of different manufacturing principles into a single process, usually referred to as *hybrid manufacturing* [A99]. The term hybrid manufacturing is not well defined. It is mostly used to describe a combination of different established manufacturing processes (e.g. injection moulding and milling), but also for a combination of material deposition and melting or multi material deposition with different heads in a single machine. The integration of electronic circuits during an additive manufacturing process, involving at least a structural and a conductive material and handling of electric components is considered a hybrid manufacturing process under all popular definitions.

During our own research on a printable modular robot (PMR) [A48, A49] and a 3D printed humanoid robot [A10] for the RoboCup soccer competition [B27], it became increasingly evident that the integration of electronics is a key aspect for the prototyping and rapid development of technical systems and robotics in particular. While the rapid additive manufacturing of purely mechanical parts posed no major issues thanks to increasingly maturing and affordable 3D printing technology, assembling the electronic connections and particularly integrating sensors required a significant share of the time spent for the project. The electric interfaces of each PMR module as shown in fig. 1.3 require the assembly of 16 connection points, each consisting of 5 individual components, resulting in 80 pieces per module.

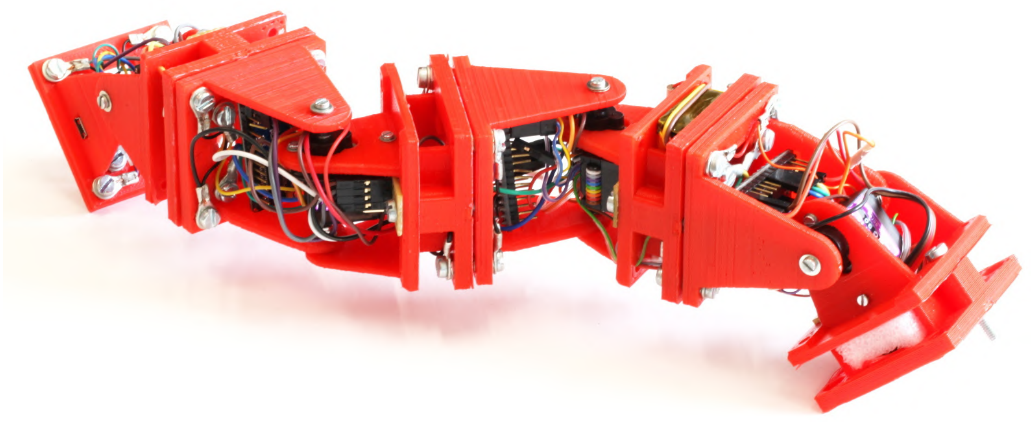

Figure 1.3 – The Printable Modular Robot, developed in an earlier project [A49]. The modules are mechanically and electrically connected via magnetic interfaces, requiring a high amount of manual assembling.

1.2 Aim of this Thesis

Although a number of research results has proven the technical feasibility of different approaches to 3D print electronics, from insertion of traditional wires [A8] to the actual additive manufacturing of an LED itself [A46], basically no commercial products are available yet. The research is mostly focused on the physical printing process itself, while the complex problem of integrating mechanic and electric designs into a single part still suffers applicable solutions. So far, most of the printed demonstrator objects have been carefully designed and prepared with a substantial amount of manual work, which is not a feasible option for broader commercial application of additively fabricated electronics.
The aim of this thesis is to create a toolchain to print an object with integrated electronics, covering all steps from design to automatic assembly of components. To achieve this, several individual developments from mechanical engineering, computer science and software development must be combined:

1. A hardware platform capable to print structural (plastic) material, conductive material and to manipulate additional components.
2. Design software to support the spatial arrangement of an electric circuit under the constraints of the manufacturing process.
3. Algorithms for routing of electric connections in 3D-space.
4. Translation of the integrated 3D-model into a sequence of machine commands.
5. Automatic placement of electronic components during the print process.
6. Quality control and verification of the build process.

The mid-term vision is an autonomous, integrated production cell, where a design can be uploaded and the entire build process is executed without human intervention. Such a system could be integrated as a very flexible part of a conventional industrial production process, but the primary intended use case is prototyping and individualized single pieces.

Given the diversity of available additive manufacturing methods, the choice of an appropriate base technique is important and has major implications on what can or cannot be achieved. Light (including laser) based processes provide very high precision and resolution, but usually require a powder bed or liquid filled basin. As a side effect, it is very difficult to combine two or more materials. Inkjet based processes also provide high resolution and are very suitable to combine multiple materials by using one cartridge per material. Unfortunately, the UV-cured material is brittle, lacks long term stability and machines are proprietary and expensive.
The FDM technology is considered to be well suited for integration of multiple materials and parts for several reasons: the surface is always flat and open during the build process, no liquids or powders are covering the workspace, interruption and resuming of the print is possible without cleaning or registration of the workpiece. FDM technology is comparably cheap and widely available, increasing the number of potential users. Both hard- and software can be purchased off the shelf, ready to use, still often distributed as open source, facilitating modifications and extensions.

1.3 Research Question and Contribution

Mechanical Engineering & Integration: How to design and operate an additive manufacturing system, that is capable of printing complex physical objects with integrated wiring and autonomous assembly of electronic components? Which materials are suitable for such a process? With regard to potential industrial automation, the entire build process is supposed to be performed without any human interaction.

3D-Electronics Design: How to combine existing mechanic Computer Aided Design (mCAD) and electronic Computer Aided Design (eCAD) approaches in such a way that the result is producible on additive manufacturing systems while preserving the intended mechanical and electrical specifications?

2D & 3D Wire Routing algorithms: How to route wires within or at the surface of arbitrary and complex 3D-Objects, constraint by limited process resolution, with a strong focus on the FDM-Process?

Process Verification: How to ensure that a circuit, fully or partly immersed in plastic, has no defects and works as intended?

1.4 Structure of the Thesis

The remaining parts of this thesis are organized as follows:

- Chapter 2 provides an overview over the fundamental methods for additive fabrication of electronics and reviews existing related work. A focus is set on the introduction of several approaches to integrate conductive traces and electronic components into different additive manufacturing processes. It also covers methods for the co-design of eCAD and mCAD for integrated 3D circuits and closes with a description of approaches for quality control and process monitoring.

- Chapter 3 covers all aspects of the hardware systems. The general architecture of the production system is explained and the two experimental printing platforms which were developed during this work are introduced. Different conductive and plastic materials, paste extruders, vacuum grippers and cameras were evaluated on a heavy CNC-gantry system. With the experience gathered in this first phase, an integrated demonstrator platform was build, based on a commercial FDM printer. All software directly running on the machine is also described in the hardware chapter, this includes the firmware, image processing for component handling and machine control and the G-code based data exchange. Finally, some remarks on calibration conclude the hardware related section.

- Chapter 4 first introduces the general functionality of slicing software, which is then extended to import schematics, place components and wire electric connections. Once the positions are set, the extrusion trajectories are iteratively re-generated with cavities for components and channels for conductive wires. It is described how solid surfaces are automatically inserted where required, to support the extrusion of liquid paste.

- Chapter 5 continues with the generation of wires but focuses on automatic finding of optimal routes within a given object shape and process parameters. First, a graph based representation of the search space is developed. The routing problem is then successively solved for the simplified 2D case within a single layer in sec. 5.2 and extended to the full 3D problem in sec. 5.3. Section 5.4 concludes with approaches to optimize the avoidance of wire collisions.
- Chapter 6 elaborates on the aspect of documentation and verification of the correctness of printed electronics. Verification during the build-process is of particular importance, as the circuits are often not accessible from the outside when the part is completed.
- In chapter 7 several printed objects are presented as case studies to apply and evaluate the methods developed in this work and to identify promising use cases. Furthermore, the runtime performance of the routing algorithms is analyzed to locate inefficient code sections, slowing down the execution.
- Chapter 8 closes the thesis by summarizing the scientific contributions. It also states the limitations of the current state of work and gives an outlook onto upcoming future research questions.

1.5 Related Publications

During the 5 years of this work, a number of publications were contributed to different conferences and journals, most of them jointly with colleagues, and at least partly related to the core topic of this thesis: [A48], [A49], [A10], [A95], [A94], [A11], [A3].

The following list only includes those publications which form the basis of this document. In these publications, the first author was responsible for problem definition, solution finding, programming and visualization. He initialized, implemented and steered discussion and experiments.

- Florens Wasserfall. “Embedding of SMD populated circuits into FDM printed objects”. In: *Proceedings of the 26th International Solid Freeform Fabrication Symposium*. Austin, 2015, pp. 180–189.

  This first paper reports on the basic experiments to integrate all required hardware components into a single manufacturing machine. The first demonstrator platform was introduced, combining a 3D printer for plastic and conductive material and a pick and place unit. The paper also includes the first printed objects (Chapter 3).

- Florens Wasserfall, Daniel Ahlers, Norman Hendrich, and Jianwei Zhang. “3D-Printable Electronics - Integration of SMD Placement and Wiring into the Slicing Process for FDM Fabrication”. In: *Proceedings of the 27th International Solid Freeform Fabrication Symposium*. Austin, 2016, pp. 1826–1837.

  The second paper focuses on combined eCAD and mCAD design. It introduces the concept of integrating electronic component placing and wire routing into the slicing software, which then automates the generation of proper tool paths with appropriate cavities and channels (Chapter 4).

- Florens Wasserfall. “Topology-Aware Routing of Electric Wires in FDM-Printed Objects”. In: *Proceedings of the 29th International Solid Freeform Fabrication Symposium*. Austin, 2018, pp. 1649–1659.

  This publication dives further into the details of the electronic slicing software and describes an approach for semi-automatic wire routing in a printed 3D-object (Chapter 5).

- Florens Wasserfall, Norman Hendrich, and Daniel Ahlers. “Optical In-Situ Verification of 3D-Printed Electronic Circuits”. In: *Proceedings of the 15th IEEE Conference on Automation Science and Engineering (CASE)*. Vancouver, 2019, pp. 1302–1307.

  This paper covers the problem of quality control and process verification. The cameras originally intended for the pick and place system were used to record high resolution images of each printed layer for documentation. In a second step, an image processing approach for automatic comparison of the G-code and the printed layer is introduced. The build process can be automatically interrupted upon defect detection (Chapter 7).

Chapter 2

State of the Art in Printed Electronics

The term *printed electronics* comprises a wide field of techniques and materials which are incorporated to produce electrical connections by selectively adding conductive material to a substrate or to the surface of an object.

The number of possible combinations of additive manufacturing and electronic-printing process is quite high, but not each of those combination is possible. For example, conductive filament cannot be processed with an inkjet printer. Therefore, an overview over relevant additive manufacturing processes is given first. Followed by a number of printing approaches for conductive material which are then individually related to suitable manufacturing principles. An early review on the combination of additive manufacturing and *direct write* of electronics is given in [A64]. More recent and broader surveys are provided in [A60] and [A20].

2.1 Additive Manufacturing

Several additive manufacturing methods are good candidates for an integration of 3D electronics. Polymer based processes are generally preferred as the plastic serves as good insulating substrate material. A more in-depth overview of available additive processes, how they work and their advantages and drawbacks is given in [A25].

2.1.1 Fused Deposition Modelling

Fused Deposition Modelling (FDM) or Fused Filament Fabrication (FFF) utilizes plastic filament which is pushed by mechanical force through a heated extrusion nozzle. The nozzle is typically mounted on a computer controlled 3-axis gantry system to dispense the molten plastic strand. First it follows the shape of the object to fabricate the correct contour and then filling the interior line by line or following an infill pattern. The object is built layer by layer. The remaining heat in the plastic material after extrusion is sufficient to partially (re-)melt and interlink adjacent layers. Multi-extruder setups allow the combination of different materials, e.g. for support structures or colors. The horizontal resolution is limited by the extrusion width, which is determined by the nozzle diameter and the fact that extrusions should follow continuous planar trajectories to achieve proper extrusion flow. Small isolated amounts of extruded material often result in very poor quality, e.g. when building peaks or pillars. In the vertical direction the resolution is limited by the minimum achievable layer thickness which varies between different printer models and extruders, but is often found to be between 0.1 mm and 0.2 mm. Due to the discretization into layers, non-vertical object surfaces suffer from *stairstepping*. The effect increases for almost horizontal surfaces. A detailed analysis is given in our previous work [A95].

2.1.2 Stereolithography

Stereolithography (SLA) is based on photopolymerization of a liquid resin. A computer controlled UV laser or Digital Light Processing (DLP) selectively transforms the fluid base monomer into a solid polymer to produce a single layer by projecting the surface of the current layer onto the resin. The object is then submersed into the resin again to provide a thin film of liquid for the next layer. A wiper is used to achieve a smooth, uniform monomer layer. Overhanging geometries are possible but support structures are often required as the cured plastic material is still slightly flexible. Support structures must be removed mechanically after printing. Post-curing with UV-light is possible to improve stability. The resolution and accuracy of SLA is high due to the use of light. However, the resulting objects are UV-sensitive, brittle and suffer from low long term stability.

2.1.3 Powder Bed Fusion and Binder Jetting

Several additive processes are based on powder material (polymer, metal, ceramic, gypsum) and use energy or binder deposition to locally solidify the powder. A chamber is filled with the powder base material and the surface is smoothed by a roller. Laser or electron beam energy sources are utilized to selectively melt and solidify the powder. Alternatively a binder material is jetted into the powder bed to stick the material together. The build chamber is then lowered and re-filled with base material. Support structures are not required, since the object is fully surrounded by powder material which allows to build true free-form objects. Powder based processes are typically used for professional industry purposes as they are expensive but provide very high resolution and stability.

2.1.4 Material Jetting

For material jetting, a high number of photopolymer droplets are applied on a flat surface with inkjet printheads and cured with a UV light source. The process is repeated layer by layer to form the 3D object. Wax-based support material is used to produce overhanging geometries. The support material can be removed in a post-process by heating the object to a temperature above the melting point of wax and below the melting temperature of the polymer material.

2.2 Wire Generation

Several approaches for the digital generation of freeform wires on the surface or inside of objects were evaluated in the past two decades. In the following, a short description of the most important methods is given to provide a first overview. More details are provided in the corresponding sections 2.2.1 to 2.2.4, where the integration of wires and electronic components into different additive processes is reviewed in detail.

Direct Writing or paste extrusion is a generic term for the application of a liquid (conductive) material with a dispensing system. The material is stored in a reservoir and pushed through a nozzle or hollow needle by force applied through pressurized air or a screw driven plunger. The dispenser can be mounted within a 3D-printer, on an individual gantry system or operated by hand. A conductive line is drawn by moving the dispenser along a surface. Typical trace widths are $0.1\,\mathrm{mm}$ to $1.0\,\mathrm{mm}$. Printing is generally possible on every chemically suitable, smooth surface, e.g. plastic, glass, metal. This explicitly includes most additively produced objects, with surface roughness being the main limiting factor.

Conductive Filament can be directly processed with an FDM-printer, replacing the common plastic filament. The conductivity is achieved by mixing conductive particles (carbon, copper, silver) into the plastic before the filament is formed, or by using low temperature alloy to form a wire, which replaces the plastic filament. A main advantage of conductive filament is the direct printability with existing standard machinery. However, the conductivity of plastic based filaments is very low and metal based filaments have a highly abrasive effect on the nozzle.

Wire Embedding is a technique where traditional copper wires are heated and directly submerged into the surface of a plastic object. The temperature can be controlled by driving the wire through a heated nozzle, by transmission of energy via ultrasonic waves or by running an electric current directly through the copper wire. After submersion, the wires are insulated by the surrounding plastic. The primary challenges with wire embedding are clean cutting of the wire and connection to other wires and electronic components. In addition, routing poses a relevant problem, as a wire should always be deposited in a single trajectory, from one endpoint to the other.

Ink-Jetting was originally invented for graphical applications to print text or images on paper. In recent years, an increasing number of materials have been processed with inkjet printheads, including a variety of conductive inks. Droplets are generated by applying a pulse of pressure onto a liquid, ejecting a small quantity through an orifice. The required force is generated either by a resistive heater or a piezoelectric actuator, the latter being preferred for most applications with conductive inks. The inkjet process imposes several requirements on the ink properties; the viscosity must be very low to not attenuate the pressure pulse. At the same time the fluid must contain a certain amount of solid particles to be conductive which has a contrary effect on viscosity and increases the risk of clogging. Eventually the ink must be compatible with the substrate it is printed on.

Aeorosol-Jetting was developed by Optomec Inc. under DARPA contract [B22]. A conductive ink is atomized into an aerosol of droplets and carried by a gas flow through a deposition head. The particle laden gas is then focused in the nozzle by a second sheath gas surrounding the aerosol [A33]. A shutter interrupts the gas flow if required. Aerosol jetting allows to create very fine wires ($25\,\mu\mathrm{m}$).

Metallization is the fundamental technique of (selectively) plating the surface of an object with metal. Metallization is widely used for the production of Molded Interconnect Device (MID), where circuits are directly applied to the surfaces of injection molded plastic parts. Regions for metallization are traditionally masked by two-component molding or laser activation of the surface. A detailed overview of this field is given by [A23]. Recently, attempts have been made to transfer the metallization approach to additive manufactured parts. Direct laser structuring is possible after coating with a special paint or by using functionalized plastic powders, containing metal additives for the additive process [A7].

The integration of circuits is generally possible during the additive manufacturing process, when the interior of the half-finished object is still accessible, or after the build process. The second option only allows deposition on the surface or filling of tubes. Integration during the print process often requires removal of powder or resin material and a subsequent registration step. Most approaches for the integration of electronics were reported to utilize either FDM or SLA as base process. The focus is therefore set on those two methods, the first one being used throughout the remaining thesis.

2.2.1 Integration with FDM

The FDM process is well suited for the integration of circuits for several reasons and has thus received attention from many researchers. All common plastic base-materials are good insulators. The print surface is clean and not covered by powder or liquids and the required equipment is both available and affordable. Many machines support extrusion of two or more different materials. Low resolution and reliability are the most important disadvantages. Typical extrusion widths of $0.2\,\mathrm{mm}$ – SI0.5mm induce a significant surface roughness and limit the feature size of electronic connections.

In 2004, Sells and Bowyer conducted a series of experiments with a low melting point, eutectic alloy, complementing their efforts to build a self replicating machine [A73]. Wood's metal ($Bi50Pb27Sn13Cd10$) has a melting point of approximately $70\,^{\circ}\mathrm{C}$ and was applied into FDM-printed channels, first by casting and in a subsequent experiment dispensed from a syringe, mounted into an air-heated hot-jacket. Their experiments resulted in the successful fabrication of a simple mobile robot shown in fig. 2.1. However, the high surface tension of molten metal was reported to often prevent successful material distribution and the minimum achievable trace width was above $1.2\,\mathrm{mm}$.

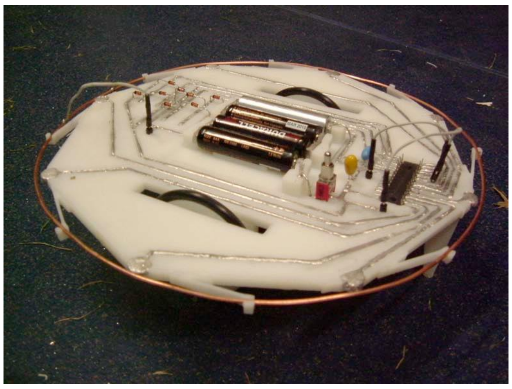

Figure 2.1 – Prototype of a printed, mobile robot. Electrical connections are realized with low-temperature metal alloy. All circuits were manually dispensed and assembled. Reprinted image courtesy of [A73].

Periard et al. used a Fab@Home system to deposit two different types of silicone with a syringe where one of them is loaded with silver particles. The Fab@Home printer originally was designed as a purely syringe based system, using different types of silicone therefore integrates very well into the process. They fabricated a 555-timer based LED flashing circuit, which is a simple demonstrator frequently used by several groups. The reported resistivity of $\rho = 5.0 \times 10^{-6}\,\Omega\,\mathrm{m}$ is surprisingly low, compared to the significantly higher resistivity of typical silver inks.

Leigh et al. used an unmodified printer for standard filaments and produced a conductive filament termed *carbomorph* by adding a quantity of 15wt% of carbon black to PolyCaproLactone (PCL) base material [A54]. The reported high resistivity of $\rho = 9.0 \times 10^{-2}\,\Omega\,\mathrm{m}$ prohibits an application as wire replacement in most cases, but the material exhibits piezoresistive behavior which potentially allows fabrication of embedded deformation and force sensors. The authors also state the materials suitability to print capacitive touch sensors. Kwok et al. proposed a similar formulation of carbon filled Polypropylene (PP) [A50], but reported a resistivity of only $\rho = 5.0 \times 10^{-3}\,\Omega\,\mathrm{m}$.
Several carbon filled, conductive filaments have become commercially available in recent years. The resistivity was investigated for raw filament [A24] and for printed objects [A79] where the layered structure, infill pattern and temperature impose a certain anisotropic characteristic. The resistivity was found to be between $1.0 \times 10^{-1}\,\Omega\,\mathrm{m}$ and $4.5 \times 10^{-1}\,\Omega\,\mathrm{m}$ for the popular Protopasta conductive PLA filament [B25]. Multi3D also offers a metal-polymer composite filament Electrifi [B18] with a claimed resistivity of only $6.0 \times 10^{-5}\,\Omega\,\mathrm{m}$.
An interesting use-case for conductive filament was reported by Iyer et al. who printed an antenna which is mechanically modulated e.g. by pressing a switch [A36]. They use the backscatter signal to passively transmit a short data packet with a standard Wi-Fi device.
A different approach to conductive filament was taken by Andersen et al. [A4] who fabricated printable filaments from two non-eutectic, low-melting alloys: Sn70Bi30 and Sn66Bi30Ag4 with melting points of approximately $170\,^{\circ}\mathrm{C}$ and $190\,^{\circ}\mathrm{C}$ and resistivity of $2.6 \times 10^{-7}\,\Omega\,\mathrm{m}$ and $2.3 \times 10^{-7}\,\Omega\,\mathrm{m}$ respectively. The alloy filament solidifies quickly after leaving the heated nozzle, resulting in extrusion characteristics similar to common plastic materials. The nozzle geometry and thermal conductivity have a strong effect on the printing quality, clogging and considerable erosion of the nozzle tip require the usage of suitable, hardened extruders.

The issue of low conductivity was addressed by a series of experiments to integrate copper wires during or after the print process. Bayless et al. conducted an early feasibility study, where they mounted a servo-actuated mechanical pencil with a heated tip onto a RepRap printer [A8]. A $0.5\,\mathrm{mm}$ copper wire is fed as a continuous strand through the pencil, heated at the tip and submerged into the plastic surface. The wire is cut by a solenoid-actuated shearing mechanism. The authors intended to utilize wires as both structural element for mechanical reinforcement (e.g. printed hinge) and conductive connection (e.g. spool). Figure 2.2, left shows a spiral pattern manufactured with the system.
Espalin et al. developed two other methods to heat the wire: with a high-power, ultrasonic horn or with a Joule heating method where an electric current is passed through the wire [A19]. The general idea is described in two patents [A97] and [A96]. A YAG laser microwelding system is used to produce solderless joints between wires and electronic components as demonstrated in fig. 2.2, right. Reliable junctions of wires and connections of wires with electronic components

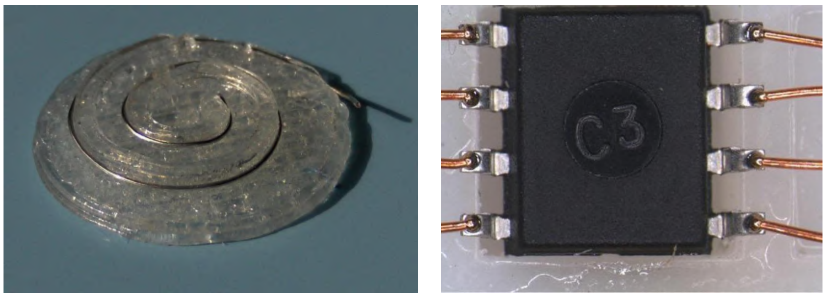

Figure 2.2 – **Left**: a wire embedded into a printed plastic object in a spiral pattern. **Right**: laser micro welded connection to connect copper wires and component pins. Reprinted images courtesy of [A8] and [A19].

generally pose a difficulty, as the molten plastic tends to form an insulating film around the copper. Kim et al. introduced a system where the wire embedding mechanism is mounted to a 3-axis CNC-controlled gantry stage and a previously printed workpiece can be rotated around one axis to embed wires at the surface of curved freeform-objects [A42]. They focus on the trajectory planning for continuous wire integration.

Gutierrez et al. performed first experiments with Ercon 1660 conductive ink, directly dispensed on the surface of FDM-printed ULTEM material in 2011 [A29]. They considered to use this approach for the production of a CubeSat and therefore performed basic compatibility and outgassing tests. The direct application of ink on an FDM-printed surface turned out to be limited in terms of reliability and accuracy due to the high surface roughness and feature size achievable with extruded plastic. To mitigate this issue, an additional subtractive processing step was introduced. Channels and cavities were cut into the printed surface with a micromachining device, achieving very high accuracy. The effort culminated in a combined manufacturing cell, termed the multi^{3D} system [A19] which was also used to produce components for the CubeSat project [A74]. Two Stratasys FDM printers and a gantry are arranged around an industrial robot arm, connecting the individual processes by conveying the workpiece between the stations [A60]. One printer produces the first layers. The process is then interrupted, the buildplate moved to the gantry for precise machining of the channels and application of conductive ink. It is then returned back to the printer where the next layers are added and so forth.

A first commercial approach was taken by the Harvard-based startup Voxel8 [B13][1], which started distribution of a low-cost printer, combining FDM with a pneumatic ink dispenser in early 2015. Despite a broad resonance among media and researchers, the company ceased development and support of the printer in 2017 and currently works on an industrial process for the multi-material fabrication of footwear.

Goh et al. published a study where they compared a combination of FDM and Stratasys inkjet based MultiJet technology with direct write application of carbon and silver based conductive inks [A28]. The objects are partly printed, moved to a 3-axis dispensing system and back to the printer to continue the additive process. Registration after returning to the printer was reported to be effortless with the FDM due to an existing fixture at the printbed, but raised issues with

[1]This reference points to the current Website of Voxel8 Inc., the original domain was https://voxel8.co

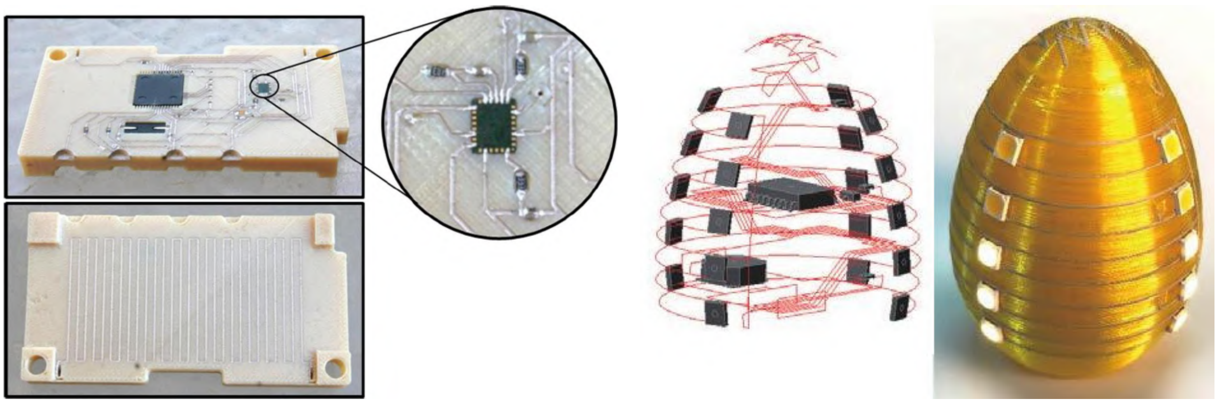

Figure 2.3 – **Left**: FDM-printed CubeSat module. Channels and cavities are CNC milled. **Right**: FDM-printed egg-timer, wires and components are assembled by a 5-axis system aligned with the freeform surface. Reprinted images courtesy of [A19] and [A5].

the MultiJet system. The transfer steps and assembly of electronic components were executed manually. A simple LED-flashlight was fabricated with the FDM-printer as demonstration object and the internal structure analyzed with X-ray CT.

One of the central promises of 3D-printed electronics is the capability to arrange circuits and components not only at arbitrary positions, but also rotated to fulfill technical requirements (e.g. orientation of a magnetic flux sensor) or to be aligned with a surface (e.g. LED-interfaces). To achieve this in an integrated system, additional degrees of freedom are required for the application of wires and component placement. Ankenbrand et al. [A5] used a fully integrated 5-axis system, combining an FDM extruder for structural material, a piezojet dispenser for contactless application of conductive ink and a vacuum gripper for camera assisted pick and placing of electronic components, manufactured by Neotech AMT [B19]. A partly integrated CAD/CAM and slicing software was used to generate the G-Code commands to control the machine. They successfully demonstrated the fabrication of an egg shaped egg-timer, integrating 20 LEDs and a PIC16F627 microcontroller inside and on the surface of the object, claiming that the entire process was executed automatically.

Li et al. proposed a selective electroless plating method, where the object is built with a dual-material FDM printer, using PolyEthylene Terephthalate Glycol (PETG) as the base material and Acrylonitrile Butadiene Styrene (ABS) for electric connections [A55]. The printed object is etched to increase the surface roughness of the ABS areas and then electrolessly plated, leaving a metallic, conductive film on the surface. SMD components were mounted to the metallized surface with silver adhesive paste.

2.2.2 Integration with SLA

Compared to FDM, resin based approaches provide better resolution and dimensional accuracy, but application of conductive material is only possible after a cleaning step and the objects generally suffer from low long-term stability.

De Nava et al. demonstrated the fabrication of a three-axis magnetic flux sensor system, where the hall effect sensors are required to be arranged in orthogonal orientations [A16]. They fabricated the body with SLA and used direct write dispensing of conductive ink into fabricated channels. Wire collisions were avoided by under-arch tunnels, which were later pumped with conductive inks. The same approach was later used to prototype a helmet insert for injury detection [A61] and parts for the aforementioned CubeSat project [A29].

The integration of SLA and direct write was described in detail by Lopes et al. [A56]. They combine a stereolithography printer with a micro-dispensing system, mounted on a three-axis linear positioning system in a single housing. The build process is partly automated. The layer-wise SLA fabrication is stopped at some point, the vat is lowered and the surface is cleaned to remove remaining uncured resin. Components are then placed manually, wires are created by the automatic dispensing system. Accurate registration of the dispensing- and SLA-unit is required for successful integration. The SLA laser is used for in-situ curing of the conductive ink to avoid contamination of the resin with uncured paste. The vat is then refilled and the build process continues.

A similar process integration was described by Wasley et al. [A88]. They also use a DLP-based SLA process which is interrupted for direct writing of electric connections with a second positioning system and manual placement of Surface Mounted Device (SMD) components. Surface cleaning is done with an ultrasonic bath to remove excess liquid resin from the surface and achieve good bonding of the conductive ink. Circuits are arranged in thick “slabs” to reduce the number of interruptions. Channels and cavities are then filled with photopolymer resin and selectively cured. Interconnects between the electronic layers are established by stacking small amounts of conductive material to form pillars. They also demonstrate a technique for flip chip packaging of fine pitch components, incorporating an abrasive polishing step to remove excess conductive material.

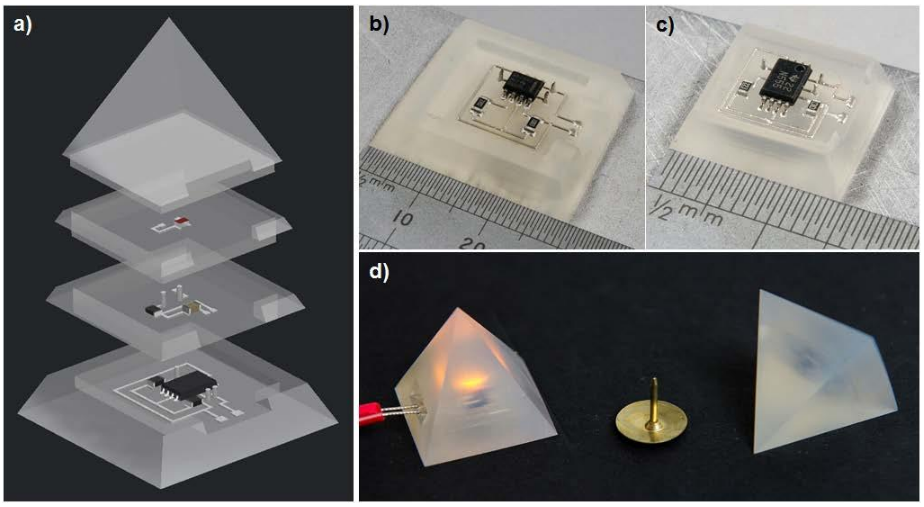

Figure 2.4 – Iterative integration of SLA and direct write process for conductive circuits. Reprinted image courtesy of [A88].

MacDonald et al. published a study comparing SLA-based prototyping of structural electronics with traditional molding process, focusing on product development and time to market [A59]. They developed and manufactured three iterative versions of a six-sided gaming die with integrated accelerometer and LEDs at the surface to indicate the result of a roll, the final version is illustrated in fig. 2.6. The dice were fabricated with both additive and traditional manufacturing. The former allowing to build a prototype within 30 hours compared to a minimum of 120 hours for an injection-molded version, integrating a flex Printed Circuit Board (PCB).

2.2.3 Integration with Powder-Based Processes

Hörber et al. performed a series of experiments to integrate circuits and components into a powder-based binder jetting process [A34]. They mounted an additional vacuum needle into the machine to selectively remove powder material to create cavities. The same system was also used to pick and place components. Conductive traces were printed during the build process with Isotropic Conductive Adhesive (ICA), applied with a pneumatic dispenser directly onto the powder bed and with Optomecs aerosol jetting technology at the surface of the finished part.
The same setup was used by Glasschröder et al. to also insert mechanical components during the print process to increase the tensile strength of AM-manufactured parts [A27]. The vacuum system was used to create cavities to insert nuts and to form channels to embed different types of fibers.

A very detailed description of all mechanical aspects for the integration of circuits into a binder-jet based powder process is provided in Glasschröders PhD thesis [A26]. The entire process was analyzed and successfully implemented, resulting in a first demonstrator object: a gripper which contains a a printed strain gauge to measure the force applied during a grasp.

Hossain et al. demonstrated the integration of sensors into metal parts to be utilized in very harsh conditions, e.g. inside of a combustion engine [A35]. They used Electron Beam Melting (EBM) to manufacture a part from Ti-6Al-4V material in a “stop and go” process, where the print is interrupted to embed ceramic piezo sensors and then resumed.

2.2.4 Material Jetting

Direct jetting bears the potential to combine several different functional materials with a high resolution, resulting in densely integrated functional objects [A13]. For several years the research focus was primarily on formulation of suitable inks, droplet formation and behavior on a substrate. A comprehensive review on the combination of inkjet printing and additive manufacturing is given by [A82].

Smith et al. published an early study where they used a single nozzle Drop On Demand (DOD) inkjet printer to deposit silver-containing organometallic ink onto flat surfaces of different materials [A78]. The tracks were cured at 150 °C, a mean resistance of $162\,\Omega/m$ was measured, which equates to a surprisingly low resistivity of $\rho = 2.5 \times 10^{-8}\,\Omega\,m$.

A basic study on drop-on-demand jetting of high viscosity conductive inks was published by Ledesma-Fernandez and Hauge [A52]. A jetting valve is used to deposit high viscosity, carbon laden inks together with UV-curable material. They successfully demonstrate the integration of a single LED into an otherwise inkjet printed object, composed of structural UV-curable resin and conductive carbon paste.

2.3 3D-Design Concepts

This section gives an overview of different approaches to design electronic circuits for additive manufacturing processes. While significant progress has been made in the field of hybrid manufacturing and the physical printing technology is maturing, the important aspect of efficient object- and electronics co-design has not received the same amount of attention yet. In 2014, MacDonald et al. [A59] described the situation as:

> "[..] the component placement and routing for 3D printed designs has been done manually in 3D space using mechanical engineering CAD software like SolidWorks without the inherent features for electronics functionality. This lack of software support has relegated 3D printing of electronic devices to relatively simple circuits as routing and placement has been done by hand."

So far, most of the printed 3D electronics demonstrator objects have been carefully designed and prepared with a substantial amount of manual work. The example in fig. 2.5 shows an approach where two solid models have been designed, one volume for the structural plastic (blue), the other representing the conductive material (yellow). The same approach was also used to create early test objects for this thesis as detailed in sec. 7.2.1 (fig. 7.2) and [A90].

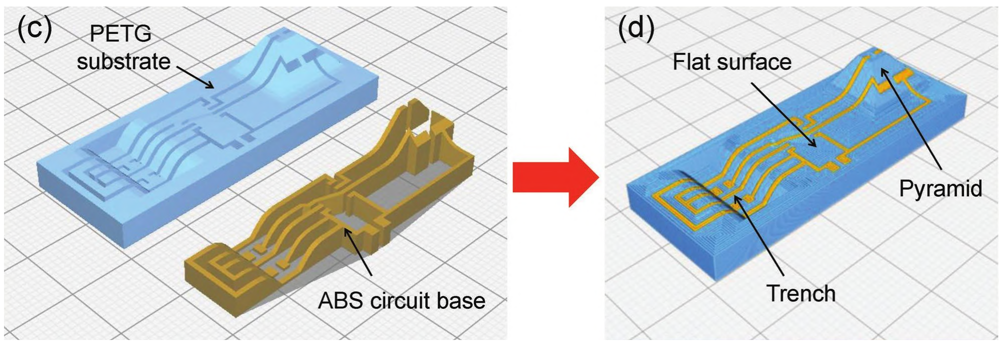

Figure 2.5 – Simple approach to design 3D printable electronics. Two volume models are manually created, one representing the structural plastic (blue) and one for the conductive material (yellow). Both models are merged into a multi-model file and printed, in this case with a dual extrusion FDM printer. Reprinted image courtesy of [A55].

Sarikk et al. generated a Drawing Exchange Format (DXF) file from an EAGLE [B12] PCB layout and used OpenScad [B16] to render a 3D model which could be directly printed, but is limited to a single layer [A70]. Panhalkar et al. proposed a file format for the additive manufacturing of electronics [A62]. They use a CSG-style tree representation to combine geometric and electric information. An electrical tree holds information about each component, including electrical properties and position. Each node in this tree references to an additional geometric tree which describes the shape of the component. The electrical tree is queried during the slicing process to identify components which intersect the current layer. The contour polygon of each affected component is then generated from the geometrical tree and removed from the current layer to create matching cavities. The aspect of wiring the electronic components is not addressed.

With the development of conductive ink, which can be used with off-the-shelf inkjet printers and coated paper [A40], several solutions for the problem of routing planar circuits printed on sheet material were developed.
PaperPulse [A65] is a toolset for rapid prototyping of paper based interactive user interfaces. It implements an A* based routing algorithm to avoid intersection with other conductive traces and obstacles on the paper, e.g. printed instructions. When the circuit is non-planar, conductive tape is incorporated to form zero-ohm bridges.
The LightTrace auto-router [A84] was developed to support the design of LED based applications on paper-based circuits. The core functionality is balancing the LED brightness by achieving equal current flow through each diode and compensating for the resistance of the inkjet printed patterns. The auto-routing algorithm is based on the traveling salesman problem, finding the shortest connecting pattern while minimizing trace intersections. To achieve this, it varies the trace width to modulate the resistance and inserts meandering patterns if the trace would become unreasonable thin. LightTrace is implemented as an Adobe Illustrator extension.

Several approaches to integrate conductive elements into FDM fabricated objects have been proposed from a user interface perspective, mostly to turn certain areas of the surface into touch sensors. Savage et al. propose a general technique to support the generation of internal pipes within generic 3D models [A71]. The pipes can be filled by injecting conductive material after the print is finished, but can also be used for other purposes, e.g. air flow or housing liquids. They implemented PipeDream in C++ as a Meshmixer extension. The tool uses A* based routing and physical rod simulation to generate smooth curvatures while avoiding contact to the object surface and other pipes. However, it is not suitable for fine structures as would be required to contact multi-pin SMD components.
Swensen et al. also introduced a framework for automatic tube insertion, but their algorithm is specifically tuned to generate hollow channels which are later filled with low temperature melting metal alloy [A83]. A Matlab script automatically inserts a series of tubes into a tesselated 3D object, using an EAGLE board layout file (.brd) as input. The tube dimensions are optimized such that the friction is compensated. This allows the pumping of liquid conductive alloy into the channels from a single entry point which then reaches every endpoint of the system at the same moment. Through-hole electronic components can be inserted into the liquid material before it solidifies, ideally by inserting the pins into the tubes before the injection.
Schmitz et al published Capricate, a tool to alleviate the integration of touch sensitive surfaces into existing 3D models [A72]. The user defines a region at the surface which is turned into a capacitive touch sensor by converting a layer of the original object into a second mesh, representing the conductive material. In a second step, the conductive area can be connected via an A* based routing algorithm either to a standalone capacitive touch controller or to the lower surface of the object, where the signal is forwarded onto a smartphone or tablet screen.

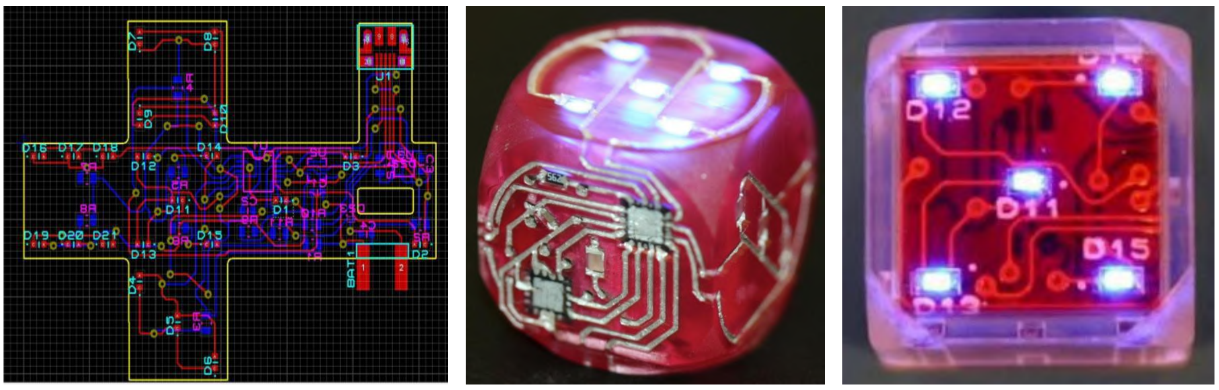

Figure 2.6 – Development of a gaming die. **Left**: PCB circuit layout to be imposed on the surface of additively manufactured prototype (**center**), compared with a version produce with conventional injection molding and embedded circuit boards (**right**). Reprinted images courtesy of [A59].

The integration of complex high resolution electronics certainly requires a design process more dedicated to the parameters and characteristics of the manufacturing technique involved, and should incorporate as many existing solutions as possible. MacDonald et al. proposed to use common 2D Printed Circuit Board (PCB) layouting software to prepare component arrangement and net routing [A59]. In a second step, they wrap or fold the result around the surface of simple objects. Figure 2.6 illustrates how a planar circuit layout is wrapped around the six sides of a gaming die. While this approach incorporates most of the advantages of well developed eCAD software, it is limited to simple geometric volumes and does not utilize the inside of objects, meaning that all connection are running along the surface.

In 2015, Autodesk in cooperation with Voxel8 launched Project Wire, a combination of a web-based CAD-modeler with support for some predefined electronic components and a slicing tool [B1]. Conductive traces were represented as a series of “boxes”, their thickness matching the layer thickness of the object, and generated by a sequence of mouse clicks. Figure 2.7 shows a screenshot of the user interface. The final design was exported as a multi-material model, represented by two tesselated objects. It was converted into G-code by a custom slicing tool which translated the conductive extrusions into combined axis and PWM commands to control the pressure driven ink dispenser. The effort was stopped and the project has been abandoned at the end of 2017, apparently due to economic reasons.

Baily et al. proposed a concept to integrate component placement and wire routing for the wire embedding process into both, the mCAD and slicing software [A6]. They use Dassault’s SolidWorks for CAD modeling and Ultimaker’s Cura as slicing tool. Both were extended with custom plug-ins to provide the additional functionality. The electronics specification is imported from an EAGLE schematic into SolidWorks, where 3D representations of the components are rendered and cut out from the object to form cavities. Electrical connections are then routed by creating a “3D sketch” and exported into an auxiliary DXF file. The generation of channels is not required, as the wires are thermally submerged into the plastic surface. In a second step, the object is imported into the Cura software as an Surface Tesselation Language or Standard Triangulation Language (STL) file, including the cavities, where a second plug-in generates the trajectories for wire embedding from the DXF file. The orientation of the wire embedding tool

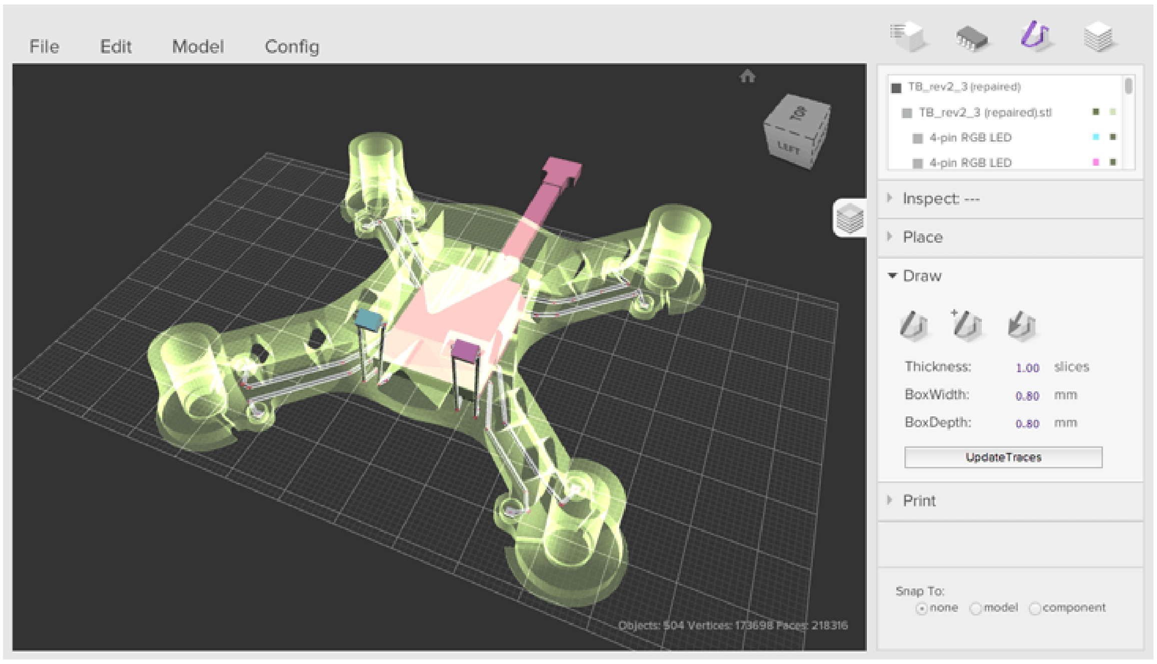

Figure 2.7 – Screenshot of Autodesk's project wire. The software allowed combined mCAD and eCAD co-design for a limited number of included electronic components and manually routed electric connections.

with respect to the moving direction of the printhead is important for this step. The combined G-code is then executed by a modified FDM printer. The print process is interrupted at the layer containing the circuit to allow manual component insertion and joining of wires and component pins and then continued to fully encapsulate the circuit. The approach is currently limited to planar circuits within a single layer.

Monolithic solutions are available as commercial design software for the field of 3D Molded Interconnect Devices (MIDs). Figure 2.8 shows screenshots of Nextra [A47], [B9] and Target3001! [B8]. Both products are proprietary eCAD layout software solutions with a focus on electromechanical systems. A mechanical model can be imported to place components and route wires on the physical surface. Embedding them into the object and 3D collision avoidance of wires is not supported as it is not possible to produce such structures with the molding process. Additive manufacturing of devices are not supported at all.

2.4 Process Monitoring

Limited reliability, process repeatability and the resulting significant shape deviations of additive manufactured parts still are a limiting factor, hindering a broader use in fields with high requirements on quality and reliability, e.g. medical or automotive applications. Recently, several attempts have been made to quantify and improve the quality of printed parts. This can be achieved by post-process qualification of the finished part, but additive methods also offer the unique opportunity to monitor during the build process, recording data from the inside of the part.

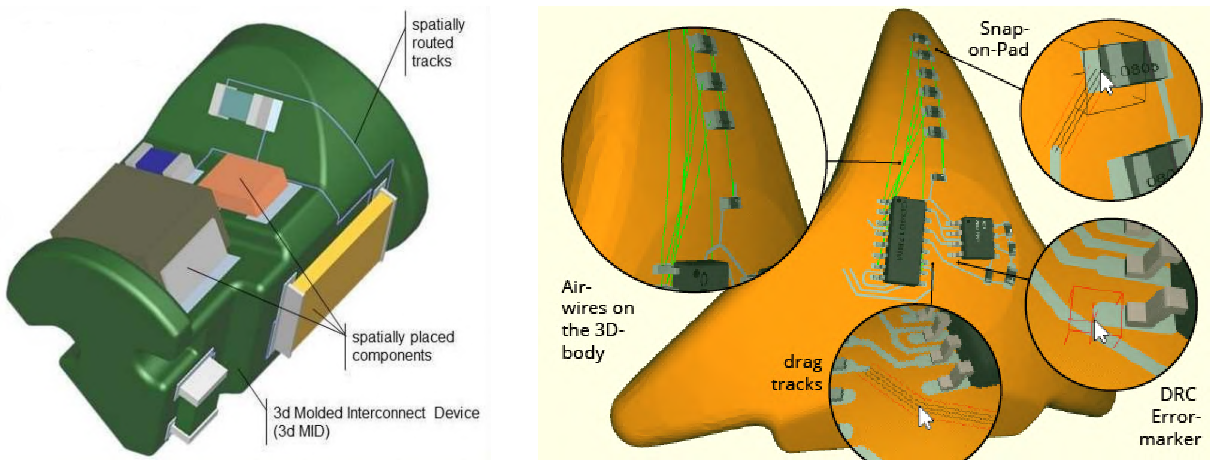

Figure 2.8 – Screenshot of Mecadtron's Nextra® [B9] (**left**) and IBFriedrich's Target3001!® [B8] (**right**) MID module. Components are placed aligned to the surface of an imported 3D-object and subsequently wired.

3D printed electronics are even more prone to defects. The mechanical complexity increases due to integration of multiple materials and processing steps, while at the same time even minor cracks or unwanted short connections in the delicate conductive traces cause complete failure, rendering the entire part useless. Traditional testing of electronics by contacting and measuring the circuit at several points is impossible, if it is enclosed by the structural plastic material. Therefore, quality monitoring during the build process is essential.

The field of quality management and assessment is very broad and a complete discussion is far beyond the scope of this thesis. In the following, a selection of research results is reviewed which are related to in-situ monitoring of additive manufacturing processes and printed electronics.

A simple and straightforward way of quality control is evaluation of process parameters, e.g. temperature or material flow. Kim et al. implemented a system to track the filament feed rate for FDM processes by measuring and analyzing the extruder motor current [A43]. Nozzle clogging, empty filament spools and underextrusion can be detected to automatically pause the printjob and trigger an alarm.

Straub arranged a set of five cameras around an FDM printer to compare the current print to pre-recorded images of a successful run [A81]. The photos are compared on a pixel-by-pixel basis, the print is stopped if the accumulated difference exceeds a certain threshold. This solution is only suitable if more than one piece is produced and requires careful control of the environment inside of the printer.

A similar approach was taken by Delli and Chang who mounted a single camera with top-down sight to the printer, in a position where the printbed can be recorded with a single image [A17]. They define a number of check points where images are taken during the process. Each image is divided into a 4x4 matrix, average RGB values are calculated for each tile and compared to pre-recorded images from a successful print via SVM classification. Both approaches aim to detect completion failure defects and substantial shape deviations.

The Spaghetti Detective [B30] is a commercial product which also uses a camera to monitor the print and claims to apply a deep learning algorithm for the detection of “spaghetti balls”, resulting from unsupported extrusion of material when the object comes off the printbed, due to insufficient adhesion.

Detection of defects and interruption of the print process only prevents failed prints, saving time and material. An attempt towards closed loop control with automatic correction was proposed for FDM [A22] and inkjet based [A57] processes. In both cases, laser profiling sensors were installed in the machine to measure the height profile of every layer, compare it to the model and potentially apply corrections in the next layer.

Laser scanners were also used for post-production verification of dimensional accuracy and influence of process parameters (infill rate, temperature) by Tootooni et al. [A85] and Khanzadeh et al. [A41]. The point cloud generated from a scan of the finished object is evaluated with different sophisticated machine learning approaches. The recorded data is compared with the original CAD model, considering the inherent deviations induced by the specific process parameters of each individual build.

Salary et al. describe an approach for optical in-situ monitoring of aerosol-jet printed conductive traces [A68, A69]. They mounted a CCD-camera coaxial with the spray nozzle for image acquirement and evaluated different Shape from Shading (SfS) approaches to reconstruct the 3D profile of the conductive track from 2D images. Successful application of SfS techniques requires a well controlled environment, where the illumination characteristics, surface reflectivity and camera direction are known. Reconstruction of the shape allows to estimate the resulting resistance based on the cross-sectional area of the wire. The work is currently limited to simple test patterns printed on a very smooth surface substrate, but could potentially be used with a fully additive process.

Chapter 3

Experimental Printing Platform

This chapter describes the physical manufacturing systems which were used as experimental printing platforms over the course of this thesis. As motivated in sec. 1.1, Fused Deposition Modelling (FDM) was chosen as base technology. To fulfill the scientific goals stated in the same section, the following additional hardware requirements are defined for the printing platform:

- Dispenser for conductive material to print wires
- Gripper to handle electronic components and potentially other additional hardware parts e.g. nuts or batteries
- Feeder or other storage apparatus to hold a stock of components for placing
- Vision system for precise alignment and positioning of components and documentation of the print-process
- Calibration system to assist precise calibration of all tools
- Controlling computer with extendable software (print server) to integrate control algorithms

A wide diversity of FDM 3D printers is commercially available on the market, ranging from cheap kits for self-assembly to professional industrial manufacturing systems. However, none of the available systems comes even close to meeting all of the requirements defined above. It became obvious very early in the process that the development of an experimental platform would take a substantial share of this work and in itself be an important aspect of the scientific contribution.

A 3D printer consists of several closely integrated hardware and software components. It is virtually impossible to consider only a single aspect separately. Up to a certain level of abstraction, hardware and software can be seen as two aspects of one physical machine. In the following sections, all relevant components of the printing platforms and the overall design concept are described in detail. This includes modifications of the firmware (section 3.2.1) and extensions of the print server (section 3.2.1), but not the development of a slicing software for tool path generation, which runs separated from the physical machine. The slicing software is detailed in chapter 4.

3.1 3D Printer Hardware

In the previous paragraph the functional goals of the demonstrator platform were defined. The diagram in fig. 3.1 shows a more detailed overview of the components required to achieve these goals.

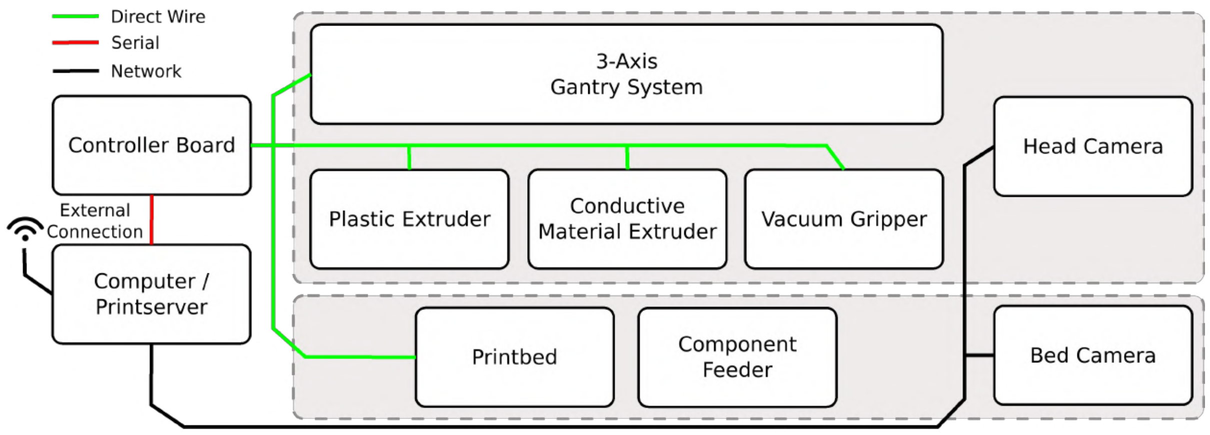

Figure 3.1 – Schematic of the main components required for the demonstrator printing platforms.

3.1.1 Demonstrator Platforms

Three different hardware platforms were used and iteratively developed to test and improve several aspects of the printing process. Two of the machines are equipped with a similar set of tools and are mostly controlled by the same software, the third was a Voxel8 printer, which was available as a commercial product (cf. 3.1.1).
All additional hardware components and modifications for the machines are collected and published as OpenSCAD files in a single repository: [B35].

Isel CNC Milling Machine

Figure 3.2 shows the first prototype, which is based on a retrofitted industrial Isel CNC milling machine. This hardware platform was chosen due to its large build volume of approximately $500 \times 500 \times 200\,\mathrm{mm}$ and its high robustness and mechanical precision, making it possible to rapidly test different tools and approaches regardless of their weight and size. This properties allowed to evaluate and qualify several cameras, vacuum systems, extruders, and component feeders without extensive optimization to fit them into a more integrated design.

The original controller board was replaced with a generic Arduino based controller board for 3D printers with integrated stepper motor drivers (cf. fig. 3.3, center). The original Isel stepper motor drivers were connected to a set of free extension pins to drive the heavy gantry system which requires significantly higher currents than a typical 3D printer (cf. fig. 3.3, left).
The machine provided only the pure 3D gantry-system. For usage as a 3D printer, basic additional hardware components had to be installed, mainly the printbed and plastic extruder. A glass plate laminated with heating foil was installed with three adjustable clamps as printbed (cf. fig. 3.2). Figure 3.3 (right) shows the extruder based on Gregs's Wade's design.

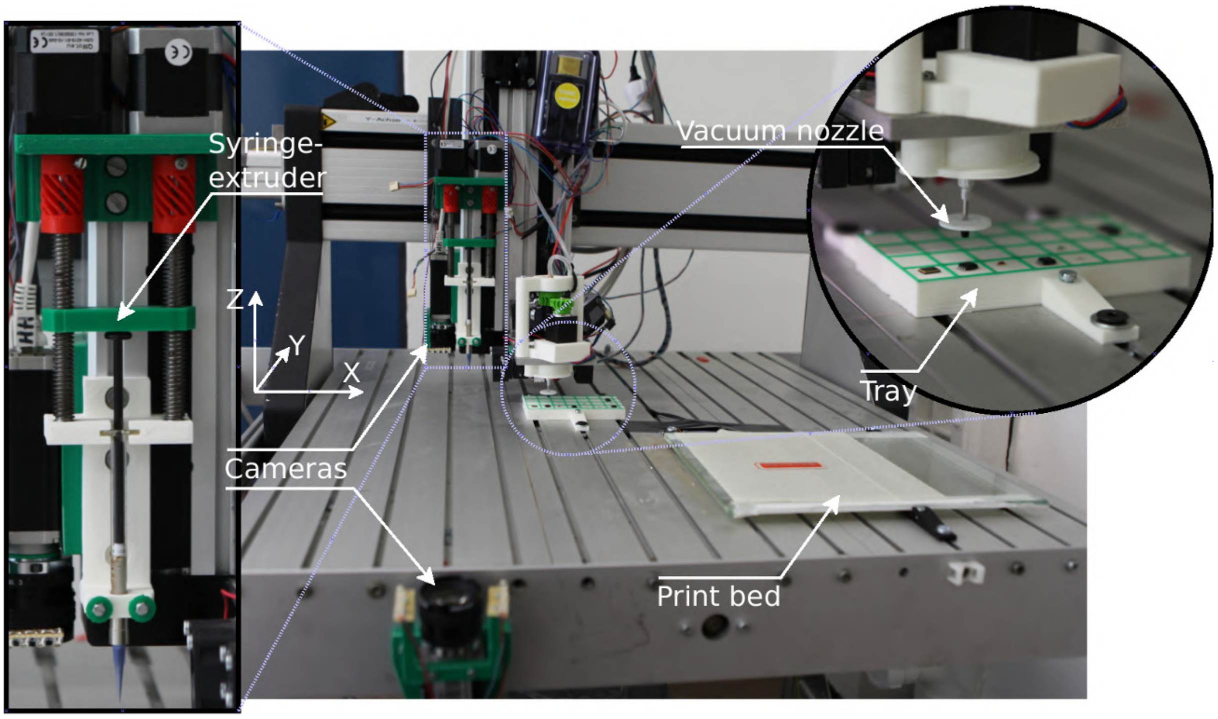

Figure 3.2 – First prototype of the demonstrator system, based on modified a CNC milling device. The large gantry system was chosen due to its size and robustness, making it easy to evaluate several iterations of different cameras, vacuum grippers and syringe extruders. The picture shows the final version of the first demonstrator, the testobject shown in fig. 7.2 was successfully printed with this configuration.

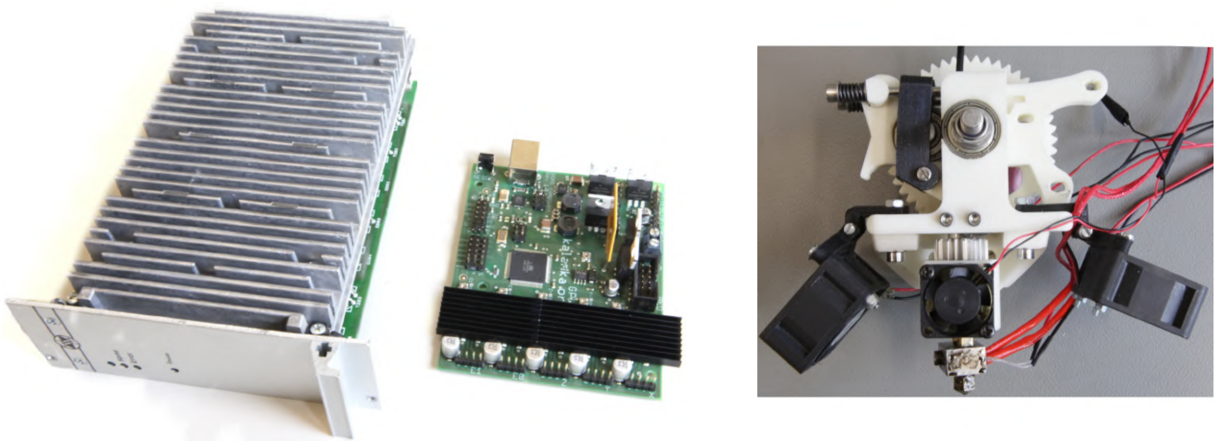

Figure 3.3 – **Left**: Original high-current stepper motor driver for a single motor. **Center**: Arduino based controller board running Repetier firmware. **Right**: Plastic extruder based on Greg's Wade's design.

This prototype was mainly used in 2014 and 2015 to evaluate several basic concepts and technologies. In particular, conductive materials and extruders were tested and developed as described in section 3.1.2, also a vacuum gripper was developed (cf. section 3.1.4).
With ongoing progress and an increasing level of integration, the disadvantages of a spindle driven gantry system, designed for high loads, became more prevalent. The most important are the following:

- Vibrations during movements, especially if all axes are moving simultaneously, caused significant shifts of SMD-components transported by the vacuum gripper, inducing frequent misplacing of the components.
- The conductive paste and some plastics require a controlled thermal environment for curing and to prevent warping, which is not available with this large and open system.
- The gantry system emits high frequency noise, requiring the operator to wear ear protection while working close to the machine.

To resolve these issues a second demonstrator platform was developed, which is portrayed in the following section.

Kühling & Kühling Industrial RepRap

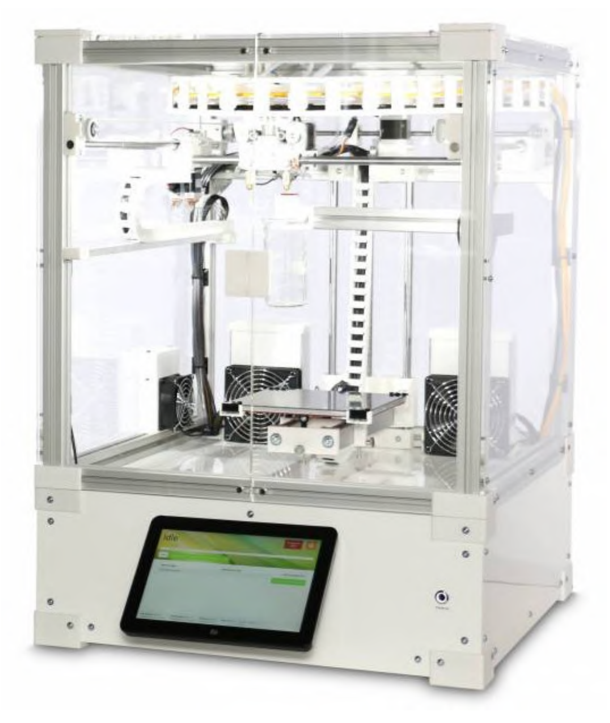
Figure 3.4 – Industrial RepRap printer used as base for the second demonstrator platform. Image by Kühling & Kühling GmbH, used with permission.

Based on the experience which was collected during the experiments with the first development prototype the second and primary demonstrator platform has been built. Figure 3.4 shows the original Kühling & Kühling Industrial RepRap printer as delivered by the manufacturer. Important criteria to select this machine were:

- The heated chamber allows to print ABS and PolyAmide (PA) based materials and to control the curing process for conductive inks.
- Large physical dimensions for additional hardware components within the heated chamber.
- Following the open source hardware principle [B21], the sources of all hardware and software components are publicly available under Creative Commons or GPL licenses. Furthermore, all plastic parts are designed to be printable on the machine itself. This makes it possible to easily modify the printer.

To fulfill the requirements sketched in fig. 3.1, the following individual modifications and extensions were applied to the Hardware:

Chamber The closed chamber is crucial to control the temperature when printing temperature-sensitive plastics and for thermal curing of the conductive ink. To gain space for the additional hardware, the height of the chamber was enlarged by 20 cm (cf. fig. 3.5, left).

X-Carriage The original carriage contained two direct-drive extruders, including stepper motors and planetary gears. Wiring and filament feeders are connected to the printer by a horizontally bending energy chain. The extruders were mounted at a fixed position and height. The entire carriage was replaced by a modified design which was printed on the machine itself. Figure 3.6 illustrates the individual components of the modified carriage. A single plastic extruder remains at its original position, but was replaced by a more reliable Bondtech BMG extruder with significantly lower slippage. The syringe extruder for conductive material and the vacuum gripper are both mounted on individual, servo-actuated micro-stages. Each tool can individually be lowered below the height of the primary (plastic) extruder to avoid collisions and mitigate oozing. A camera is mounted between the drive shafts, pointing downwards, illuminated by an LED-ring. All components are arranged in a way that each tool can cover the entire printbed.

Bed-Camera The bed camera is affixed to the frame, as close to the printbed as possible (cf. fig. 3.5, left). Vertical adjustment is not possible with this configuration. Mounting the camera at the printbed would allow vertical movements, but would have required significant modifications to the z-axis, which is currently prevented by a lack of sufficient space.

Component Tray The component tray is attached to the printbed, mounted with three adjustable screws for leveling (cf. fig. 3.14).

Controller / Network The printer's hardware is controlled by a RUMBA+ 1.4 control board which in turn is connected via serial over USB to a single-board computer, running the print server and user interface. The original BeagleBone Black was replaced by an ODROID-XU4 with more computing power. The machine has a dedicated internal Ethernet network for the cameras and a second external network for the web-based user interface.

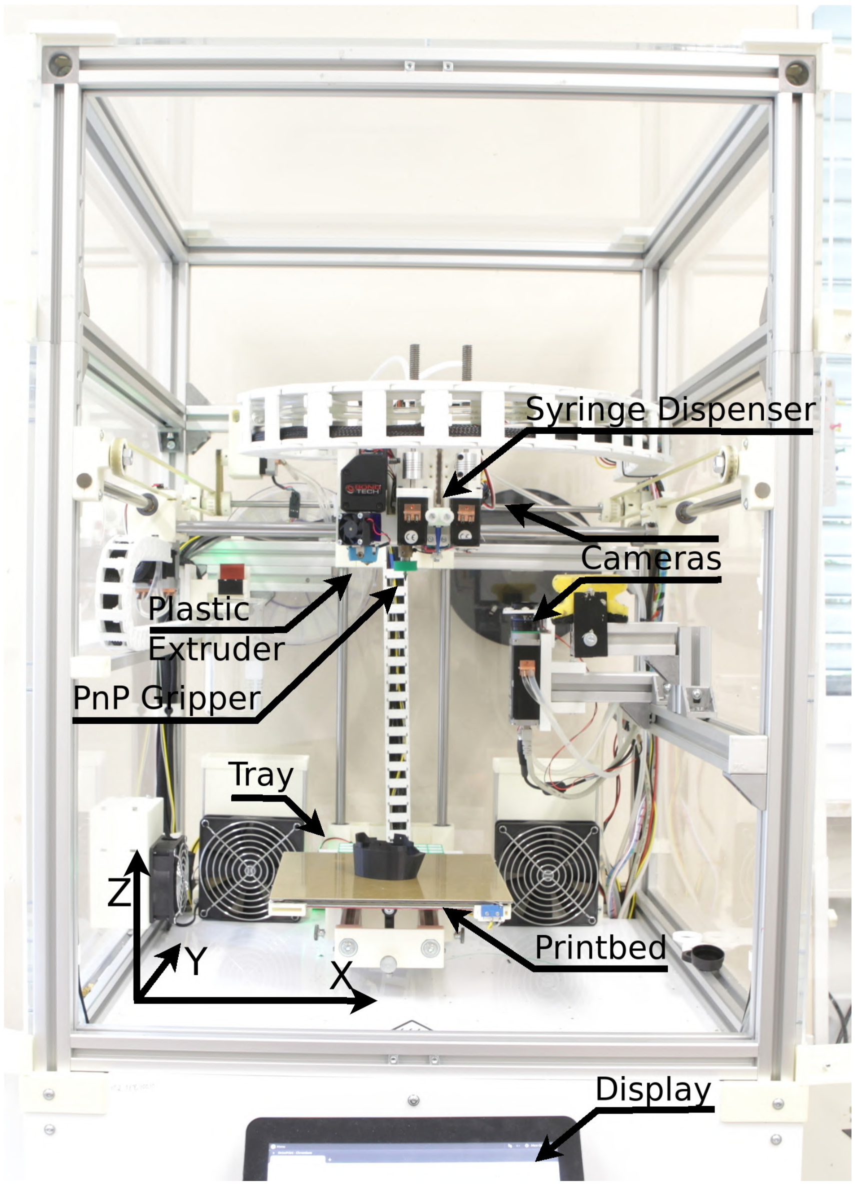

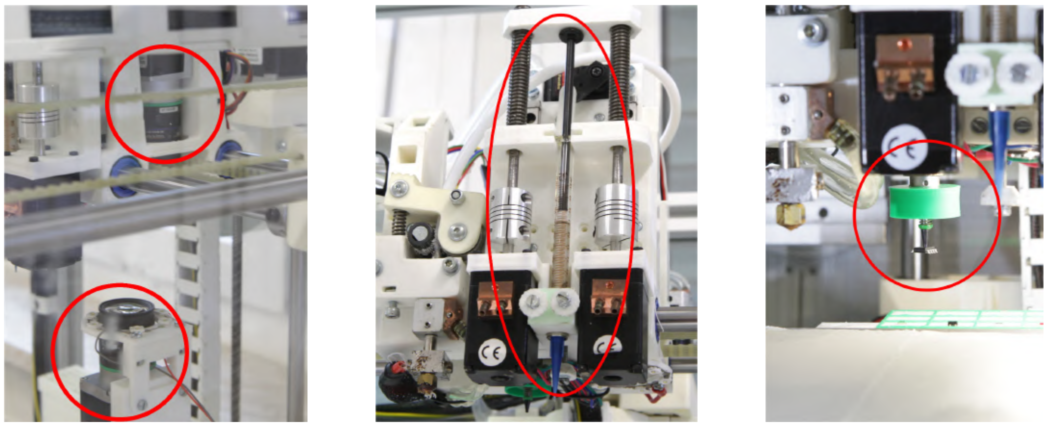

Figure 3.5 – Second prototype of the demonstrator system, based on a Kühling & Kühling Industrial RepRap printer. **Top**: modified machine, equipped with **left**: two cameras for component handling and process monitoring, one mounted at the printhead, one next to the printbed **center**: a screw-driven conductive paste extruder and **right**: a vacuum gripper for automatic component placement.

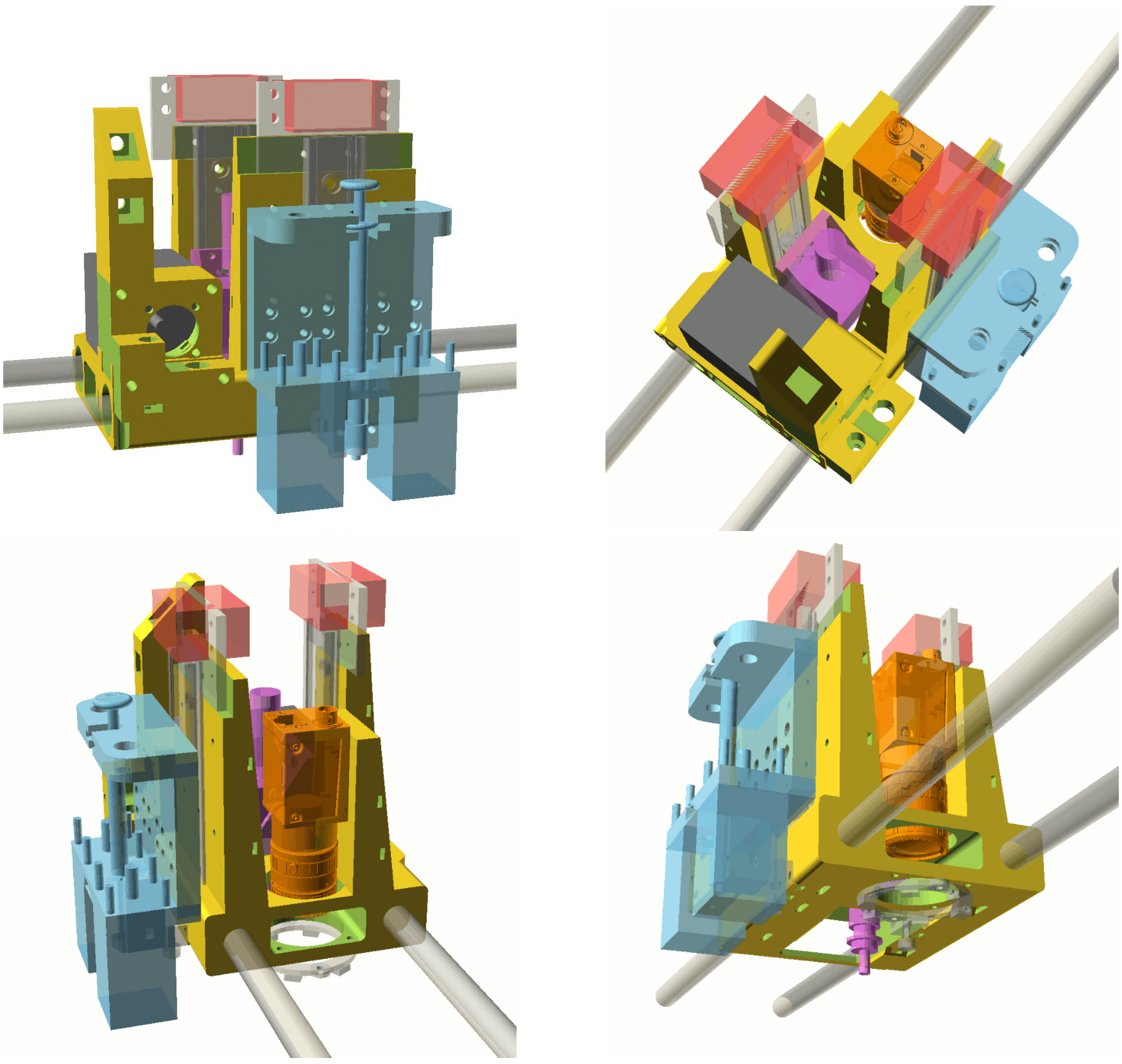
Figure 3.6 – CAD drawings of the modified X-axis. The syringe extruder (**blue**) and the vacuum gripper (**purple**) are mounted on individual linear bearings, their z-height is adjustable by servos (**red**). An industrial camera (**orange**) is mounted at the right side and illuminated by an LED-ring.

Voxel8

In addition to the demonstrator machines which were specifically built for the approaches and algorithms of this thesis, the modified version of Slic3r as described in chap. 4 and chap. 5 was tested with a standard Voxel8 printer, in cooperation with the Technical University of Darmstadt. The Voxel8 lacks any support for component handling, therefore only manual placing was possible. The printer otherwise mainly differs in the working principle of the conductive ink extruder. Voxel8 utilizes a pressure driven pneumatic dispenser with conductive ink similar to the material described in the next section 3.1.2.

Controlling the pneumatic extruder basically requires to set the pressure and actuate the valve before and after each line of extrusion which was achieved with minor modifications to the slicing software. Appropriate values for pressure and extrusion speed were obtained experimentally. As the volume of dispensed material can not be thoroughly predicted with this approach, only one single extrusion speed and diameter were available. Several simple test objects (wire through cube) were successfully printed. Further integration steps were ceased, when Voxel8 discontinued the support and stopped distribution of consumables shortly after the experiments.

3.1.2 Conductive Material Extrusion

In opposition to the plastic material for FDM processes, which allows for direct mechanical extrusion of an endless wire or filament, most suitable conductive materials show characteristics of a high viscosity fluid. For direct write applications the conductive material is usually processed by pneumatic or screw driven dispensers. For this work, only screw driven syringe extruders were used. Pneumatic dispensers require a dedicated controller and a mapping between nozzle diameter, writing speed and pressure to control the amount of dispensed material. For stepper motor actuated screw driven dispensers the amount of material is determined by the number of steps, the nozzle diameter, and inner syringe diameter, which directly corresponds to the parameters of a plastic filament extruder. Such a dispenser can be directly driven by an existing stepper motor driver on the printers controller board without firmware modifications. Furthermore, the material flow calculations in the slicing software can be directly applied if the syringe diameter is used as the filament diameter variable. The development of our dispensing system is depicted in fig. 3.7, the final version, mounted on an additional micro z-stage, is shown in fig. 3.5 (center) and fig. 3.6 (blue). All versions consist of a gas-tight glass syringe (Hamilton #1001, 1000 μl), one or two motors, ball bearings, a few screws and a number of printed parts. All components are comparably cheap and easy to obtain.

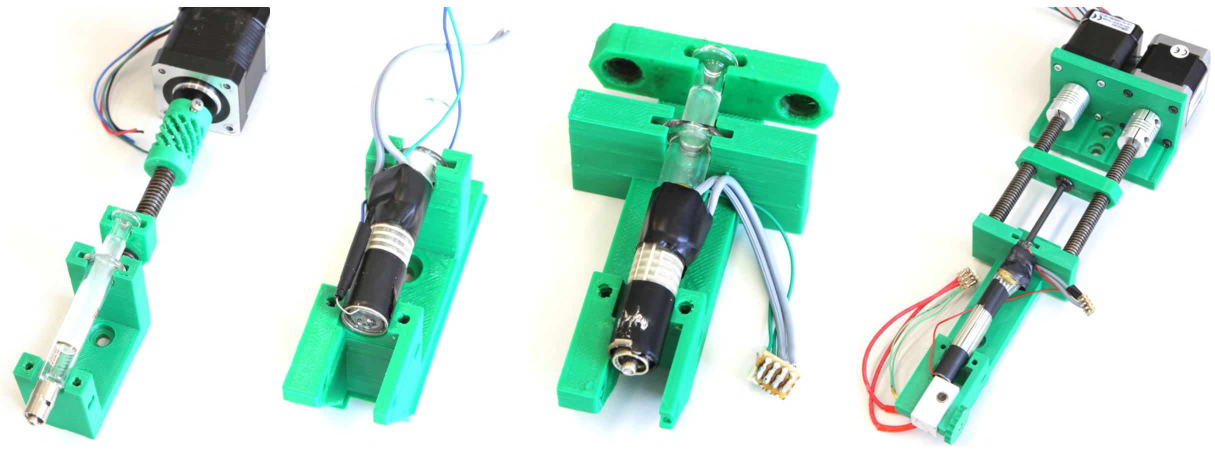

Figure 3.7 – Four evolutionary iterations of a screw driven syringe extruder. The design was adapted for different types of glass syringes, two screws for reduced backlash and a heating block to prevent solidification of molten alloys in the nozzle tip.

Field's metal		**#6130M, Methode Inc.**	
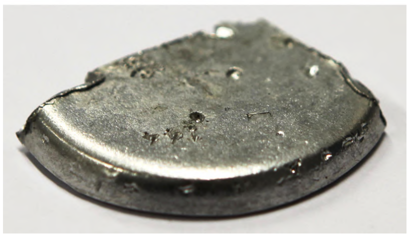			
Material:	In51Bi32Sn16	Material:	Silver filled polymer
Melting point:	$\sim$ 62° C	Curing:	$\sim$ 20 min. at 95° C
Cost:	$\sim$ 2500 € / kg	Cost:	$\sim$ 425 € / kg
Resistivity:	$5.2 \times 10^{-7}\,\Omega\,\mathrm{m}$	Sheet resistivity:	$40\,\mathrm{m}\Omega/\Box$ @ 1/2 mil print thickness

Table 3.1 – Properties of the conductive materials used in this work.

Two conductive materials have been successfully printed with the extruder: In51Bi32Sn16 (Field's metal) and silver filled polymer ink (#6130F and #6130M, Methode Electronics Inc.). Unless explicitly stated, #6130F conductive ink was used for all experiments described in this document. The reasons for this decision are explicated in the following.

Fields's metal is an eutectic alloy with a melting point of approximately $62\,°\mathrm{C}$. The syringes were wrapped in heating foil to liquefy the material for dispensing. The needle was additionally enclosed by a heating block to prevent cooling and clogging in the thin needle (see fig. 3.7, right). Both heaters were powered and controlled by a spare connector for additional FDM-nozzles and treated as an extruder temperature by the printer's firmware.
A series of simple specimen was fabricated to evaluate the material. Four straight lines were dispensed directly on top of a flat surface and into channels, both printed with Polylactic Acid (PLA). While In51Bi32Sn16 has a generally higher conductivity than conductive inks, a number of negative properties are prevailing. As stated in [A73], the surface tension of liquid metal is very high, resulting in bulky traces and preventing the nozzle to disconnect from the floating material without strong oozing effects (fig. 3.8, left). Besides, fig. 3.9 shows how bonding between the metal and the plastic object proved to be insufficient. In previous work, lead based alloy has been extruded on PCL plastic by [A44], but the bonding test was applied against a PCB surface only.

In contrast to Field's metal, the #6130F polymer ink shows excellent bonding and extrusion characteristics. The sheet resistance is $40\,\mathrm{m}\Omega/\Box$ when cured at a temperature of $95\,°\mathrm{C}$, as stated by the manufacturer. Curing at such a high temperature is not possible for PLA objects, since the glass transition temperature of PLA is approximately $60\,°\mathrm{C}$ and the objects would deform during the process. ABS or PA based materials can withstand this temperature, but the heating chamber of our printer is currently not able to maintain temperatures above $70\,°\mathrm{C}$.
In addition to the temperature related questions it was expected that the curing characteristics of ink completely enclosed in plastic might be insufficient for more sophisticated circuits. To evaluate this issue a number of test patterns was printed on both, an open surface and covered by

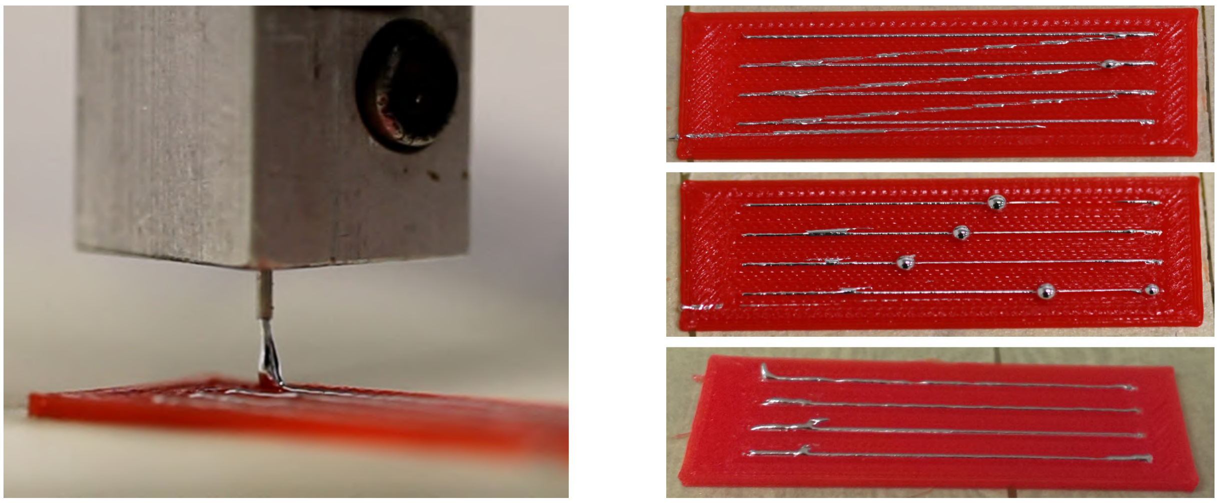

Figure 3.8 – Dispensing experiments with In51Bi32Sn16 (Field's metal). **Left:** high surface tensions prevents the extruder to disconnect from the alloy at the end of a printed line. **Right:** strong oozing effects (top) were countered by retraction which frequently causes suction of air and results in alloy drops (center). Successful print after precise calibration of the dispenser and with additional wiping movements (bottom).

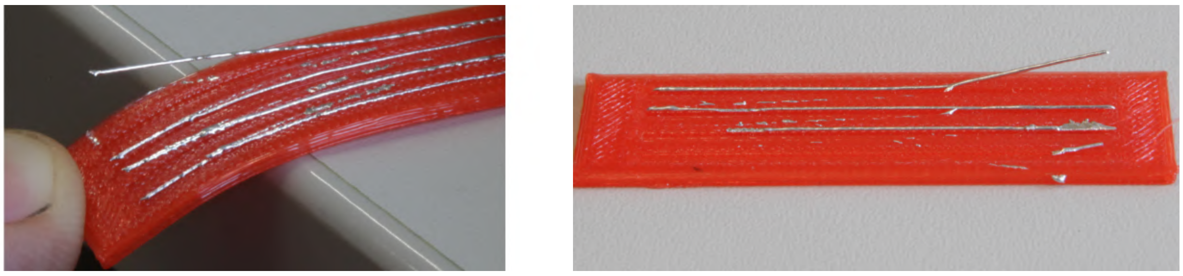

Figure 3.9 – Insufficient adhesion of metal alloy on plastic during bending (left) and after bending into the opposite direction (right).

plastic. The resistance of a $90\,\mathrm{mm} \times 0.5\,\mathrm{mm} \times 0.25\,\mathrm{mm}$ trace was measured over time at room temperature (20°C) and in a heated chamber (60 °C). The results are shown in fig. 3.10 and indicate that the curing is primarily determined by the temperature.

Depending on the nozzle diameter, a line width of $0.2\,\mathrm{mm} - 0.7\,\mathrm{mm}$ is achievable by the extruder on a smooth surface. A line width of $0.2\,\mathrm{mm} - 0.3\,\mathrm{mm}$ is desired for fine pitch package sizes (e.g. TSOP). Currently, a line width of $0.5\,\mathrm{mm}$ can be reliably achieved on a printed surface. Smaller traces are subject to disruptions, caused by bruises in the printed object. Besides, the line width is limited by a certain amount of ink required to ensure adhesion of the parts as described in section 3.1.3.

Refilling the syringe and replacing the nozzle tip requires some care. Gas inclusions have a significant effect on extrusion precision: they behave as a spring when fast retraction- and unretraction movements are executed, resulting in underextrusion at the start point and overextrusion or oozing at the end point of a line.

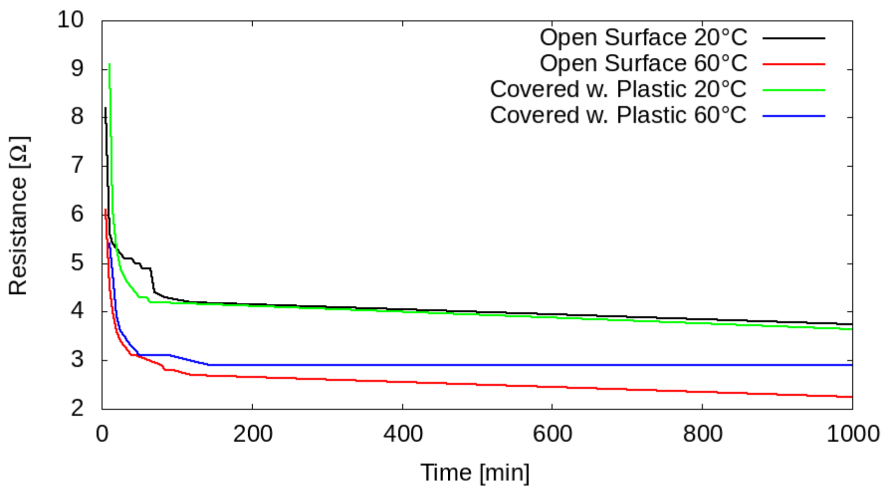

Figure 3.10 – Curing characteristics of #6130F polymer ink. The resistance of a $90\,\text{mm}\times0.5\,\text{mm}\times0.25\,\text{mm}$ trace printed on both the surface of an object and entirely enclosed in plastic is measured during the curing process at room temperature (20 °C) and in a heated chamber (60 °C).

Frequent reasons for gas bubbles in the syringe are:

Stirring Conductive polymer settles when stored for more than a few hours and must be stirred before usage. Mechanical stirring introduces air bubbles, which can be sucked into the syringe. We therefore use slow, magnetic stirring.

Outgassing Ink can be loaded by applying vacuum inside the syringe (drawing the plunger). This potentially causes outgassing at the surface.

Nozzle Tip Small air bubbles remain at the fringe of a the nozzle tip after replacing it.

To reliably remove all gas inclusions, the loaded syringe is centrifuged for approximately 300s at $225\,\text{rpm}$ after each refill. It is further important to apply only small amounts of retraction to the syringe extruder. If the amount of retraction is higher than the volume of the nozzle, air enters the syringe and accumulates at the top.

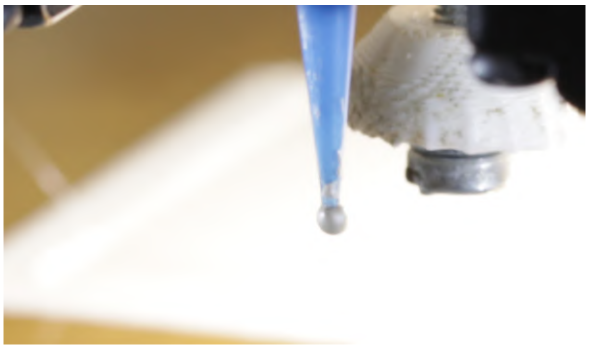

Figure 3.11 – Oozing at the syringe extruder due to thermal expansion.

Despite from gas inclusions, thermal expansions also has a notable effect when the syringe is correctly filled. Figure 3.11 was taken during a print, after the extruder was not used for a few layers. The heated printbed slowly warms up the syringe and forces the expanding material out of the tip. If both extruders are at the same height, as it was in early versions of the printers, the oozing ink gets smudged over the surfaces, potentially causing shorts. The micro-stage prevents this effect by lifting the extruder when it is unused, but priming and wiping is required after every toolchange to remove excess material.

3.1.3 Bonding Characteristics

Since the SMD components are affixed by placing them directly into uncured ink, the bonding characteristics are crucial to assess the electrical and mechanical quality of a manufactured object. Besides, this information is relevant for the design of tool path generators (slicing software).
As shown in fig. 3.12 (left), a series of specimen were produced on the printer, each containing several 1206 SMD-resistors, placed with increasing time delay on two $0.5\,\mathrm{mm}$ ink traces. In the image, the x-axes indicates the time between ink dispensing and component placing. After an additional curing period of one day, a shear force was applied to the parts by a calibrated flat spring until the part was released. The results are shown in fig. 3.12 (right).

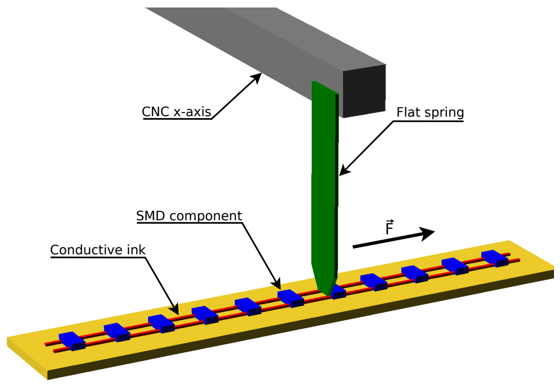

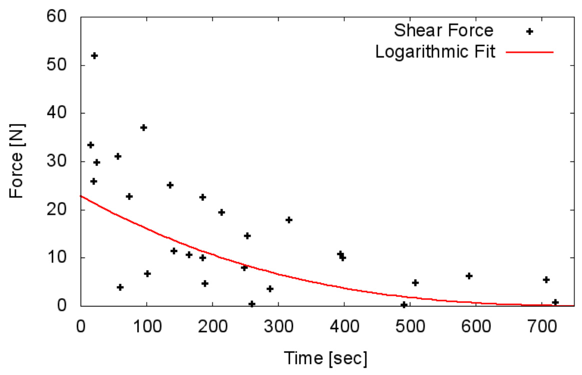

Figure 3.12 – Evaluation of the bonding quality between conductive ink and SMD components. **Left:** Experiment setup to measure shear forces required to release SMD components from cured ink traces on the surface of printed specimen. **Right:** Measured shear forces to release the components, the x-axis indicates the time between finishing the ink trace and placing a part onto this trace.

The data shows high variance but a trend is clearly visible. The bonding quality partly depends on the conductive line geometry which varied over time due to several recalibrations of the syringe extruder during the long experiment. The results indicate that a fast placing of parts after the fabrication of a conductive trace is important to achieve reliable connections. A period of up to 100 seconds for uncovered parts at the objects surface and 200-300 seconds for plastic covered parts is considered to be a reasonable value. This implies that it is not possible to create a trace, continue printing the object and place the part into a left open cavity for most objects, because printing several layers usually requires more than 3 minutes. Potential approaches to mitigate this problem are:

- Deposition of small ink droplets on the pin landing areas. This requires an appropriate needle and potentially causes collisions between the plastic extruder and the object since the landing layer is below the objects surface. The implementation of this approach is documented in sec. 4.5.2.
- Additional fixation of the component by glue droplet, potentially jetted against the underpart.
- Embedding the parts upside down and connecting the part by ending the conductive trace on the pad. This approach probably requires additional fixation as described above to avoid shifting when contacted by the extruder.
- Usage of conductive ink with slower curing characteristics. Depending on the material properties, this probably has a negative effect on the overall curing of traces enclosed by plastic.

3.1.4 Component Handling

This section describes the hardware specifically deployed for precise placing of small components. The software aspect, including image processing is covered in the next section 3.2.

Vacuum Gripper

The second demonstrator platform is equipped with a pivot-mounted vacuum nozzle to grip, rotate and place SMD-components as illustrated in fig. 3.6 (purple) and fig. 3.5 (right). A standard industrial pick and place nozzle (Juki 503) is directly mounted to a NEMA11 Hollow Shaft Stepper Motor. The motor is connected as an additional extruder, the G-code `E<value>`-parameter causes a nozzle rotation of `<value>` degree instead of filament extrusion. Vacuum is generated by a small 24 V vacuum pump. The nozzle can be controlled via a solenoid by G-code commands. The gripper is mounted on a micro z-stage which is actuated by a servo so it can be lifted during normal print moves to avoid collisions and lowered below the plastic extruder to press components against the surface. The contact pressure is mechanically regulated by the integrated spring.

```
1   M340 P1 S1000 ; Lift vacuum nozzle
2   M340 P1 S1800 ; Lower vacuum nozzle
3   M42 P33 S255  ; Activate vacuum pump
4   M42 P33 S0    ; Deactivate vacuum pump
5   M42 P08 S255  ; Open valve
6   M42 P08 S0    ; Close valve
7
8   G1 E90        ; Rotate nozzle 90°
```

Figure 3.13 – G-code commands used to control the vacuum gripper. Lines **1-2:** PWM defined positions of the servo connected to pin 1. Lines **3-6:** Enable / disable pin 33 / 8 to power the pump via a MOSFET or actuate the solenoid respectively. Line **8:** Coordinated Cartesian movement with the extruder-axis as only argument, causing a nozzle rotation of 90°. All commands are standard G-codes, available in most 3D printer firmwares.

Component Tray

Commercial pick and place machines are supplied with components by reel feeding systems to facilitate high throughput. While this is reasonable for an industrial process where the same object is assembled many times in a row, it is not very suitable for the additive manufacturing of prototypes, where each object potentially requires a different set of external components with different shapes and dimensions.

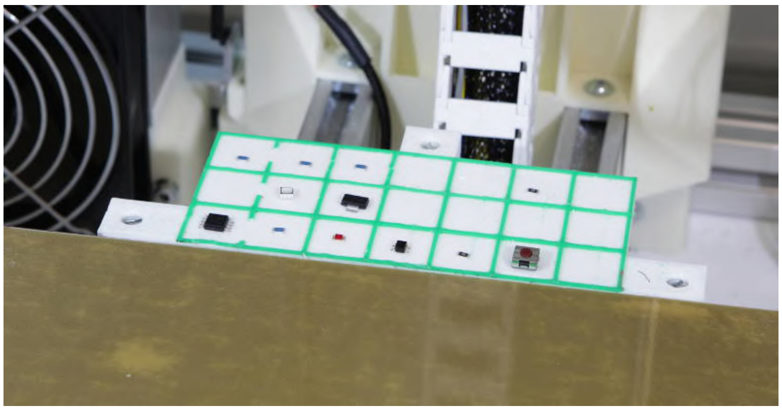

Figure 3.14 – Component tray attached to the printbed. Each box is supposed to hold a single SMD-component, roughly orientated. The boxes are separated by a raised, colored rim to prevent shifting of the components and provide a defined optical boundary for the vision algorithm.

Figure 3.14 shows the 3D printed component tray mounted next to the printbed of both demonstrator machines. The tray's surface is divided into boxes by a raised, colored rim. Each component is placed in a single box. As described in section 3.2.2, the known box dimension and rim color is used by the vision system as a reference frame for self calibration. Prior to each print job, the required components are placed manually on this tray by a human operator, according to the instructions from the print server as described in section 3.2.1.

Camera System

Both demonstrator platforms are equipped with two camera systems. The cameras were initially intended to guide the pick and place operations for SMD components, but additionally proved to be very useful for calibration (sec. 3.3) and general process documentation and verification purposes (chap. 6). The positions of the cameras are highlighted in fig. 3.2 and fig. 3.5 respectively. All cameras are illuminated by LED rings.

The bed camera is mounted at a fixed position, relative to the frame and facing upwards. The focus is adjusted to the tip of the vacuum nozzle to provide high resolution images for component alignment.

The head camera is mounted at the x-axis, facing downwards, and can be freely positioned in all three dimensions over the printbed.

We use industrial Basler Pilot (piA2400-17gc) and smaller Ace (acA2500-14gc) cameras with a similar resolution of approximately 2500×2000 pixels and C125-0818-5M lenses with a

Figure 3.15 – **Left:** Ace (acA2500-14gc) camera, **center:** Pilot (piA2400-17gc) camera, **right:** C125-0818-5M lens. Images ©: Basler AG.

focal length of $8.0\,\mathrm{mm}$. The cameras are connected via IEEE 802.3 Ethernet to the on-board computer running the print server. To achieve higher compatibility and modularity our print server extension OctoPNP [B33] (section 3.2.1) does not access the cameras directly. Every time an image is required OctoPNP executes a user defined script which must be adapted for every installation according to the deployed camera setup. OctoPNP expects a set of correctly cropped and rotated images after executing the script. It is therefore very easy to work with different types of cameras.

3.2 Control Software

A FDM 3D printer generally consists of a gantry system, actuated by stepper motors, and a number of heating elements for extruders, printbed and chamber. Except from endstops, the gantry system is fundamentally controlled in an open loop. The position of each axis is solely determined by the history of steps executed by this axis. Whereas the thermal subsystems are closed loop controlled by Proportional Integral Derivative (PID) controllers.

All hardware components are controlled by a microcontroller on the controller board, which runs the low level real time Firmware introduced in section 3.2.1. The firmware accepts and executes ASCII encoded G-code commands over a serial connection. Section 3.2.1 also describes the print server, which provides a user interface and transmits longer G-code files line by line as they are executed by the printer, to perform a full printjob.

3.2.1 Firmware & Print Server

The Industrial RepRap printer originally runs Repetier Firmware [B11] on the controller board and a self-developed print server for the user interface. The firmware was updated with a modified version [B32] configured for the new dimensions of x- and y-axis, additional extruders, servos and the vacuum solenoid. The print server was entirely replaced with OctoPrint [B10]. OctoPrint is well supported, widely used and provides an extensive plug-in mechanism, making it possible to control almost every aspect of the printer communication, which is crucial to implement interactive pick and place control.

3.2.2 Pick and Place

To execute component placement operations and integrate the cameras, OctoPNP [B33] was developed as an OctoPrint plug-in. The cameras are connected to the print server via network as explicated above, but encapsulated by an additional layer of abstraction to simplify the usage of different camera types. OctoPNP executes a script to trigger the camera and expects a correctly rotated and cropped image on a predefined path as result. The script must be provided as a wrapper for each individual type of camera.

Upon opening a G-code file in OctoPrint, OctoPNP searches for embedded information about electronic components. The shape of each component and its destination position are encoded in a custom XML-based G-code extension as illustrated in fig. 3.16. The plug-in renders a visual representation of the feeder tray containing all required SMD-components to indicate their expected position for the operator to prepare the printjob (fig. 3.17).

```
G28                         // Home alle axis
G1 X10 Y35 Z14 F3000        // Move toolhead to position
M361 P4                     // Place component 4

;<part id="1" name="LED_1206">
;   <position box="4"/>
;   <size height="1.05"/>
;   <shape>
;     <point x="-1.6" y="-0.8"/>
;     <point x="-1.6" y="0.8"/>
;     <point x="1.6" y="0.8"/>
;     <point x="1.6" y="-0.8"/>
;   </shape>
;   <pads>
;     <pad x1="-1.5" y1="0.75" x2="-1.1" y2="-0.75"/>
;     <pad x1="1.5" y1="0.75" x2="1.1" y2="-0.75"/>
;   </pads>
;   <destination x="104.93" y="27.98" z="8" orientation="90"/>
;</part>
```

Figure 3.16 – XML G-code extension for in-line description of SMD components in a common G-code file.The M361 command actually executes the placing operation for a certain object during the printing process. XML-lines start with a ";", marking them as comments in normal G-code syntax to avoid interference with the printing process. The `<shape>` and `<pads>` information is currently used by the host software to visualize the position of the components on the tray.

Placing a particular component is triggered by a `M361 P<part_id>` command in the G-code. OctoPNP detects this command as it is processed by OctoPrint, interrupts the printjob before it is transmitted to the printer's command queue and executes the following hard-coded steps:

Pick Take a picture of the respective tray box with the head camera to locate the exact position of the component in this box. Pick the component at its center of mass.

Align Move the vacuum gripper to the bed camera, take a picture, rotate the component into its target orientation and correct translation offsets by again finding the center of mass.

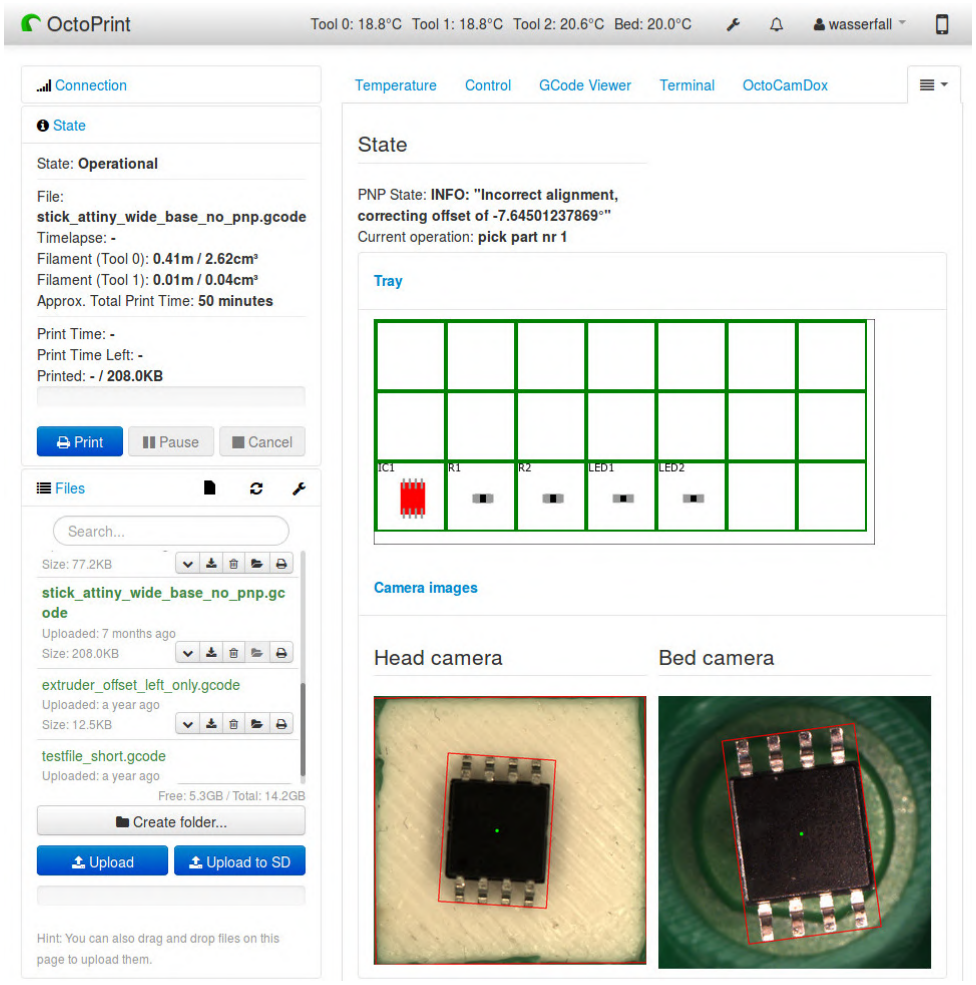

Tool 0: 18.8°C Tool 1: 18.8°C Tool 2: 20.6°C Bed: 20.0°C wasserfall

State: **Operational**

File: **stick_attiny_wide_base_no_pnp.gcode**
Timelapse: **-**
Filament (Tool 0): **0.41m / 2.62cm³**
Filament (Tool 1): **0.01m / 0.04cm³**
Approx. Total Print Time: **50 minutes**

Print Time: **-**
Print Time Left: **-**
Printed: **- / 208.0KB**

Size: 77.2KB

stick_attiny_wide_base_no_pnp.gcode
Uploaded: 7 months ago
Size: 208.0KB

extruder_offset_left_only.gcode
Uploaded: a year ago
Size: 12.5KB

testfile_short.gcode
Uploaded: a year ago

Free: 5.3GB / Total: 14.2GB

Hint: You can also drag and drop files on this page to upload them.

State

PNP State: **INFO: "Incorrect alignment, correcting offset of -7.64501237869°"**
Current operation: **pick part nr 1**

Figure 3.17 – Screenshot of the OctoPNP plug-in during a placing operation. The position of all required components is indicated as tray preview. The currently grasped component is highlighted in red. The head camera shows the position detection in the physical box, the bed camera measures the deviation of position and rotation after grasping the component.

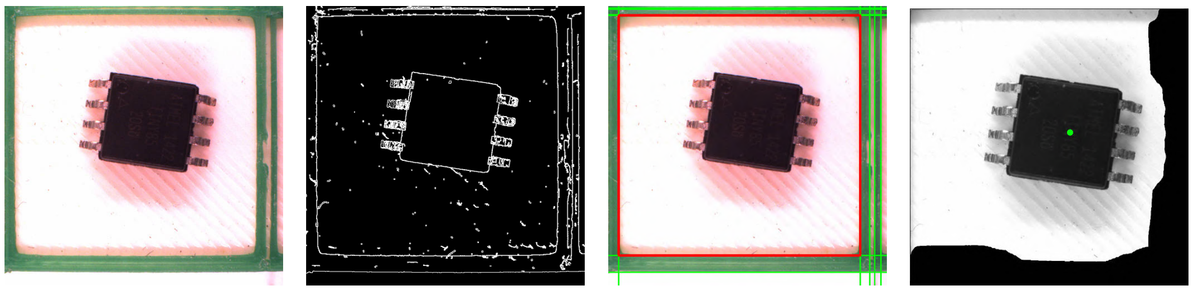

Figure 3.18 – Image processing steps to locate a single SMD-object in a given tray box. From left to right: raw image provided by the top camera, edges extracted by Canny detector, relevant lines filtered by Hough transform (green) and minimal bounding box (red), objects center of mass from histogram.

Place Move the vacuum gripper to the component destination at the part and place it into the conductive ink.

To execute those steps a vision system is required which can identify the tray boxes and find the position and rotation of a component. It was expected that image processing for pick and place applications be a well understood and solved problem. However, no suitable solution was found for integration into an open source project. OpenPnP [B20] provides some software for low-budget pick and place installations, but is mainly written in Java and is generally not well suited for the integration with our software ecosystem.

The image processing steps implemented in OctoPNP are based on the OpenCV framework which provides a Python interface, making the integration into the Python-based plug-in very simple. SMD-parts must be placed on the tray by a human operator prior to a printjob. The rotation must be within a range of ± 45° since the vision system is not aware of the objects absolute rotation, e.g. the polarity of a diode. The tray boxes can be used as a reference frame to locate the objects, requiring only a rough calibration of the top camera.

Three slightly different approaches for image processing were implemented. The first iteration is described in [A90]. Figure 3.18 illustrates how it utilizes a Canny edge detector and Hough transforms to identify relevant features in the image. The orientation is found by computing the average direction of filtered edges in the image relative to the closest 90°axis.

To improve reliability and accuracy, the initial vision pipeline was revised into a more modular approach, consisting of three basic steps:

- remove the background
- find the bounding box of the masked object
- compute orientation or center of mass from the bounding box

The underlying assumption for the usage of both edge- and bounding box-detector to measure the rotation is, that components are mostly rectangular or have at least straight features.

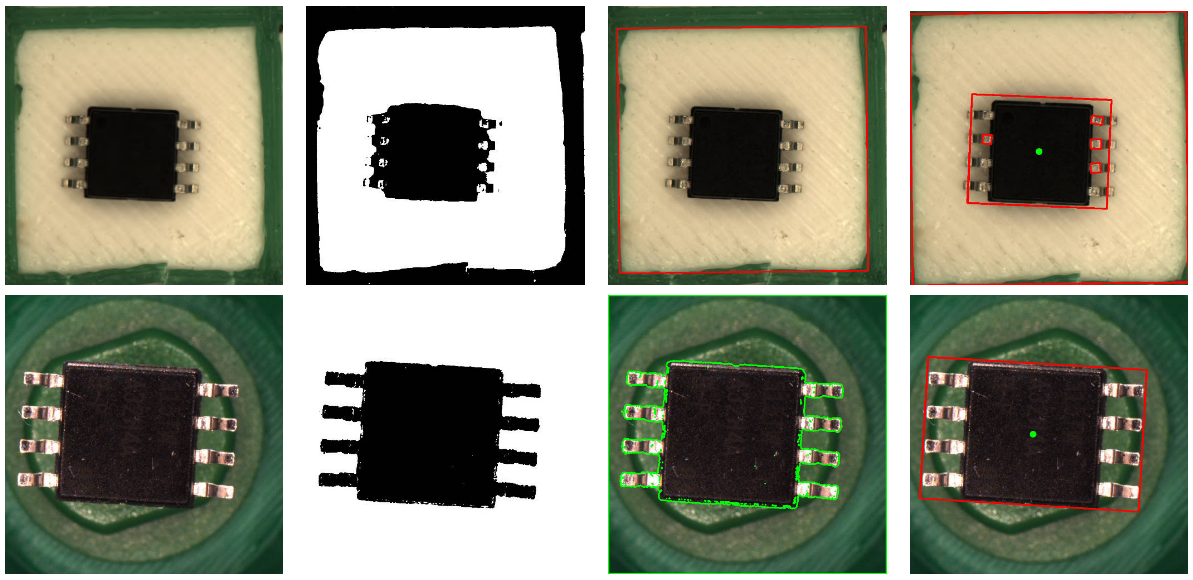
Figure 3.19 – Image processing steps to locate a component based on contours. From left to right: **Top**: raw image, binarized image to remove white background, large contour to find box, small contours to locate component. **Bottom**: raw image from the bottom camera, background removed by color filter, contour finding, bounding box to measure rotation and position.

As visible in fig. 3.19, bottom left, all parts of the vacuum nozzle are green to facilitate background masking. To remove all green background pixels from the image, it is first converted into HSV (Hue, Saturation, Value) color space and then range filtered to select all pixels in the green region of the value space. The resulting bitmap (fig. 3.19, bottom) can directly be used as binarized image for further processing steps. The white background inside of the tray boxes is masked by applying a simple binary threshold.

On the binary image, a contour finding algorithm is applied (green outline in fig. 3.19, bottom). The minimum area rectangle enclosing all contour points is computed in the subsequent step. If multiple contours were found, the minimum area rectangle computation is recursively applied to find the bounding box which encloses all contour rectangles. The resulting bounding box inherently has a rotation and a center point (fig. 3.19, right) which are directly used to determine the rotation and displacement of the component.

A third approach, based on template matching and Hough transformations, was implemented as a bachelor thesis [A45] and is currently under integration into the main version.

Incorporating vision feedback changes the printer control paradigm from open- to closed-loop. This raises synchronization problems since neither firmware nor print server are designed for this application. Taking an image at a specific position inside the printer requires the prinhead to move to this position (or the object attached to the printhead to the camera, which is a technically equivalent problem). The plug-in could simply inject some lines of G-Code to move to the target position, but unfortunately it is not clear at which point of time the printhead will arrive and stand still to take a picture. The reason for this problem is illustrated in fig. 3.20. The controller board buffers a number of commands (typically 16) in a move cache, to ensure a smooth

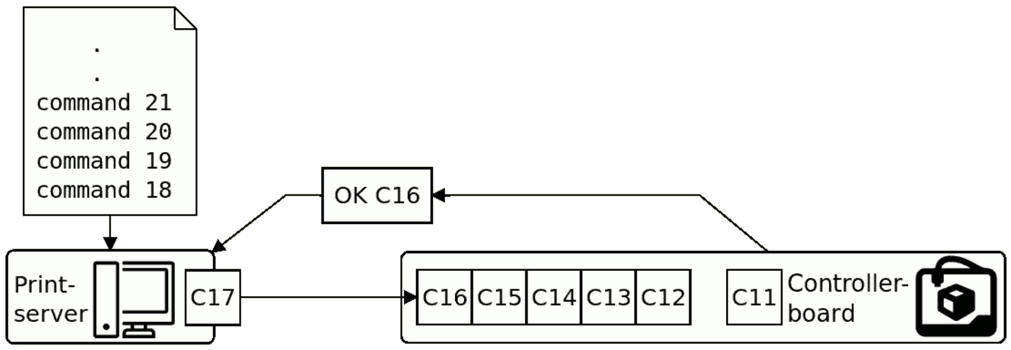

Figure 3.20 – Illustration of the command buffer within the printers controller board. The queue size in this example is 6. The print server sends a single command and waits for an acknowledging `OK`. The controller acknowledges commands immediately until the buffer is full. In this example, the print server waits for the permission to send `C17`. `C11` is currently executed, so the controller sends the pending acknowledgement for `C16`, allowing the print server to transmit `C17`.

trajectory execution in situations with multiple short travel distances, where the transmission of a G-Code line from the print server to the controller board takes longer than its execution. It is possible to flush the move cache by sending a `M400` command, which is only acknowledged when it gets consumed.

The plug-in mechanism in OctoPrint provides callbacks, implementing a hook-scheme to interact with the G-Code stream during execution. Right before a particular line of G-Code is sent to the printer, a plug-in subscribed to this hook, has the option to read the line, suppress it, or replace it by one or multiple different commands. OctoPrint maintains a second queue of outgoing commands to support injection of additional lines. OctoPNP could replace a `M361` command (which triggers the placing of one component) with a series of commands to move the camera to the corresponding tray position, terminated by a `M400` to flush the move cache. However, the plug-in still needs to be notified before the next regular line of G-Code is sent to the printer, as this is the moment where the image must be taken. To achieve this, we inject an additional `M362` as a marker after the `M400` command. Once the hook is invoked again for the marker command, the plug-in exactly knows where the printhead is at this point of time an can take a picture.

A modified firmware with support for coupled communication was considered as a simpler solution for the double queue synchronization problem, but was eventually not used to preserve compatibility with other printers and software systems.

3.3 Calibration

Precise calibration of all components in the manufacturing machine is absolutely crucial for the successful fabrication of 3D printed electronics. Particularly for comparably cheap, belt driven 3D printing systems, calibration is required at frequent intervals, as the hardware suffers from backlashes and inaccuracies.

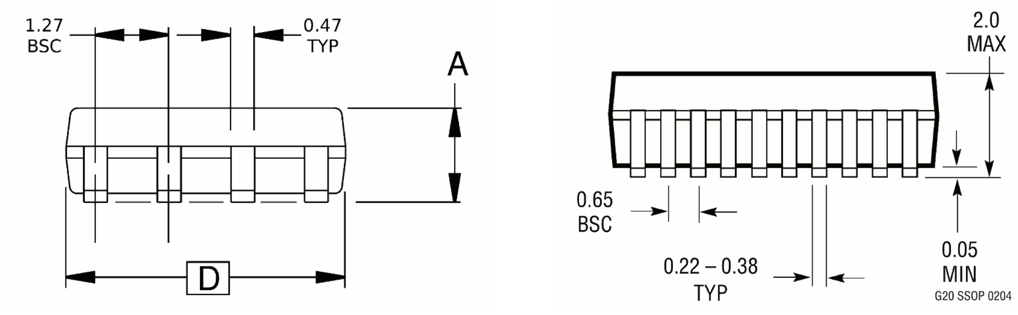

Figure 3.21 – Typical pin and pitch dimensions for large SMD packages SOIC (left) and SSOP (right).

Currently, realistic extrusion widths are $0.3\,\mathrm{mm} - 0.5\,\mathrm{mm}$ for plastic and $0.4\,\mathrm{mm} - 0.6\,\mathrm{mm}$ for conductive ink (cf. sec. 3.1.2). Figure 3.21 shows pin dimensions for common package types. Applied to the SSOP package with a pitch of $0.65\,\mathrm{mm}$, this leaves a space of approximately $0.15\,\mathrm{mm}$ between two wires for an average $0.5\,\mathrm{mm}$ conductive ink extrusion. Both plastic and ink dispensing and component placement are operating at the printers technical resolution limit.
For the purpose of this work, we therefore require the absolute deviation of each two components in the printer (e.g. "plastic extruder $\leftrightarrow$ vacuum nozzle" or "head camera $\leftrightarrow$ feeder tray") to be lower than $0.1\,\mathrm{mm}$.
For the first iterations of hardware development, this was achieved by printing calibration specimen with two materials and placed electronic components. The specimen where manually evaluated under a microscope and the deviation was corrected in the printer firmware. This proved to be very laborious and it is not possible to calibrate over multiple links. For example, it is not possible to find the exact position of the bed camera and vacuum nozzle by measuring the deviation of a placed component since both errors accumulate in this case. Most offsets can generally be corrected either by the slicing tool by adapting the g-code coordinates, or by the firmware. As far as possible, all corrections are done in the firmware, since otherwise the slicing step would have to be re-executed after each calibration and the offsets, measured in the machine, would have to be transferred to the slicing tool. A set of tools was developed and integrated into OctoPrint plug-ins to aid and automate most of the calibration tasks.

Calibration of the entire machine is composed of four aspects which require different methods, described in the following.

Backlash

The belt driven gantry system of the second demonstrator platform suffers from significant backlash effects due to limited belt tension and multiply geared transmission in the y-axis. A small OctoPrint plug-in *OctoPrint-Autocalibration* [B34] was written to automatically calibrate the backlash compensation values for the x-, y- and z-axis. The compensation is applied by the Repetier firmware running on the printers controller board. To determine the correct amount of backlash, the plug-in exploits the Hall-effect endstops by moving each axis into the endstop, and iteratively back to the opposite direction in $0.01\,\mathrm{mm}$ steps until the endstop state changes again. This indicates a physical movement of the axis. The process is repeated three times for an averaged result.

Backlash compensation significantly improves the accuracy. However, the backlash is not evenly distributed along the axes due to varying friction and is also influenced by temperature. Optical verification with the head camera reveals a remaining worst case backlash up to $0.1\,\mathrm{mm}$.

Planar Offsets
Planar offsets occur between all tool tips and cameras and can be divided into two cases: physically fixed links at the x-carriage and links between x-carriage and components mounted to the printers frame, including the printbed and component tray. With the two camera systems, it is possible to optically measure most of the links as described in detail below. The bed camera covers links within the x-carriage while the head camera can be used to find the positions of tools mounted to the frame.
We define the plastic extruder `T0` to be the primary tool and reference link. The positions of all other components in the printer are defined in relation to `T0`. The offsets between plastic extruder and other tool tips are calibrated as following:

Head Camera It is not possible to directly measure the position of the head camera. However, the offset is found with a simple intermediate step by printing a rectangular structure (cross), moving the camera to the arms for each axis respectively, correcting the position until cross and camera center are congruent.

Conductive Ink Extruder The conductive ink extruder `T1` offset can be found with two methods: by printing a cross as described above for the head camera, but correcting the extruder offset instead of the camera offset, or by moving `T1` directly over the bed camera. Both methods are indirect and require either a calibrated head or bed camera.

Vacuum Nozzle The vacuum nozzle position is determined by moving the nozzle over the bed camera and directly measuring the offset.

Bed Camera The position of the bed camera (and part tray) is not an actual offset, but the position of the optical axis with respect to the primary extruder `T0` which is only relevant within OctoPNP and not modeled in the firmware. It can be easily obtained by moving `T0` over the camera, manually aligning the optical center with the nozzle tip and storing the current extruder position as camera position.

Part Tray The part tray position is found by aligning the head camera with the front left corner of the tray (box position $[0, 0]$).

The adjustable Z-position of the conductive ink extruder and the vacuum nozzle pose additional difficulties for a direct camera based calibration. The measurement has to be done in the lower position to be precise, but this position is below the plastic extruder tip to avoid collisions. Due to the very narrow range of focus, the calibration of at least one tool tip suffers from image blur.

Offset calibration must be conducted after each filament change and syringe refill. Particularly the long syringe dispense tips are slightly bent. Figure 3.22 shows a screenshot of OctoPNP's calibration tool, which was added to facilitate the recurrent task of offset calibration. The current extruder offsets are read from the printer firmware, camera and tray positions are only

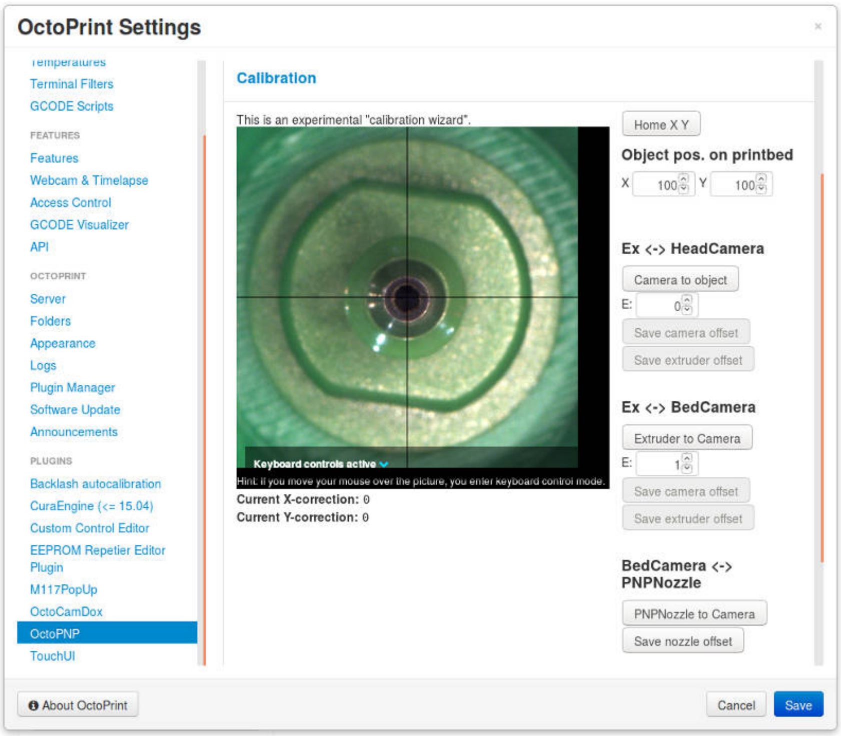

This is an experimental "calibration wizard".

Hint: If you move your mouse over the picture, you enter keyboard control mode.

Current X-correction: 0
Current Y-correction: 0

Figure 3.22 – Calibration tool, integrated into the OctoPNP plug-in. The screenshot shows calibration of the vacuum nozzle by manually adjusting the position in relation to the bed camera.

modeled in OctoPNP itself. The wizard supports calibration of the head camera against any object on the printbed or tray position, and extruders and vacuum gripper against the bed camera. Crosshairs allow alignment of the subject with the live camera image. The corrected offset is either stored in the OctoPNP configuration or propagated to the printer's firmware.

Thermal Deformation

Even with the accurate determination described above, offsets where still observed to be incorrect, the effect is particularly visible when conductive ink is not deposited at the center of a plastic channel. Calibrating the offset between T0 (plastic) and T1 (conductive ink) in cold state with the camera based calibration tool results in an observed x-offset of $0.4\,\mathrm{mm} - 0.6\,\mathrm{mm}$. The reason is assumed to be thermal deformation of the carriage, holding both extruders. The carriage consists of printed ABS. ABS has a linear thermal expansion coefficient of $\sim 0.1\,\mathrm{mm}\,\mathrm{K}^{-1}$. With an x-offset of $\sim 65\,\mathrm{mm}$ this would require a temperature difference of $60\,\mathrm{K} - 100\,\mathrm{K}$ to explain the effect. The carriage is mainly heated by the printbed which typically operates at $100\,°\mathrm{C}$. If the carriage is warmer at the lower side, bending could increase the effect.

The assumed explanation was not yet thoroughly verified. Obviously, all components must be heated to operational temperature prior to the calibration step. Doing so yields better ($\sim 0.2\,\mathrm{mm}$ offset), but still not perfect results. The temperature also varies during a printjob due to increasing distance to the printbed, heat from the stepper motors or open doors when components are placed manually.

Z Offsets

The last aspect which requires calibration is the relative height of the three tools. Due to their adjustable position, fortunately this can be done in software by applying different offsets to the printbed position. Figure 3.23 shows how the calibration itself is done by repeatedly moving the tool tips into a switch, mounted at the printbed and averaging the measured offset. The vacuum gripper nozzle requires less precision in z-direction as it is decoupled by a spring-pivoted bearing, to apply a certain pressure when placing a component into the ink.

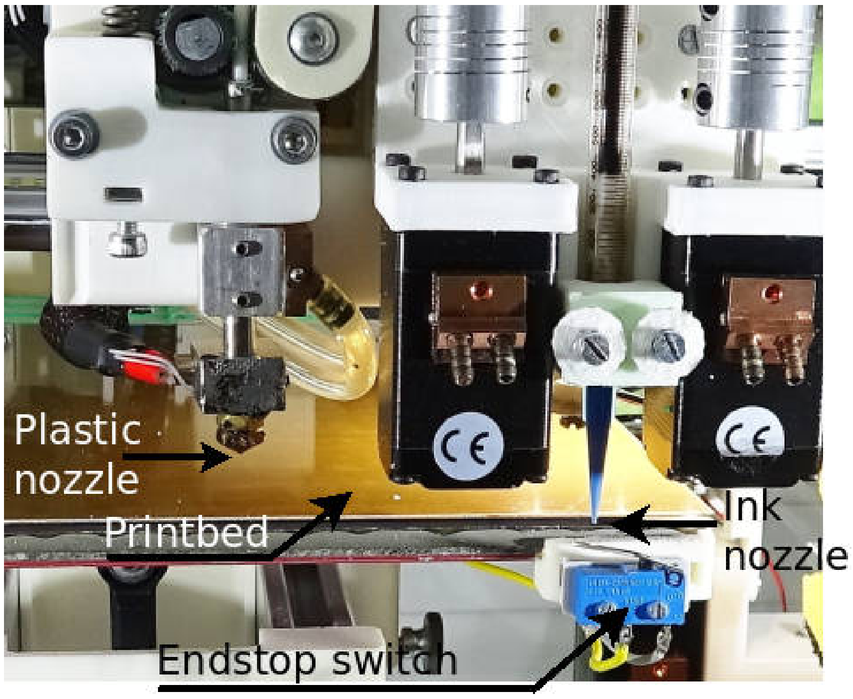

Figure 3.23 – Calibration of tool z-offsets via contact sensor. The blue switch is directly mounted to the printbed. Each nozzle is repeatedly driven into the sensor to measure an averaged distance which is then applied to the printbed when the respective tool is active.

Chapter 4

Integration of Electronics and Mechanical Objects

With a hardware platform available which is capable to print plastic objects, to generate conductive wires and to handle electronic components, the challenge to actually use the potential of such a machine lies in the design and control software. This chapter describes how the mechanical and electrical designs are integrated into a G-code which is directly executed by the printer.
Section 4.1 elaborates on the question of how to combine mechanical and electrical design in general and specifically for additive manufacturing.
Slicing is the fundamental step of generating an executable sequence of commands for a 3D printer from a model. An introduction into the slicing algorithm and data structures, including an overview of important software projects is given in section 4.2.
In the remaining sections, it is described how a schematic design can be integrated into the slicing process and user interface. Section 4.3 covers the import, data structures and graphical visualization of schematics within the slicing software. The following two sections explicate how the components (sec. 4.4) and wires (sec. 4.5) are physically integrated into the printed object by automatically generating appropriate cavities, channels and extrusions. Furthermore, several minor, but important details of the printing process are discussed, e.g. solid wire beds on sparse infill, retraction strategies and pin contact improvements.

4.1 Design Methods

Manufacturing an integrated 3-dimensional circuit generally requires a model of the object (mCAD), a circuit design (eCAD) and the transformation into an executable tool path by a slicing software, which can then be executed by the printer as G-code. At an early stage of this research project, one of the fundamental decisions was where to combine the already existing solutions. The integration of model and circuit could potentially be implemented right into one of the corresponding tools: CAD software, PCB design tool or slicer, or alternatively as an additional standalone application. The design decision to integrate mCAD and eCAD into the slicing software Slic3r [B26] is further explained and motivated in the following section.

Creating 3D-electronic designs manually with a CAD software is only feasible for simple test objects since it is laborious, very time consuming and has no reference to any electronic component data. A more promising approach is the creation of PCB layouts with a PCB designer and either deforming or combining them with a CAD software or to use multilayer PCB circuits with a subsequent registration step that maps each layer of the PCB to a corresponding slice. Both methods can benefit from the well-engineered PCB design software and use features like the existing component databases, electronic rule checking and simulations. However, this approach does not produce real 3D electronics because the final circuit is still limited to a combination or deformation, e.g. folding or wrapping around a regular body, of 2D PCB designs.

Standalone 3D electronic design solutions can simply design real 3D electronics without limitations for component positions and wire paths. They are very flexible due to their independence from surrounding tools like the slicer or the CAD tool. A problem that all these approaches have in common is the missing reference to the actual structure of the print. Without this reference, the designer cannot react to structural differences that 3D printed objects have and the slicer is not able to handle wires and components differently from the base materials. If slicing information is available, it can be used to ensure a predefined wire thickness, to prevent shorts, to create proper SMD pads, and to ensure the connection on intersections of wires without overfilling them. *Project wire* [B1] was the only implementation of this approach, the project was stopped by Voxel8 and AutoDesk by end of 2017. However, *project wire* never had an actual schematic design feature; the designer had to manually create linear circuit connections while placing the components inside of the object.

4.2 Slicing Software

This section provides an overview over existing slicing software projects and commercial solutions in 4.2.1. The choice for Slic3r as framework for this work is motivated. A general introduction into the fundamentals of slicing algorithms is given in 4.2.3 as a basis for the following chapters.

4.2.1 Existing Software Projects

A state of the art, general purpose slicer is a rather complex piece of software. Developing a new slicer clearly was neither feasible nor desirable within the scope of this work. The obvious decision was to modify and extend an existing software. Propelled by the enormous development of low-end and semi-professional 3D printers, ignited by the RepRap project [A38], a variety of slicers were developed in the last 10 years. Modifications of the slicer either require at least a very extensive plug-in mechanism or, better, access to the source code. Unfortunately, most existing slicers (Kisslicer, Materialise, Netfabb, Simplify3D, Voxelizer, SelfCAD, Pathio etc.) are proprietary, commercial products and therefore not suitable for modifications. IceSL [B15] takes a special role in that it is driven by a university research project, not exactly a commercial product and free to use, but also not open source. The most important and prominent open source slicers are introduced in the following.

Slic3r Slic3r [B26] was started in 2011 by Alessandro Ranellucci as a new STL to G-code generator under the AGPLv3 license. It was originally written in Perl, the core was successively ported to C++ to improve performance, the user interface still contains a substantial amount of Perl-code. Slic3r is still maintained and developed by an active community but increasingly suffers from the amount of legacy code and very long release cycles. The code used to be basically undocumented until recently, but currently receives some attention to generate appropriate in-line documentation. It provides a feature rich graphical user interface but can also be used from the command line or integrated as a library. Slic3r heavily relies on the Clipper library by Angus Johnson [B14] for polygon operations. Clipper is distributed under the Boost Software License.

Slic3r Prusa Edition The Prusa edition [B29] is a fork of the original Slic3r, developed by Prusa Research s.r.o. since 2016. It shares the same codebase but is specifically tuned for the printers Prusa Research sells. The Prusa edition contains a number of additional features.

CuraEnginge CuraEngine [B5] is developed by Ultimaker B.V. as part of the Cura software under the AGPLv3 license since 2013. It is a backend G-code generator, similar to Slic3r, but purely written in C++. It also uses the Clipper library for polygon operations. CuraEngine is state-of-the-art slicing software, supported by an active community.

MatterSlice MatterSlice [B17] is a C# port of CuraEngine, primarily used as slicing backend for the MatterControl 3D printing software suite, developed under AGPLv3 license by MatterHackers inc.

Others A number of outdated slicers is historically relevant, but not suitable as a basis for further developments. **Skeinforge** [B7] was an important tool in the early phase of the RepRap project, it was written in Python and inspired most of the modern projects. The Java based **RepRap Slicer** [B24] was another tool related to the early RepRap project stage. **Bread** [B3] is an experimental slicer for a recent research project to generate non-planar, three-dimensional layers. **ros_additive_manufacturing** [B4] contains a G-code generator for robot mounted extruders.

4.2.2 Slic3r Electronics Fork

Slic3r was used for this work because it is fully open source, has a very flexible, generic internal structure and an integrated user interface which is suitable to visualize a preview, not only of the G-code, but also of delicate electronic components and wiring details (fig. 4.1). It was also used in previous work for the implementation of my master thesis [A89] and a subsequent paper on adaptive slicing [A95]. The knowledge and experience with Slic3r, accumulated during those projects, outweighed the weak documentation and slightly slower execution performance compared to CuraEngine. Slic3r Prusa edition and MatterSlice did not exist when this project was started.

The original Slic3r repository [B26] was forked into a **Slic3r Electronics** repository [B36], which contains all algorithms and implementations related to slicing and wire routing described in the rest of this document. It is currently not planned to merge the electronics extensions back into the upstream software since only very few institutions have appropriate hardware to use it, but it would add significant complexity to the project, affecting thousands of users.

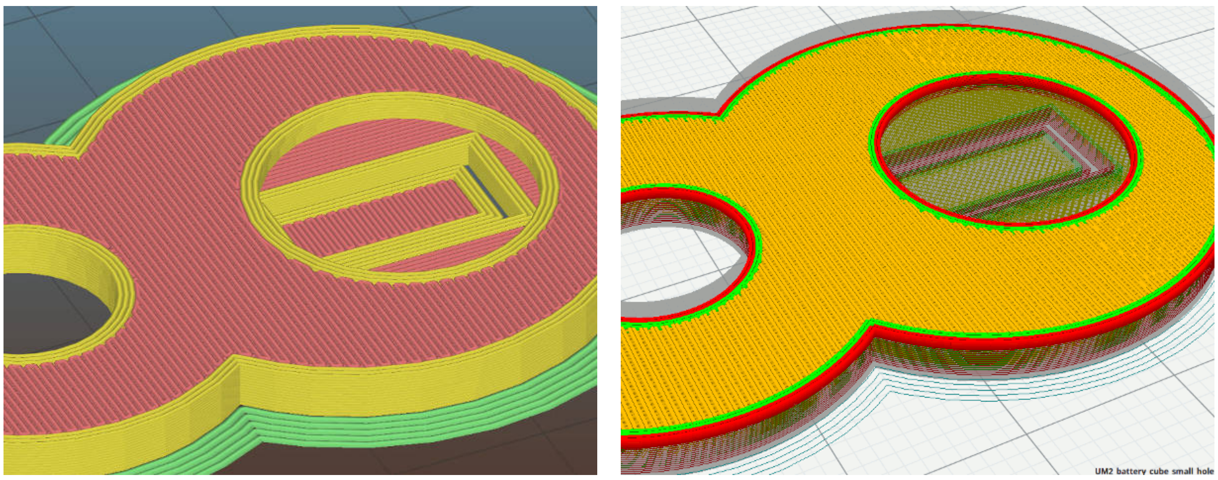

Figure 4.1 – Tool path visualization in Slic3r (**left**) and Cura (**right**). Individual extrusion lines and details are well recognizable in Slic3r's volumetric representation.

4.2.3 Slicing Software Fundamentals

The general working principle and architecture of slicing for FDM-applications is similar for most software solutions, with some exceptions e.g. octree-based approaches [A76] or direct slicing from CAD models or other sources [A37]. In the following, the slicing process is introduced in detail using the specific example of Slic3r.

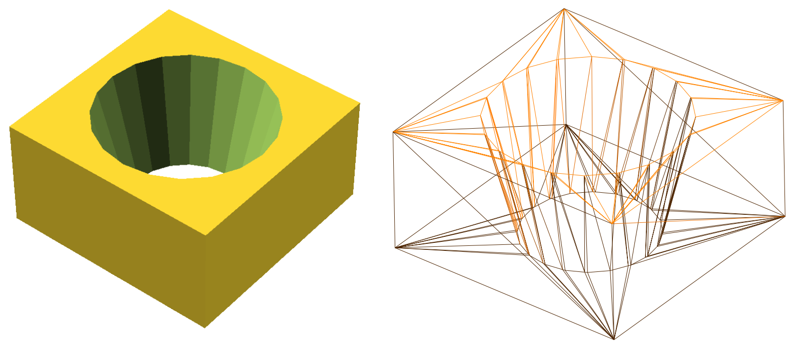

```
solid Example_Model
  facet normal -1 0 0
    outer loop
      vertex 0 0 0
      vertex 0 0 10
      vertex 0 20 0
    endloop
  endfacet
  facet normal -1 0 0
    outer loop
      vertex 0 20 0
      vertex 0 0 10
      vertex 0 20 10
    endloop
  endfacet
  ...
```

Figure 4.2 – Example of a tessellated CAD object as CSG model (**left**), wire-frame model (**center**) and ASCII encoded .stl-file (**right**).

The slicing process starts with a digital model of an object, usually encoded in the Surface Tesselation Language or Standard Triangulation Language (STL) format or a similar representation, where the surface of the object is approximated or *tessellated* by a (large) number of triangles as illustrated in fig. 4.2. The STL format is highly redundant since every vertex is encoded in at least three facets and contains no further topology information. The model is

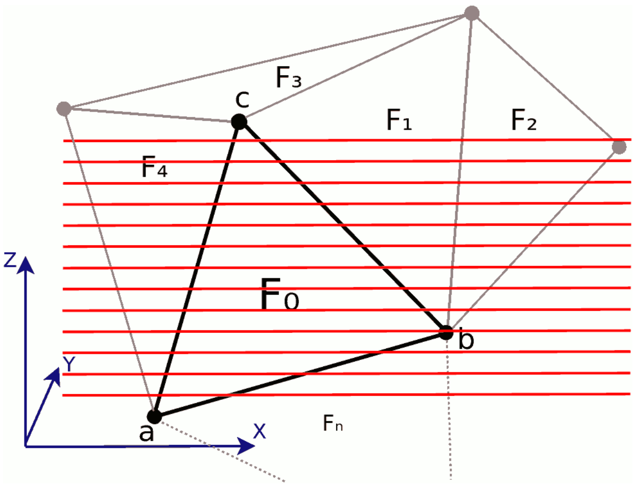

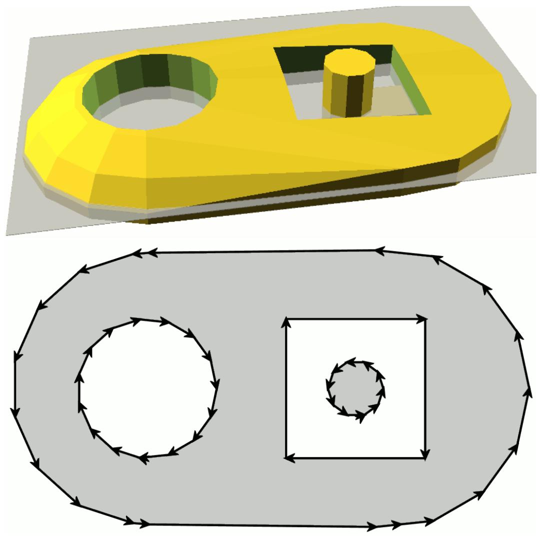

Figure 4.3 – **Left:** intersection of a single facet (F_0) with all horizontal x-y-planes (red) which represent the pre-determined set of layer-z-coordinates. This computation step can be done in parallel for each facet. **Right:** intersection of a single plane (top) and resulting nested polygon representation of one layer (bottom). The layer contains two islands (gray surfaces). By convention, the polygon orientation is CCW for *contours* and CW for *holes*. Note that the tesselation resolution is intentionally very low for this object to better clarify the representation.

therefore converted into a more sophisticated internal representation with explicitly modeled facet adjacency information.

Layer Generation

In the actual *slicing* step, the 3D-object is divided into a set of horizontal 2D-layers. This can be done layer by layer (e.g. with the *marching* algorithm [A66]) or facet by facet, computing the intersections of each facet with a set of pre-determined horizontal planes. In Slic3r, a set of z-coordinates is generated, which represent the position of the individual layers. For each facet of the model, the intersections with each of these z-planes is computed as illustrated in fig. 4.3 (left). The result is a an unordered set of horizontal lines for each layer. This approach allows good parallelization of the intersection operations since each facet is treated independently, but requires a subsequent sorting step to generate closed loops from the unconnected lines as the adjacency information is discarded.

For all further processing steps, the resulting loops of each layer are stored as a vector of nested polygons (*ExPolygons*), containing exactly one outer polygon (*contour*) and a number of inner polygons (*holes*) as depicted in Fig 4.3 (right). These nested polygons are usually referred to as *islands* or *LayerParts*, they represent parts of the same object which are unconnected at the given layer, e.g. two pillars of a bridge. By convention, *contours* are stored in counter-clockwise orientation, *holes* in clockwise orientation, with the material always being on the left side. A single object may consist of different materials and it is also possible to define regions e.g. for a different infill-strategy to achieve high stability where required, but reduce the weight otherwise. This is covered by subdividing each layer into *LayerRegions*. This is basically a vector, where each *LayerRegion* contains the respective *island* polygons. *LayerRegions* are only mentioned for the sake of completeness, for this thesis, we always assume a single material object.

Vertical Shells

The object is now represented by a stack of two-dimensional surfaces. To generate an individual surface with a printer, a 0-dimensional circle (nozzle) is moved around, depositing a 1-dimensional strand of plastic. Printing a single layer is done in two steps by first following the contour to create a smooth surface and then filling the remaining area with a repeating pattern (*infill*). The contour loops (*perimeters*) are found by repeatedly applying a negative offset to each nested polygon as depicted in fig. 4.4. The offsetting computations are executed by the clipper library based on Vatti's polygon clipping algorithm [A87, A12, A1].

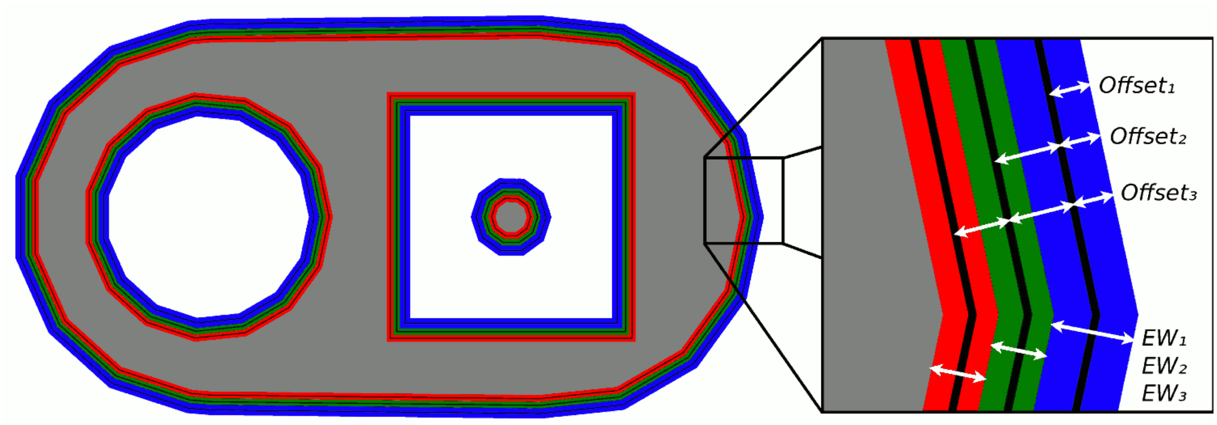

Figure 4.4 – Generation of perimeter extrusion loops by multiple offsetting of the contour polygon (gray). The colored regions each depict the surface covered by a single extrusion loop with the G-code-coordinates overlaid in black. The `extrusion_width` of the external perimeter EW_1 can be different from the other perimeters EW_2, EW_3 to achieve better surface quality.

Figure 4.4 also illustrates how the amount of offset for each extrusion loop is computed. Slic3r uses two `extrusion_width` parameters for perimeter loops: EW_{ext} for external perimeters and EW for all other perimeters to potentially achieve a better surface quality with thicker or thinner extrusions. For the first (most outward) loop, the polygon offset computes as:

$$\text{Offset}_1 = \frac{EW_{ext}}{2}$$

to achieve a path in the center of the extrusion area (blue). For the second line:

$$\text{Offset}_2 = \text{Offset}_1 + \frac{EW_{ext}}{2} + \frac{EW}{2}$$

and for all further loops:

$$\text{Offset}_n = \text{Offset}_{n-1} + EW$$

Horizontal Shells

The remaining interior surface of each layer is then filled with a repeating pattern (*infill*), where the amount of material can be gradually controlled by setting the pattern-distance to either fabricate strong, solid objects or reduce the printing time and weight. While the vertical shell-regions of an object are implicitly solid by printing the closed perimeter loops, horizontal shell surfaces must be identified and printed with solid infill in an additional step. Figure 4.5 illustrates the identification of solid infill areas at horizontal shell regions. Areas which are not covered by the next layer should be filled with a solid pattern. These areas are found by computing the difference between the surfaces of a given layer and the next layer. To allow for thicker shells, this step is repeated over several layers. All differences are accumulated and the resulting area is marked as top solid. The same scheme is applied to identify bottom shells, overhangs, bridges and regions which require support.

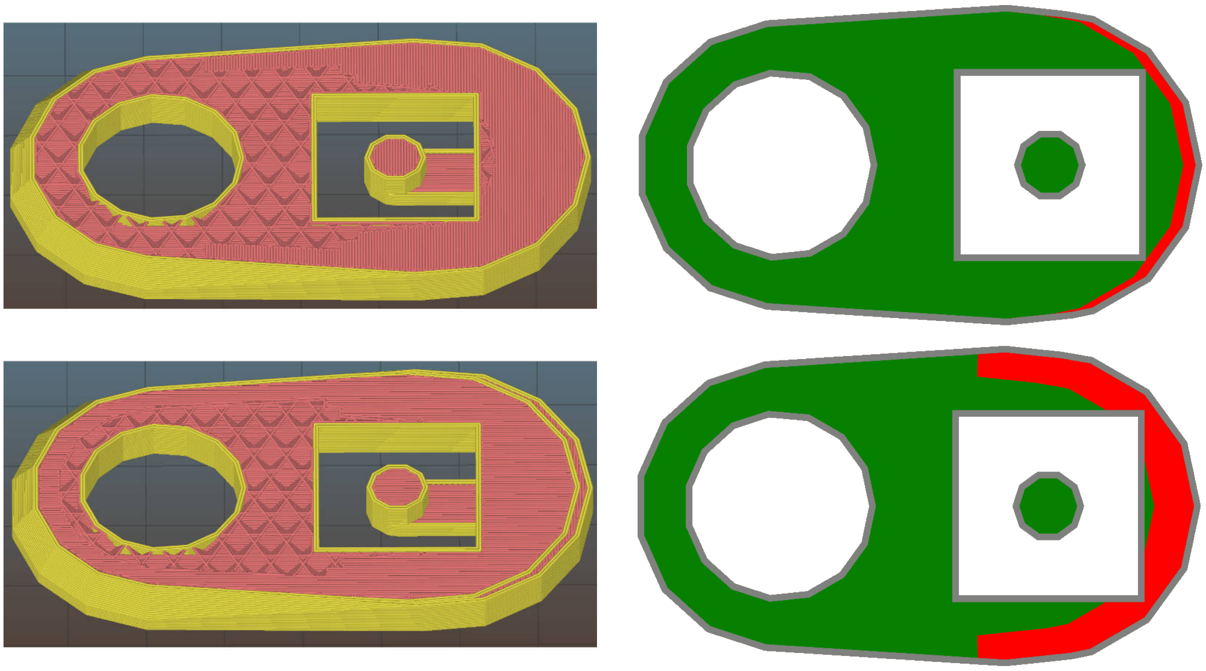

Figure 4.5 – Generation of solid horizontal shells. For a given layer (**top left**) the difference to the next layer (**bottom left**) is computed (red area in **top right**) and filled with a solid pattern. Since a shell is usually supposed to be thicker than one layer, this step is repeated for the next n layers. After accumulating all differences, the layer is filled with sparse infill (green) and solid infill (red) as indicated in the last image (**bottom right**).

Optimizations

For complex model geometries, the slicing process requires significant computational resources and time. Compared to the printing time, the computational processing time is usually negligible, but the user experience is considerably better with short response times. When preparing a printjob, the user often tweaks several parameters until the tool path preview gives a satisfying result, repeatedly causing the slicer to execute the full slicing chain. Not every parameter requires a full re-slicing. Increasing the number of perimeters for example does not change the layer positions and outline polygons, but has an effect on the infill generation. Changing the brim configuration has no effect on the rest of the slicing process at all. To reduce the amount of redundant computations, the process is divided into a sequence of steps, depending on each other. When a parameter gets changed, only the related step and all subsequent steps are invalidated and re-executed. For each individual object in a printjob, the following steps are executed:

`Layers` determines the position and thickness of all layers. The result is a vector of z-positions, indicating where the object will be cut into slices.

`Slice` computes the intersections between the set of planes from the previous step and the object model. Result is a vector of nested polygons (*LayerParts*).
`Perimeters` generates a set of extrusion loops by offsetting the *LayerParts*.
`DetectSurfaces` split the remaining interior areas into regions with different filling strategies for sparse internal and solid external infill.
`PrepareInfill` detect bridges, combine infill regions over multiple layers etc.
`Infill` generate the actual infill pattern extrusions.
`SupportMaterial` compute the pairwise difference of adjacent layers to identify overhanging regions and generate a supporting structure.

Additionally, most computationally intensive operations can be executed in parallel on suitable hardware. Parallelization is mostly done on a per layer- or per facet-basis (for the first slicing step), since layers are mostly independent from each other.
The slicing process can be either triggered manually or executed automatically upon invalidation of the current configuration when the user changes a parameter. The automatic execution is called *background slicing*. The idea is to reduce the response time. In an optimal case, the result is immediately available and visualized. However, for complex objects the user interface may become unresponsive and the computation load is very high. For the integration of electronic components, background slicing is heavily used to update the resulting placement and wire routes after each manipulation.

G-code Export
Actual G-code instructions are only generated upon export of the final result. The tool path preview is rendered from internal extrusion representations only. Producing an executable G-code sequence from the geometric model of material extrusions requires the consideration of a variety of additional aspects, including but not limited to: temperature control for nozzles and printbed, travel moves, amount of material per extrusion segment (*flow*) and cooling. The G-code file is created from bottom to top, layer by layer. If multiple objects are printed in a single printjob, each object has its own set of layers. The layers of all objects are sorted by their `print_z` position and interleaved. Multiple copies of the same object are generated by "cloning" the G-code statements and only translating their x- and y-coordinates.

4.3 Import and Representation of eCAD-Data

The integration of electronics into a 3D-object requires a mechanical model of the object (mCAD) and a definition of the circuit (schematic diagram, eCAD). Importing a 3D-model into Slic3r from an .stl or similar format is a basic functionality, discussed in sec. 4.2.3. Similar to the 3D-model data, the import of schematics is split into an import function which can be adapted to different file formats and a common internal representation. The import mechanism was originally written by Daniel Ahlers [A2] and extended for this work. It currently only supports EAGLE [B12] schematic (.sch) files. Such a schematic definition mainly contains a `partlist`, a `netlist` and package information for each component, encoded in an XML-format. A `part` describes the physical shape and pins of a specific component. A `net` basically holds a list of connected pins with equal electric potential, representing an electric connection. EAGLE stores spatial layout and routing information in a separate file which is not used at all for 3D-electronics.

As illustrated in fig. 4.7, the internal schematic representation is similar to the imported structure, but contains additional semantic information. A single printjob can contain several physical objects which are arranged on the printbed and printed in parallel. Each physical object representation is extended by an assigned `Schematic` class, which serves as a central access point to all electronics related data and provides import and export functions. The `Schematic` object holds a `Netlist` and a `Partlist`, similar to the imported data structure. The `Partlist` object provides geometric information about every component for the creation of cavities and visualization. It also holds the 3D-position of placed components which are stored relative to the mCAD coordinate system.
The `Netlist` holds a list of 3D points, representing the geometry of wires, organized in a graph data structure for each individual net. The graph vertices are either `pins`, representing the pins of a component, or user-generated `waypoints`. Edges represent direct, wired connections between two pins. Upon initialization, the graph contains no edges and only `pin` vertices from the imported .sch-file.

Figure 4.6 demonstrates how unwired connections are represented by `rubberbands` in the user interface. To generate those rubberbands, all *connected components* of the graph are computed by a Depth First Search (DFS) based algorithm. The shortest spatial connection between each pair of components is found subsequently and visualized by a rubberband (black). New waypoints and connections are created by double clicking an existing waypoint (red) or rubberband and extending to an arbitrary point in 3D-space or an existing waypoint of the same net. Components, waypoints and wires are deleted by a double-right-click.

Both `Netlist` and `Partlist` can be exported into a custom .3de-file to store the 3D arrangement and routing of a schematic in a printable object. The .3de-file only provides additional positioning and routing information and is linked to the original .sch-file, similar to a common PCB layout file. This separation of circuit and layout information allows for later modifications of the schematic. Additionally, the eCAD definitions are technically independent from the mCAD model, also allowing for modifications of the physical shape of an object.

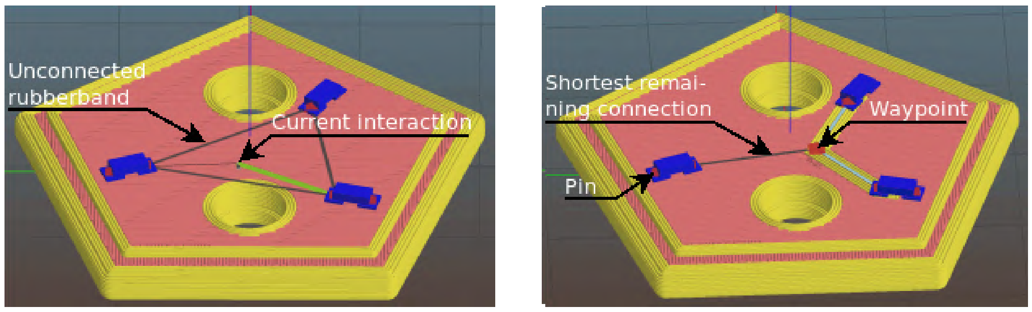

Figure 4.6 – Rubberband representation of a net. **Left**: unwired gnd-connection of 3 LEDs. The green line indicates the resulting wired connection for the current ongoing interaction. **Right**: the same net, partly wired. The left LED is only connected to the wired part of the net by the shortest rubberband possible.

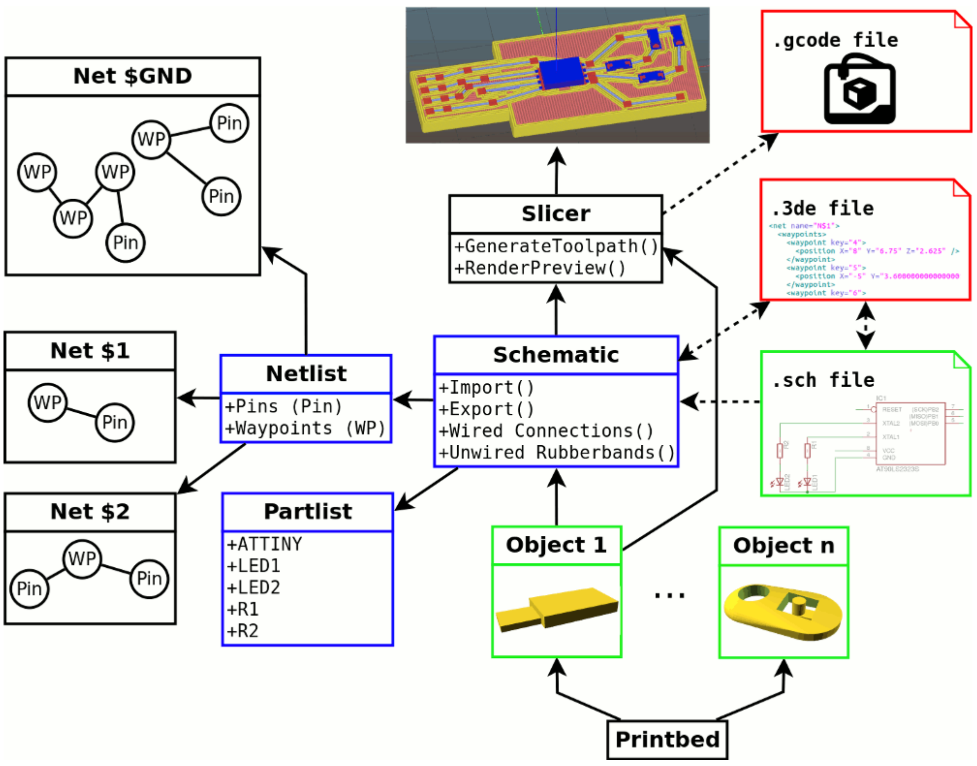

Figure 4.7 – Architecture of the internal representation of electrical circuits and components. Each mesh object on the plater holds an individual schematic object which imports the circuit information from an EAGLE netlist (green input files). The schematic object itself holds a partlist with component geometries and positions and a netlist for electric connections. Each net is stored in a graph representation, containing the position of connected component-pins and user generated waypoints. Position- and routing-information can be exported to an additional .3de-file which extends the original .sch-file (red).

The concept of a meta-format for 3D-electronics which aggregates and augments models from different domains without duplication of the respective model information is similar to the Prostep ivip PSI ECAD/MCAD Collaboration format (.idx) [B6]. The .idx-format was established by a consortium of major CAD software companies to facilitate exchange between different specialized products, with a focus on spatial arrangement of conventional electronic components. The Approach is described in a whitepaper [A18]. The standard is actively developed by the "ECAD/MCAD-Collaboration" forum, new versions are released iteratively.

4.4 SMD-Component Integration

The first step of integrating a circuit into a 3D-object usually is to set the positions of components, followed by routing the wires. The geometric shape of the component's body and pin positions is provided by the imported schematic definition, either as rectangle or polygon. For most standardized package formats (e.g. 0805, SOP, QFP) the component height is not explicitly specified and must be provided by the user.

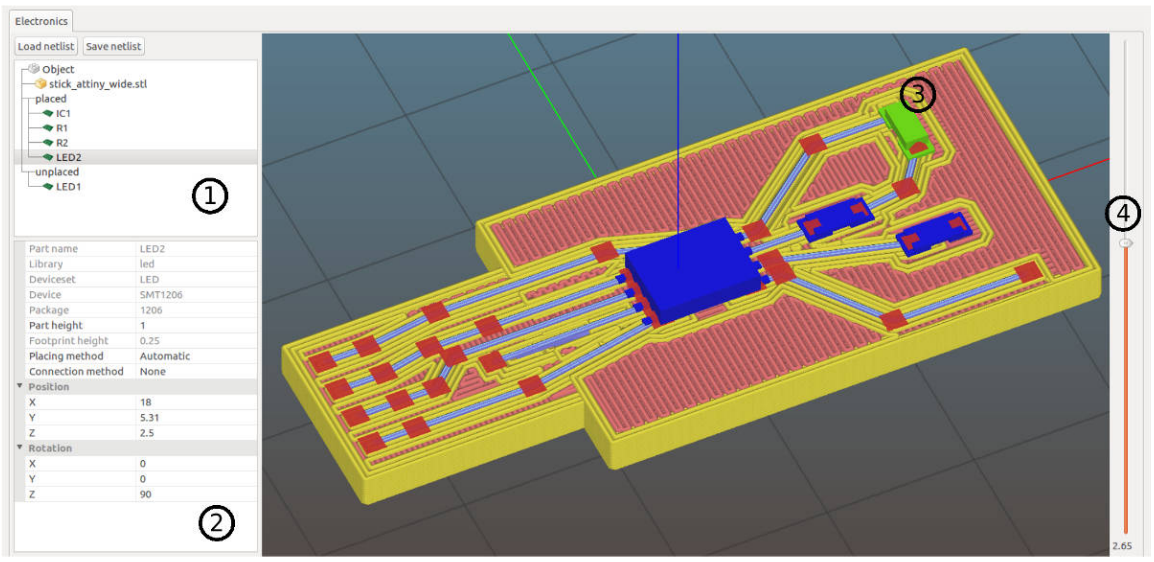

Part name	LED2
Library	led
Deviceset	LED
Device	SMT1206
Package	1206
Part height	1
Footprint height	0.25
Placing method	Automatic
Connection method	None
▾ Position	
X	18
Y	5.31
Z	2.5
▾ Rotation	
X	0
Y	0
Z	90

Figure 4.8 – Tool path visualization of a single object, augmented with the representation of electronic circuits. The sidebar contains a list of all placed and unplaced components (1) and a dynamic grid (2) with details of the selected component or waypoint (3, highlighted in green). Positioning of a component or new waypoint is done with drag and drop on the currently selected top layer. The slider on the right (4) allows to browse through the object layers. Exact positioning and rotating can be done by modifying the values in the detail grid.

Visualization

Slic3r's tool path visualization was extended to additionally display rubberbands, waypoints and SMD-components as illustrated in fig. 4.8. Unplaced components are positioned in an object by dragging them from list on the left to the surface of the currently displayed top layer. The exact position and rotation can be refined in the detail information grid on the lower left of the screen. The fader on the right indicates the current z-position and can be used to vertically browse through the generated layers. To visualize the components, individual meshes are composed from the footprint information by merging tessellated geometric primitives for all pins and an extruded body outline into one object which can be displayed by the OpenGL-based rendering engine. The existing STL-library was used to store the generated meshes and to perform rotations and translations.

Generation of pockets or cavities.

Unless a component is placed on the surface of an object, a pocket or cavity is required to embed the component into the printed material. Cavities can either be part of the mCAD-model or generated dynamically during the slicing process. Explicit modeling of cavities offers more design freedom, e.g. the battery slot in fig. 7.4 is shaped in a way that it also serves as a mechanical switch, but typically requires significantly more effort, especially when the component position needs to be modified later. Cavities designed in the mCAD-model also do not respect any process parameters.

Hence, for this work, the dynamic approach was chosen. The generation of cavities can be done very early in the slicing process by modifying the original part model mesh prior to the layer generation step (`Layers`), or by inserting holes into the *LayerPart*-polygons between the

`Slice` and `Perimeters` steps. Figure 4.9 illustrates the dynamic generation of cavities as it was implemented into Slic3r. Once the *LayerPart*-polygons are generated, the algorithm iterates over the list of all placed components and removes the convex hull polygon of the component from each affected layer. The areas right below and above a cavity are marked as top- / bottom-surfaces during the `DetectSurfaces` step and therefore get automatically filled with a solid pattern, creating a smooth, reliable bed and cover for the component.

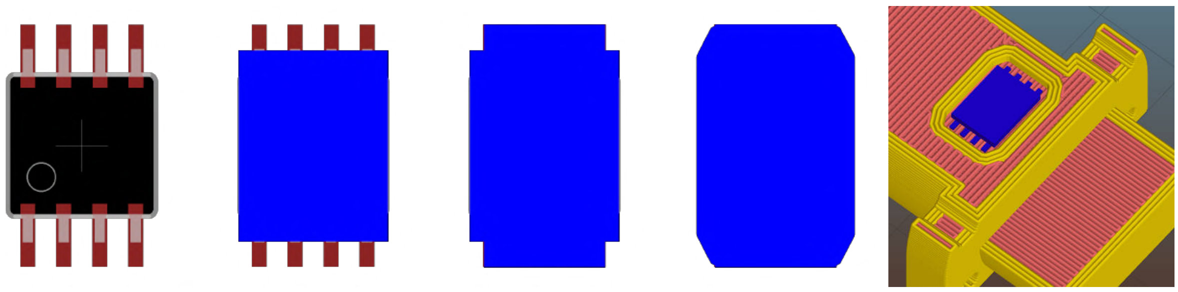

Figure 4.9 – To produce a cavity for a SMD-component, the part geometry from the imported .sch-file (**1**) is utilized. The convex hulls of the body (**2**) and pins (**3**) are combined (**4**), an additional tolerance offset is applied and the resulting polygon is removed from all affected layer surfaces (**5**).

Generating a slot for an electronic component is considerably easy if the component is placed on its pins or flipped to its back (fig. 4.10, **1**). A polygon, generated from the convex hull, can be applied to every affected layer, leaving enough space to later fit the component into. An additional, user configurable offset is applied to achieve a sufficient tolerance. If the component is rotated irregular, the ground of the slot must fit the components rotated geometry, but the top must be flat and have at least the size of the projected convex hull polygon to allow the insertion of a component and to avoid collisions with the extruder after placing, as illustrated in fig. 4.10, **3** and **4**. For a given layer, this is achieved by generating a convex hull polygon from the rotated component geometry for this layer and computing the union of all component hull polygons from the lower layers.

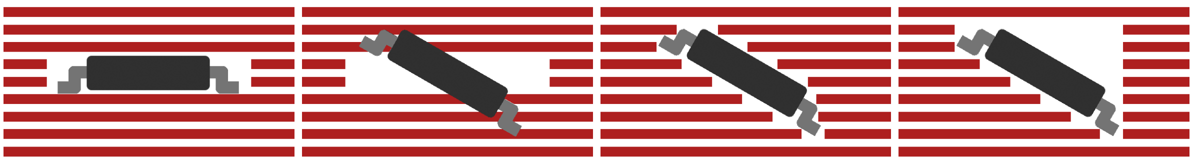

Figure 4.10 – Subtraction of SMD components from the printed object to create cavities. From left to right: **1**: outline subtraction, **2**: part rotated but subtracted outline generated from flat footprint, **3**: naive polygon subtraction with rotation, **4**: accumulating polygon subtraction with rotation.

Component placing

Once the position of components has been set and cavities are inserted to the G-code, placing instructions are added to control the automatic pick and place process.

During the G-code-generation, after each layer the list of SMD-components is checked for components which are placed in the object, but not yet processed (printed) and whose upper surface is below or at the current `print_z` value. The component is flagged as `printed` and a placing command is appended to the G-code, depending on the placing method selected by the user:

Automatic Appends a "`M361 P<partID>`" command to trigger a fully automatic placing operation as described in sec. 3.2.2.

Manual Appends a "`M117 Insert component <partID>`" command to notify the user that a manual interaction is required. `M117` simply displays a message at the screen. Additionally, a custom G-code snippet is appended to pause the printer, e.g:

```
G28 Z0 ; Home Z-axis for better accessibility
M0     ; Pause printjob, press button to continue
```

No placing Only appends a comment to notify the user that this component will not be placed at all. Omitting a component during the print process can be useful if it is located at a surface and supposed to be assembled in a subsequent processing step, e.g. for a vertical component which can not be placed by the vacuum gripper.

Finally, a list with required information for all processed components is appended as described in sec. 3.2.2 and the `printed` flags are reset.

Performance considerations
Since changing the position of a component requires a re-generation of the tool path to visualize the result, performance is critical for the user experience. Often, only a small region of the object is affected by such a change and a full re-slicing would introduce significant overhead. Modifying polygons on a per layer level allows for dynamic re-slicing of only a few layers, when a component is modified by the user. To achieve this, the original surface polygons must be stored to preserve the information that would be lost during the modification otherwise.
After each user interaction, all layers which are affected by the modification are marked "dirty" and the slicing chain is triggered, starting with the `Perimeters` step, as the original *Layer-Part* polygons are already generated. All subsequent steps are layer-based and simply return immediately for clean layers. Finally, all dirty flags get removed.

Unfortunately, slicing only affected (dirty) layers causes several concerns. Combined infill affects multiple layers and must either be disabled for partial re-slicing or adjacent layers must be also marked dirty, up to the maximum number of combined infill layers which is limited by a configuration parameter and the maximum printable layer height.
If the modified component is already connected by wires, those have to be re-generated as well. While this is possible for static wire generation by following all connected wire to the first fixed waypoint, it is not predictable which layers are affected by dynamically generated wires as described in sec. 5.3.

4.5 Wire Integration

This section introduces the algorithmic core-concepts of the thesis, the generation of conductive connections within a printed object. Section 4.5.1 lays the groundwork by introducing the basic concepts of waypoint based linear routing of wires over multiple layers. The generation of actual physical channels and extrusion paths is then detailed in section 4.5.2, this also includes strategies mitigation of defects and considerations to improve pin contacts. Once the basis is established, the next chapter 5 elaborates on dynamic routing approaches, incorporating the physical topology of objects and wire self collisions, while preserving printability.

4.5.1 Static Wire Routing

All wires connecting the individual components are stored in the `Netlist` object, represented by an acyclic undirected graph as introduced in sec. 4.3. The "rat's nest" of placed but currently unwired components is visualized by a set of rubberbands. The routing of wires through the 3-dimensional object is divided into two steps: the high-level generation of "waypoints" to define the desired routing paths and the low-level routing of a single line between each tuple of waypoints. This concept allows for a certain level of decoupling between the classic routing task of finding a collision free partitioning of the available space given a number of constraints, and the process related task of finding a set of suitable extrusion paths given a specific printer's parameters.

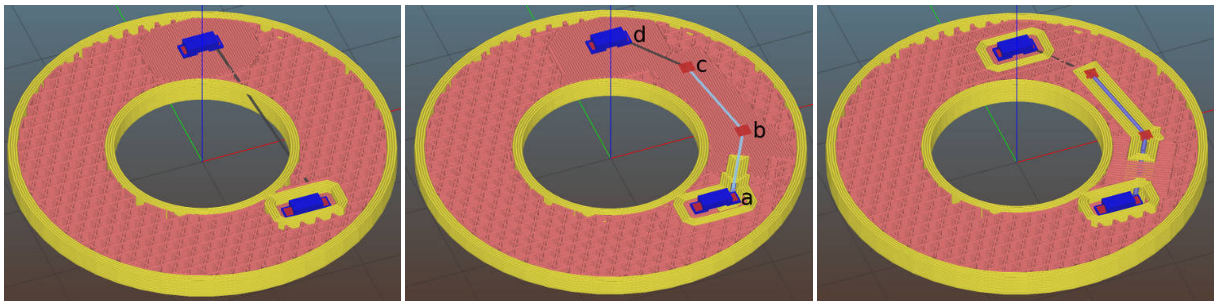

Figure 4.11 – Generation of static wires. The unwired connection is represented by a rubberband (left), the route is defined by setting waypoints (a–d). Segment $[a, b]$ crosses several planes, segment $[b, c]$ affects only a single layer, $[c, d]$ remains unwired.

The following algorithms focus on the second task, where a set of waypoints is manually defined by the user. Figure 4.11 illustrates how a single wire is represented by a sequence of waypoints $w \in \mathbb{Z}^3$ where usually the first and last waypoint are determined by the pin positions of connected components. A wire segment $s = [a, b]$ is the direct line between two subsequent waypoints a and b. Note that waypoints are represented in scaled integer coordinates to avoid numerical instabilities (cf. sec. 5.2.1).
Figure 4.12 illustrates how the low level routing step computes a set of extrusion skeletons for each layer from the 3-dimensional set of waypoints. This process is similar to the `Slice` step which divides an object into a stack of 2.5-dimensional layers by computing the intersection of a set of planes with the tesselated mesh representation. For a given layer L and each wire s, the intersection of the first point's x-component a_x with the lower and upper boundary L_b, L_t is computed by

$$a'_x = \begin{cases} a_x + (b_x - a_x) \cdot \frac{L_b - a_z}{b_z - a_z} & \text{if } a_z < L_b \\ a_x + (b_x - a_x) \cdot \frac{L_t - a_z}{b_z - a_z} & \text{if } a_z > L_t \end{cases}$$

and correspondingly for a'_y and the second point b, resulting in a 2-dimensional set of lines. This step is trivial for horizontal wire segments, where the intersection equals the planar projection of the original wire. For inclined wires, the end points of the resulting line are then extended by

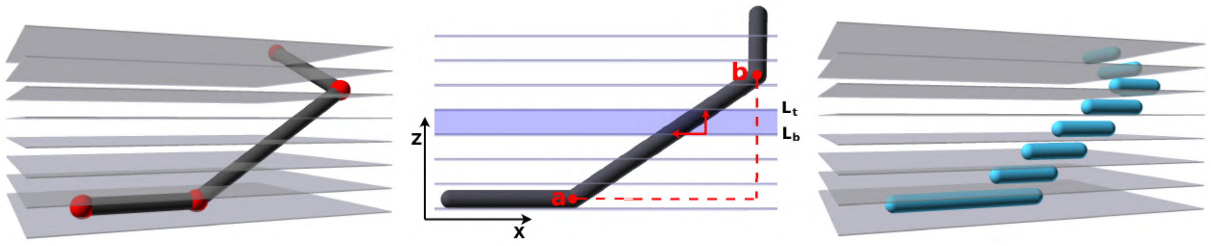

Figure 4.12 – Generation of extrusion paths from a wire routed in 3D-space. **Left**: three wire segments (black) are defined by a set of waypoints (red), the slicing layer boundaries are indicated as gray planes. **Center**: for inclined segments, the intersection with the upper and lower boundary of each layer is computed to generate a horizontal section. **Right**: sections from inclined segments are extended to achieve reliable inter-layer contact points, resulting in a "staircase".

a user defined offset to achieve a stable, overlapping, inter-layer connection to the adjacent wire sections as illustrated in fig. 4.12. The result of this routing step is an unordered set of extrusion lines per layer which requires further processing as described in the next section.

4.5.2 Channel Generation

The static wire routing step as described in the previous section produces a set of unordered, horizontal lines per layer. Actually printing a conductive trace with a direct write extruder requires several additional steps to generate channels and a reasonable volumetric extrusion of material.

Extrusion trajectories
In a first step, the unordered lines are sorted to obtain continuous, printable polylines. This is trivial unless three or more pins are connected to the same net, inducing a junction as illustrated in fig. 4.13. Extrusion paths which can be printed as a continuous line are assembled by:

1. Finding an endpoint. Iterate the set until the first line with at least one endpoint which doesn't coincides with any other endpoint. Remove this line from the set.

2. Traversing adjacent lines until finding a point which coincides with 0 (endpoint) or more than 1 (intersection) other points and removing the lines.

3. Repeat steps 1-2 until the set is empty.

The trajectories are then printed in reverse order, such that the continuous line (the blue line in fig. 4.13, **3**) is printed first and all other traces terminate at the junction point to avoid crossing the same point multiple times.
The polylines can now be directly used as trajectory for the direct write extrusion. However, the starting point of a an extrusion path tends to be not reliable after a retraction move. The plastic- and conductive ink extruder are in alternating use for every layer, therefore typically the first conductive line at each layer is printed after a relatively long period of inactivity. Since wires consist of only one single trace, even a small air-gap is catastrophic. A few simple countermeasures are implemented to mitigate extrusion defects:

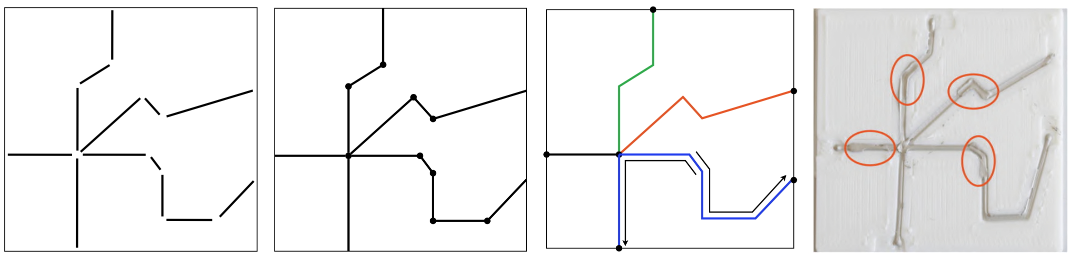

Figure 4.13 – Generation of extrusion paths for a single layer. From left to right: **1**: Wire segments from slicing. **2**: Assembling a connected graph from unordered segments. **3**: Re-fragmentation at junctions, thin black arrows depict directions of overlapping extrusions. **4**: Printed layer. Overlapping regions to ensure extrusion towards the SMD-pads are marked in red.

- After each toolchange the conductive ink extruder is primed by dumping a small amount of material and wiping the nozzle tip at a silicone blade.
- Each trajectory is split into two segments and the extrusion is executed from the center of the line towards the end to achieve reliable extrusion at the SMD-pad. The segments are extended at the starting point by a user defined offset, generating a small overlap at the center of the line. Possible over- or underextrusion only occurs at non-critical spots in the object (see fig. 4.13, **4**).
- The extrusion polylines are sorted by length, starting with the longest trajectory to maximize the distance between overlap and endpoint. Trajectory splitting can be disabled by setting the overlap parameter to 0.
- Priming the extruder is most important after a toolchange. Hence the amount of overlapping can additionally be increased only for the first segment of each layer to minimize double extrusions.

Channels

The resulting polylines are then used to generate channels for the wires by removing material from the respective layers, similar to the cavity generation step described in sec. 4.4.
Channels for the wires are generated by offsetting the polylines and subtracting the resulting polygon from the current layer. The offset value amounts to $\frac{e+\Delta}{2}$, where e is the extrusion width of the conductive material extruder and Δ is an additional offset value provided by the user for clearance. The result is illustrated in fig. 4.14, Layer 17.
One fundamental issue when applying fine ink lines on a printed surface is the surface roughness, which is inevitable for the FDM-Process due to the working principle of plastic, extruded by a single nozzle. If the wire is not aligned with the printed lines of a surface, ink tends to spread along the recesses resulting in electrical shorts as described by Espalin et al. [A19]. For inks with a higher viscosity, the extrusion breaks off when crossing a surface peak or valley, resulting in disconnected electric connections. Typically, objects are fabricated with "sparse" infill to reduce printing time, weight and material consumption. Obviously, printing a wire on sufficiently sparse infill with a typical ratio of less than 50% plastic material makes the problem even worse. Printing a wire on such a surface is generally impossible.
Espalin et al. introduced an additional processing step by CNC machining pockets and channels into the half-finished FDM-printed object to achieve highly precise and smooth surfaces. To avoid the expensive integration of a second process into the production chain with requirements

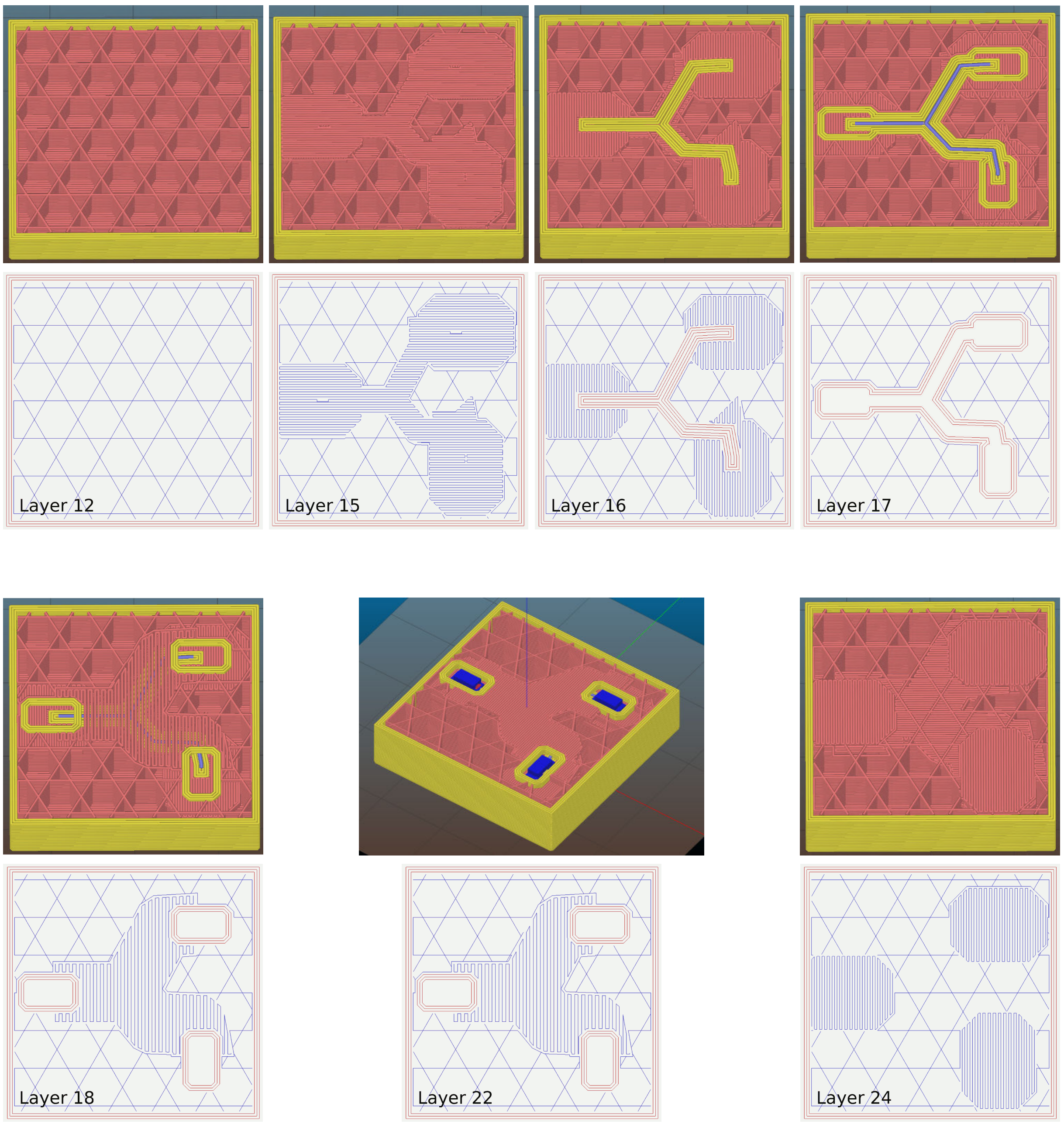

Figure 4.14 – Different layers of a tool path with integrated electronic components and wires, illustrating the steps for channel and cavity generation. **Layer 12**: Internal layer with sparse infill (density 20%). **Layer 15**: Several layers of solid infill to create a closed surface for wires and components. **Layer 16**: Layer directly below wires and components. The internal perimeters (yellow) serve as a smooth “substrate” for the wires, well aligned with the extrusion path of the conductive material. **Layer 17**: Channels and cavities are generated for the extrusion of wires and placing of components. **Layer 18**: Channels are covered by a region of solid infill. **Layer 22**: Placing of components. **Layer 24**: Components are also covered by a region of solid infill, providing reliable mechanical adherence.

for transport of the work piece and registration at both machines, a different, software-driven approach was chosen.

For each layer L, a "substrate" is generated by offsetting the polylines only by a small value ϵ and subtracting the resulting polygon from the contour of the preceding layer L_{-1} as illustrated in fig. 4.14, Layer 16. This opens a very small hole in the surface, causing the generation of a perimeter around the hole where the "gap" at this center is precisely aligned with the wire.
The opening created by this step (fig. 4.14 Layer 17) implicitly causes Slic3r to detect a `TOP` surface which is not covered by the next layer. Thus, the respective region is covered by a few layers of solid infill, serving as a closed surface over the otherwise sparse infill. The number of solid layers is determined by the user defined shell thickness for the overall object. The channels and cavities are covered by solid infill in the subsequent layers analogously (fig. 4.14 Layer 18 / 24)

Pin contact and G-code generation
A number of minor, technical issues arose during the first attempts to actually print objects with integrated electronics. Most problems were either related to insufficient calibration or to details regarding the electrical connections of SMD-components and G-code generation. The calibration of all components in the prototype printer is covered in section 3.3.
The following optimizations were already implemented or should be considered for future evaluation to increase the reliability of electrical connections:

Pin contact extensions The conductive ink currently provides both mechanical and electrical connections for SMD components. It is important to maximize the contact area at each pin while preventing shorts caused by excess conductive material. Unfortunately, the exact pin dimensions are not included in the EAGLE libraries for most components. Only the pad dimensions for the recommended "landing pattern" are provided, as they are mainly used for PCB layout. For optimal results, the libraries should be customized to include the exact pin dimensions.

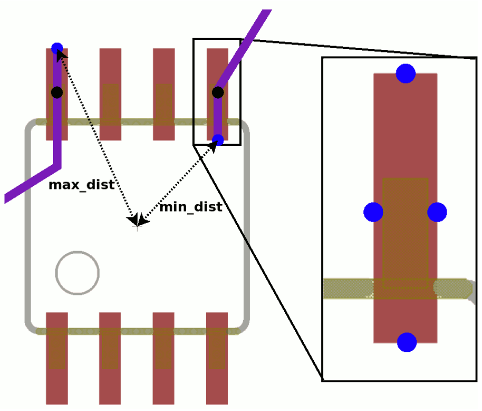

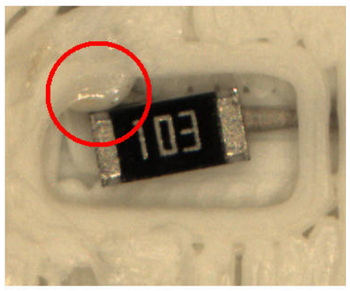

Figure 4.15 – **Left**: Extension of conductive traces to improve SMD-pin contacts. A wire (purple) is directly routed to the waypoint at the center of each pin (black dot) and depending on the entrance angle, extended to the opposite edge (blue dots) which is found by computing the min- / max-distance of all four edges to the center of the component. **Right**: Misplaced component caused by unretraction artifacts at the perimeter of a cavity.

To improve pin contacts, conductive traces are extended to the opposite edge of the pin (or actually the opposite edge of the landing pad), depending on their entrance position as illustrated in fig. 4.15.

Pin contact points A second problem, primarily related to component adhesion, is drying or curing of ink before the component is placed. Details on the curing characteristics are provided in section 3.1.3. Components are often placed several layers after the conductive connections were printed. To improve adhesion in those cases, small droplets of fresh ink can be dispensed right before the component is inserted. This is only possible if the ink dispensing nozzle is small enough (e. g. needle tip) to preclude collisions with higher layers, as the nozzle tip must be positioned below the current `print_z` surface. Additionally, the ink extruder must have sufficient clearance to all other extruders, which is granted in our case since the conductive ink extruder is mounted on an individual z-stage and lowered sufficiently for this operation.

Slic3r is designed for a layer-based, horizontal data structure and has no model for vertical extrusions. A new `ExtrusionEntity` model was implemented which provides vertical extrusion of a single line for a given height. The layer thickness of the first layer affected by the cavity cutout is used as height of the vertical extrusion. Pin connection options can be set per component to add droplets right after the connecting wires were printed, immediately before placing the component or disabled entirely.

Additionally, the component adhesion could be improved by also dispensing contact points for unconnected pins. This is not implemented yet.

Wire bed endpoints Wire beds ensure a smooth, solid and well aligned substrate for the deposition of conductive material. For SMD components with multiple pins this raises a problem, as every endpoint generates its own extrusion loop inside of a the small area under the component. Figure 4.16 illustrates how this can lead to a high number of small gaps and retraction movements if the extrusion width does not happen to by a multiple of the pin distance. Both gaps and particularly unretration movements result in a highly irregular and unpredictable surface structure. To mitigate this effect, it is considered to introduce a new surface type which generates a solid surface under components, where the infill pattern is aligned with the main direction of the pins. Such a surface could be printed in a single run. A smooth but not perfectly aligned surface is still preferred over unpredictable gaps and blobs.

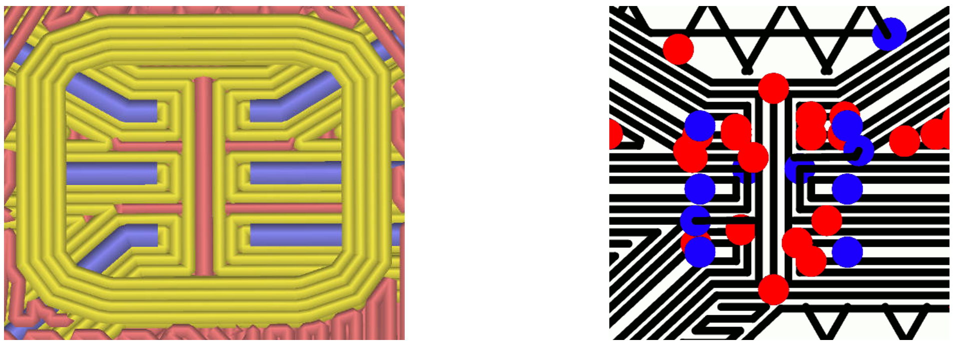

Figure 4.16 – Endpoints of wire beds causing a very irregular surface under multi-pin components (left). Gap filling leads to a high number of retraction and unretraction movements (right).

Unretraction strategy Channels and cavities by design are enclosed by perimeter extrusion loops. Entering such a loop requires an unretraction move which is prone to cause blobs, increasing the risk of interrupted conductive extrusions and component placement failures as shown in fig. 4.15, right. The precision of unretractions decreases after long travel moves and extruder changes. Minimizing travel moves and extruder changes prior to extrusion loops in the immediate vicinity of electronic components has the potential to mitigate the effect.

The actions described above are part of the tool path generation itself, the effect is already visible in the preview. At the stage of actual G-code-generation, some additional modifications were required to reliably print conductive paste with a syringe extruder:

Extruder ordering For multi-extruder setups, extruders are usually used in alternating order, but with minimal extruder changes. Consider the example of two colors, white and black, both colors are used at each layer. At the end of layer L_i, the black extruder is active. The next layer L_{i+1} is then started with the black extruder as well and finished with the white extruder to avoid the additional change. Layer L_{i+2} continues with white and so on.

For conductive paste, it is preferable to always have the extrusion at the end of a layer to minimize the time between extrusion and application of components and to reduce the risk of defects caused by a plastic extruder, crossing or touching a wire.

Extrusion width and speed Different aspects of an object (e.g. external perimeters or top solid infills) require individual extrusion parameters, mainly extrusion-width and speed. A `conductive_wire` extrusion role was added to assign an extruder and configure extrusion-width and speed values. This role is assigned to all polylines, each represented by an `ExtrusionPath` object. The extrusion speed for needle dispensing of conductive paste is very low, typically less than $2\,\mathrm{mm/s}$. The extrusion-width must be set by the user and describes the absolute width of the extrusion which is roughly shaped like a "squashed" cylinder.

Retraction and wiping Proper retraction for both the plastic, as well as the conductive ink extruder is important to avoid oozing and over- / underextrusion at the start of the first line. Oozing is a severe problem for the conductive ink extruder, as it potentially causes shorts. For the plastic extruder, blobs (too much) or gaps (not enough material) are the prevalent issue, but oozing can also cause problems if conductive traces are crossed and the uncured ink is smeared by the trailing plastic strand. Further details and images are given in sec. 7.1. Both extruder types have very different retraction and wiping requirements. The plastic extruder requires a high amount of fast retraction to remove the filament from the hot nozzle tip, whereas the conductive ink extruder is limited to very small retraction values to avoid intake of air into the syringe. Slic3r natively supports per-extruder retraction settings. However, each extruder has a different wiping position. Also, the current amount of retraction must be known for correct unretraction prior to wiping. To solve this, the tool change G-code insertion was extended by a set of new placeholder variables, which get replaced with the current values during each toolchange operation. Particularly `[previous_retraction]` and `[next_retraction]` are additionally exposed.

Different wiping positions were initially handled by a post-processing script, which filters G-code lines based on logical conditions. This initial work was later implemented in

Slic3r as a conditional G-code parser by the community. A correct unretraction movement for the plastic extruder (tool 0) can now be easily expressed as:

```
{if [next_extruder] == 0}G1 E-[next_retraction] F1400
```

Chapter 5

Object-Topology Aware Wire Routing

In the previous chapters, the technical foundations to 3D print electronics embedded into physical object were laid, covering all required steps for the full production pipeline. Once an object is designed, it can be exported, printed and electrically assembled in a fully automated process, without user intervention. However, arrangement and routing of electronics within a complex 3D-shape under the constraints of a delicate manufacturing process is an intricate task that requires some experience from the user. So far, the wires are only generated as a straight, linear interpolation between waypoints. In this chapter, an algorithm for local auto-routing is laid out. This is a first approach to support the designer by defining only the positions of the electric components and some waypoints to set the approximate layout.

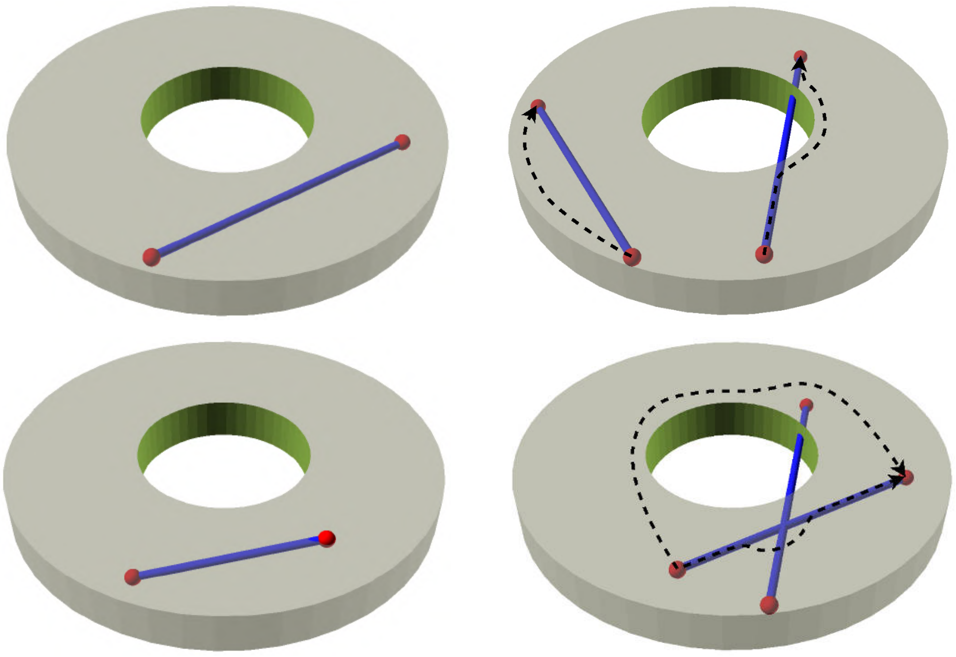

Figure 5.1 – Typical routing scenarios for a single wire, possible solutions are indicated with dotted lines. **TL**: Trivial case where the wire crosses only infill. **TR**: Touching a concave (left) or convex (right) perimeter. **BL**: Connection of different layers. **BR**: Intersection with other wire, collision could be avoided by detouring on the same layer or routing around the other wire on a different layer.

The term *local* in this context refers to finding a connection between two adjacent waypoints with fixed positions, where the wire segment must terminate at the exact waypoint positions. *Global routing* is defined as finding a connection between two endpoints of a net, e.g. two SMD-pins. In a weaker definition, waypoints can be set to guide the routing algorithm by attracting the search with preferred exploration along the predefined path.

For the rest of this chapter, the routing problem is defined as *finding the optimal, collision free path, connecting two points A and B which is printable for a given object geometry and set of printer configurations.* A and B are two adjacent *waypoints*, connected by a *rubberband*. The routing step is executed iteratively on all wire segments, avoiding collisions with previously routed wires.

The overall goal is to support users with their task of defining wire paths, by finding a smooth trajectory in a complex shaped object, while not interrupting perimeters and reducing the amount of small gaps. Avoiding collisions between wires is a second important objective. 3D printing offers a huge potential in this field, by introducing a full third dimension. On the downside, electrical connections between layers are prone to a high risk of defects. They also require significant physical space since direct vertical connections are not possible in most cases, and the routing complexity increases.

The routing algorithm should also adapt to changes in process parameters (layer height, number of perimeters, extrusion width etc.) to make the design process more independent from the manufacturing step. Figure 5.1 illustrates different typical scenarios in the same order as in this chapter. Figure 5.2 shows an actual screenshot of a trivial case of routing a single rubberband in the simple demonstration object from fig. 5.1. The waypoints are implicitly defined by the positions of the SMD-components, the wire is not yet generated. This object is used throughout the next sections as a minimal example to illustrate the basic concepts.

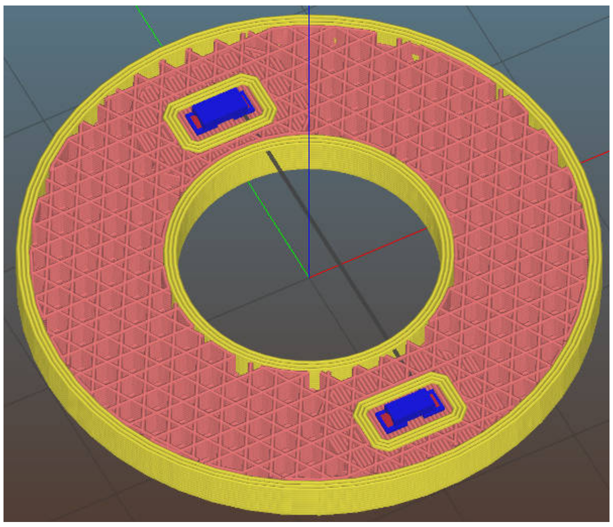
Figure 5.2 – Minimal example of a single wire to illustrate routing steps in the following sections.

The remainder of this chapter is organized as follows: first, an overview of search space representation and routing algorithms from related domains, particularly electronic circuits and robotic navigation, is given in section 5.1.

In section 5.2, the reduced problem of routing a single wire on a single layer is analyzed. This includes appropriate representation of the search space and utilization of common pathfinding algorithms.

Section 5.3 extends the search space to the full stack of layers which is required to describe a whole 3D-object. A focus is set on the problem of finding a set of suitable connections between adjacent layers which can then be used by the pathfinding algorithm to “jump” from layer to

layer. Another important aspect is the coherent representation of positions (polygon points, vertices and waypoints) to identify matching points on different layers and to use indexing for efficient data access.
Basic strategies for collision avoidance of multiple wires are discussed in section 5.4. Finally, section 5.5 wraps up the algorithmic results and gives a short summary of the entire routing and G-code generation process.

5.1 Related Approaches

Routing or pathfinding problems are a very common aspect in several domains and have received a tremendous amount of research over the last decades. The domain of PCB-routing, where many collision-free paths must be found in a constrained space, and the field of route planning in robot navigation and path planning, where only a single route must be found in a complexly shaped terrain, are particularly related to the problem at hand and therefore considered important.

5.1.1 VLSI and PCB routing

Very Large Scale Integration (VLSI) in general and PCB design in particular are concerned with the problem of arranging a number of components on a given surface (*placement*) and optimizing collision-free connections between the components (*routing*). Figure 5.3 illustrates how the problem is usually subdivided into multiple steps: *global routing* in which the wire segments are tentatively assigned to coarse regions and *detailed routing* where wire segments are assigned to specific routing tracks [A39]. Additionally, optional *timing driven* steps can be applied to refine the topology to perform optimizations, e.g., minimizing the total routing length or circuit delay. The additional steps are particularly interesting as a potential solution to compensate for the high resistivity of the silver ink used in our experiments.

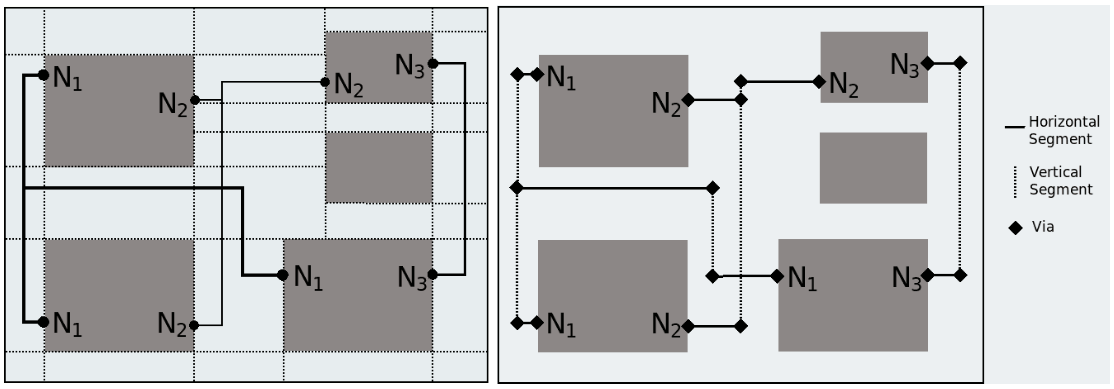

Figure 5.3 – Example of coarse *global* routing (**left**), where the wires are assigned to regions and fine *detailed* routing (**right**) to determine the final positions of wires and vias. The three nets N_1 - N_3 are routed with rectilinear paths on two separate layers for vertical and horizontal connections [A39].

To model the available routing space, occupied regions are represented as polygons and the free space is divided into regions of different types, e.g. *channels*, with wire running only from one edge to the opposite, and *switchboxes*, with connections into all four directions [A67, A39]. The routing space is typically stored in a graph data structure for efficient reasoning as sketched in fig. 5.4.

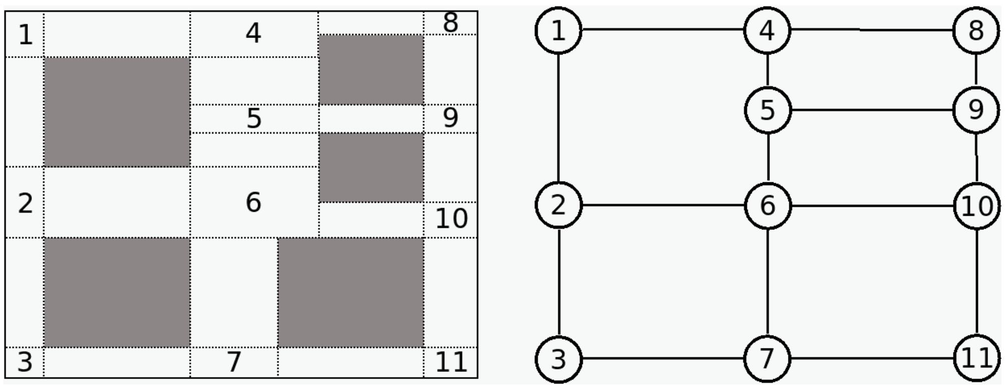

Figure 5.4 – Positions of switchboxes (numbered), channels (un-numbered) and the corresponding switchbox connectivity graph representation [A39].

Classic routing approaches are Manhattan-grid-based [A53] and typically utilize Rectilinear Steiner Minimal Tree (RSMT) algorithms to find an (optimal) spanning-tree between all pin locations of a net. Constructing an RSMT in the general case is proven to be NP-hard, therefore several heuristic solutions have been developed for practical applications [A31, A14]. Non-Manhattan Routing extends the grid to a 6- or 8-connected neighborhood, additionally allowing for diagonal connections [A98]. Several modern routing algorithms are based on graph routing, Integer Linear Programming (ILP) and congestion avoidance methods. The focus lies on the dispatching of a high number of connections, which currently is not a realistic scenario for printed electronics.
An important concept to resolve conflicting routes with intersections is the Rip-Up and Reroute (RRR) strategy [A39]. In the naive, greedy procedure, wires are routed sequentially, forcing later wires to accept large detours if the direct connection is already occupied. RRR allows to temporarily create conflicting routes. Once the overall structure is settled, those wires with the best alternative paths available are ripped up and routed again.

5.1.2 Path Planning in Robotics

This paragraph mostly follows the textbooks by Siegwart et al. [A75] and Tzafestas [A86].
Path planning in robotics refers to the fundamental problem of finding a collision-free path for a given robot configuration in a partly occupied environment. Given a configuration q of the robot that is composed of $q_1, \dots q_k$ values. Each value represents a degree of freedom of the robot (e.g. a joint). The configuration space CS of the robot is the set of values that its configuration q may take. Then, the free configuration space CS_{free} is the subset of CS where the robot is not in collision with an obstacle and therefore can move safely.
Path planning in the sense of navigation in a planar environment for mobile robots can be seen as a simplified sub-problem, where the degree of the configuration space is typically limited to two (x, y) or three dimensions (x, y, θ) for the position and rotation of the robot. For navigation purposes, CS_{free} is usually represented by a map. The type of map representation can

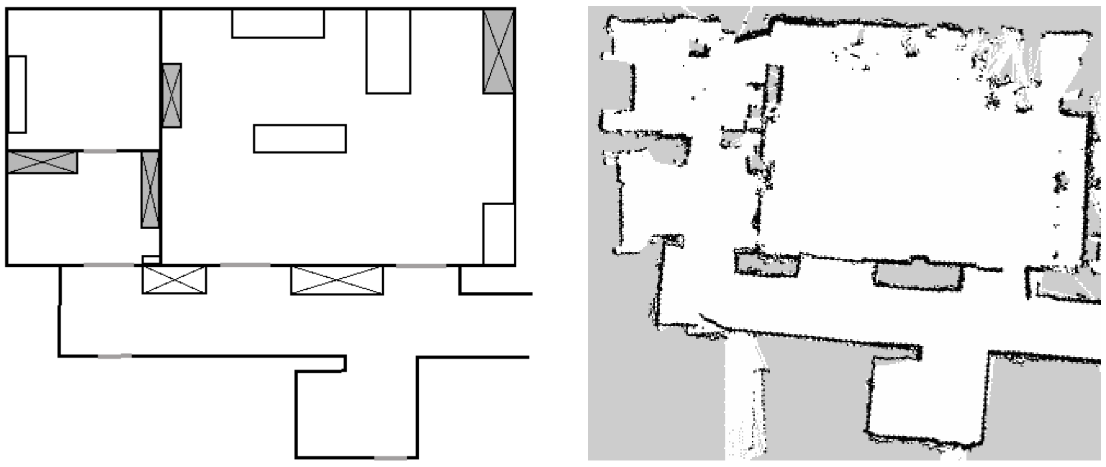
Figure 5.5 – **Left**: continuous map representation using polygons to model areas and obstacles. **Right**: the same map in discrete occupancy grid representation, recorded with a laser scanner.

have an impact on the available options for position representation and navigation algorithms. Figure 5.5 shows frequent representations of maps, either continuous, with polygons as environmental obstacles, or discrete occupancy maps, where the space is decomposed into a grid. Besides the fixed grid decomposition, *exact cell decomposition* is widely recognized, to tessellate the free space between obstacles into distinct regions [A51]. Exact decomposition is only feasible if the number of obstacles and the resolution of the polygon representation is low enough.

For mobile robots, path planning involves two aspects that complement each other. *Global* path planning identifies a collision-free, efficient trajectory from start to goal, based purely on prior knowledge of the terrain (map). *Local* obstacle avoidance approximately follows the global path, but modulates the trajectory based on current sensor information to avoid collisions with previously unknown or dynamic obstacles. For this study, we focus on global path planning under a closed world assumption without sensor input.

Deterministic search algorithms require an appropriate data structure to represent the map. As a common first simplification step, the robot is represented as a point and all obstacles are inflated by the radius of the robot convex hull. The map is then usually converted into a graph representation. Grid-based occupancy maps can be seen as a special case of graph representation where each cell is connected to the four or eight adjacent cells. Polygon base maps are often converted into a graph representation by constructing the *visibility graph*. All polygon points which are visible to each other are directly connected by a straight line as illustrated in fig. 5.6. Depending on the number of polygons and their resolution, the number of additional edges might become very large. The shortest path in a visibility graph often exactly follows the contours of some obstacles. While this effect is a serious problem in robotics, where a certain safety distance is desired, it well matches the requirement in 3D printing where a conductive trace is preferred to either match the contour or keep a certain distance to avoid small gaps. In a tessellated map representation from a cell decomposition, the center of each cell, or the center of each edge between two adjacent cells might be taken as a graph node, with edges connecting adjacent, non-occupied cells.

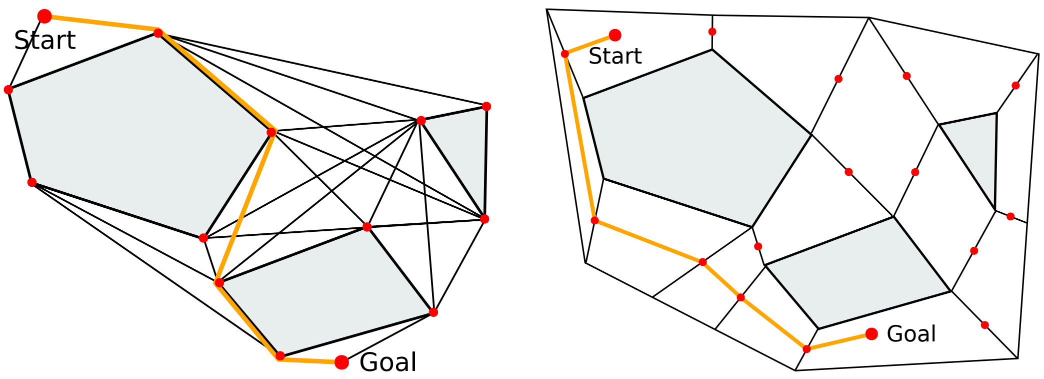

Figure 5.6 – Navigation in a polygon-based map representation. **Left**: visibility graph, constructed by connecting all pairs of polygon points (red) with unobstructed line of sight and result from the A* search (orange). **Right**: tessellated representation of the same map. The graph is constructed by creating nodes at the center of each edge (red) and connecting adjacent nodes.

5.2 Intra-Layer Connections

We start to solve the routing problem by considering the sub-problem of routing a single wire segment within a single layer L. Later we will later generalize the solution to the three-dimensional case in sec. 5.3.

5.2.1 Data Representation

This section gives a short overview of the basic data structures which are used throughout the rest of this chapter. The fundamental concepts of graph representation, notation and algorithms are covered in more detail by virtually any textbook on algorithms, e.g. [A15, A75]. An excellent, very detailed, informal overview of map representations and different aspects of the A* search algorithm is provided by [B23].

The search space in a given Layer L_i is constrained by the physical outline of the layer contour, represented by a set of nested polygons. It is also constrained by the contour of one or more previous layers $L_{i-1} \dots L_{i-n}$ since the wire must be printed on a solid surface; bridges or overhangs are not acceptable. The printed contour of Layer L_i is generated by a set of n_p perimeter loops, forming the solid shell of each object. Within this shell which is filled with a sparse infill structure, wires can be routed arbitrarily.

We use an *undirected*, *weighted* graph $G = (V, E)$ with $E \subseteq [V]^2$ to represent the search space of each Layer L_i. Vertices are mapped to a set of vertex properties: $V \to S$, particularly containing the spatial position p of each vertex: $p : V \to \mathbb{Z}^3$ and a number of properties for internal use in algorithms i.e. *color*, *distance*, *predecessor* etc. A weight function $w : E \to \mathbb{R}_0^+$ assigns a nonnegative weight $w(u, v)$ to each edge. The weights are used to “prioritize” connections, e.g. to attract routes to be aligned with perimeters.
All *coordinates*, *weights* and *distances* are scaled by a factor of 10^6 and represented by integer values to avoid accuracy problems caused by floating point approximations.

After initialization, the empty Graph G is successively filled with information which is already available prior to the routing step. This includes the existing perimeters of the given layer (sec. 5.2.2) and the direct connection between start- and endpoint of the current wire segment (sec. 5.2.3). During the routing process, the graph is successively extended as new connections are inserted in the currently explored region, aligned with a global grid (sec. 5.2.4).

The graph data structure is supported by external indices to allow for efficient access to individual elements. The spatial position p of each vertex is a native property of G (*vertex-point-index*). An inverse index $\mathbb{Z}^3 \rightarrow V$ is maintained as additional hash-map, to find the corresponding vertex for a given point (*point-vertex-index*). A list of all possible z-positions (layers) is provided to facilitate direct access to corresponding points on adjacent layers and to enable iterating over all layers of the 3D-model.

Finally, an R-tree [A30] based index is incorporated for efficient spatial relation queries (*spatial-index*). Since approximate spatial access is typically used in the current, or the direct lower and upper adjacent layers, the index is implemented as a map of two-dimensional R-trees, with z-positions as keys. The R-tree index is mainly used for two purposes. Due to the use of scaled integer values, coordinates are unique within the graph. However, coordinates from the user interface (*waypoints*) or slight deviations introduced during the slicing and polygon offsetting steps frequently result in very similar, but not identical points. Two points with a distance below a certain threshold ε are considered to be coincident. Without a spatial index, for simple lookup operations (*"is there a corresponding point on the next layer?"*; see section 5.3.2) all vertices of G must be checked for ε-coincidence individually by iterating the entire graph. A `nearest`-query is used to find the closest point which is then tested for ε-coincidence in a second step. The second application is introduced in sec. 5.2.4. The graph is dynamically extended by the search algorithm during the routing step. To connect a new grid-cell with existing vertices, all points within a bounding box must be identified (`within`- query).

No index	R-tree (quadratic)	R-tree (R*)	No wires
35.4 s	1.4 s	1.4 s	0.1 s

Table 5.1 – Execution time of the full slicing process for a test object with 604 facets to compare the effect of different indexing strategies. Wires were spanning the maximum possible extent of the object to achieve a worst case scenario. Different R-tree implementation strategies showed no significant effect. The test object was also sliced without embedded wires for reference.

Using the R-tree index approximately reduces the complexity for spatial queries from $O(n)$ to $O(\log n)$, which is significant, given that it is invoked in each exploration step of the search algorithm (Alg. 1, line 12). A brief performance evaluation is given in tab. 5.1.

5.2.2 Perimeters

The optimal route of a wire crossing or touching a perimeter would be such that it is perfectly aligned with the most inward perimeter extrusion line. If this is not possible, due to a lack of space, the next best option would be the second, third, etc. perimeter. The number n_p and width

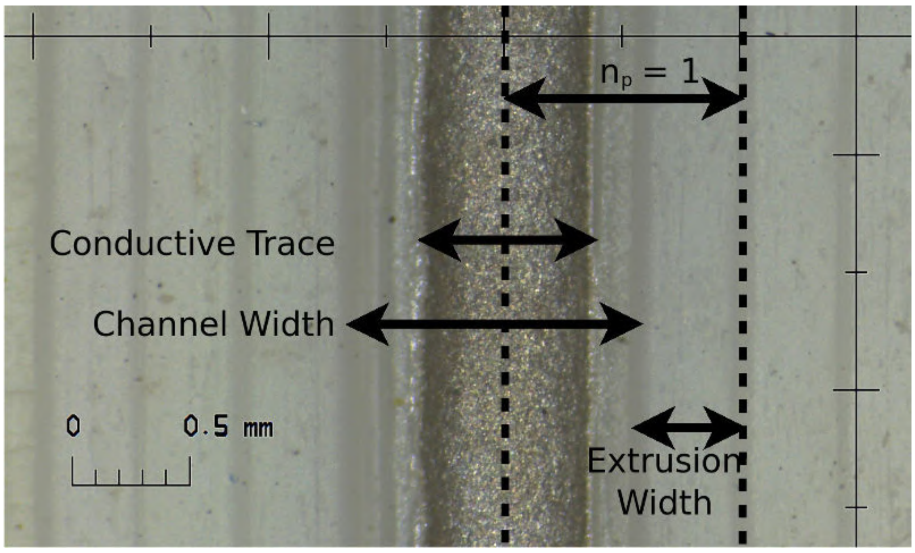

Figure 5.7 – Parameters of a single conductive trace embedded in a printed channel. The distance between the vertical dashed lines indicates the required offset Δ_1 to compute the deflated surface for a single perimeter loop (eq. 5.1).

δ_p of perimeter extrusions are defined by the user and potentially vary between each object, printer, or even different configurations on the same printer.
Figure 5.7 illustrates the dimensions of a conductive trace, the required channel and the combined distance from the boundary of a plastic extrusion to the center of the conductive trace as it is used to compute a wire trajectory aligned to the object boundary.
Optimal wire traces for all perimeters are found by taking the contour of Layer L_i (fig. 5.8 *Left*) and computing a set of offset-polygons (*deflated surfaces*) for each perimeter. The offset values Δ are given by:

$$\Delta_k = k \cdot \delta_p + \frac{\delta_c + \gamma}{2}, \quad k \in \{0 \mathinner{..} n_p\} \tag{5.1}$$

where δ_c is the extrusion width of the conductive material and γ is the amount of extra space to form a channel around the wire. The result of this operation is the center of the potential extrusion line for conductive material, aligned to the respective perimeter. As discussed in sec. 4.2.3 and illustrated in fig. 4.4, the extrusion width δ_p of the plastic extruder varies between internal and external perimeters and for different materials in one object and must therefore be computed for each individual layer and region.

In a final step, the resulting polygons are weighted, to prefer inner traces, and added to the graph. The result is depicted in fig. 5.8 right. The edge weight w for the k-th contour computes as

$$w_k = 1.0 + (n_p - k) \cdot \alpha \tag{5.2}$$

where α can be configured in the user interface as `conductive_wire_routing_perimeter_factor`, with a default value of $\alpha = 0.1$. For the example given in fig. 5.8, this assigns a weight of 1.0 to the most inward (3), 1.1 to the second (2) and 1.2 to the outer (1) contour.

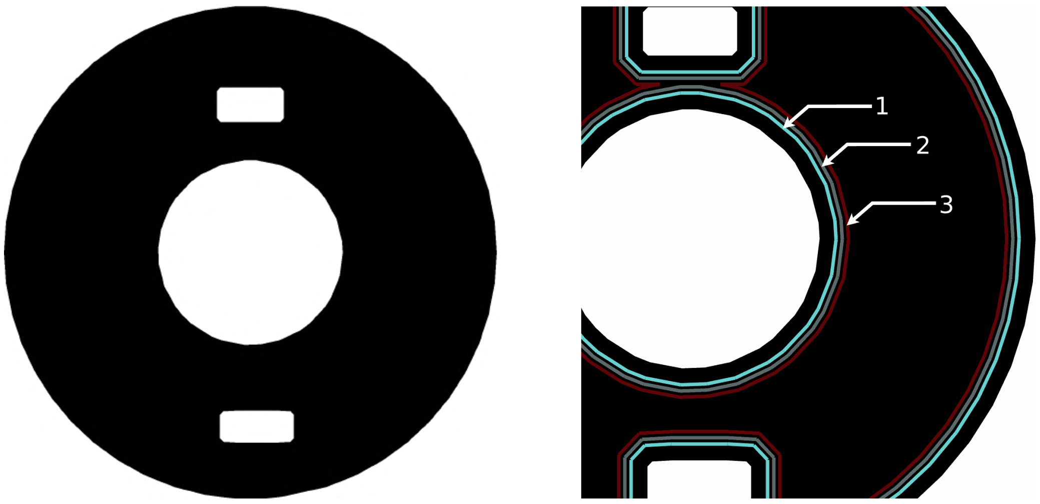

Figure 5.8 – **Left:** contour (slice) of layer L_i. **Right:** graph edges as potential routes for wires, aligned to the object perimeter, found by offsetting the contour polygon. The resulting edges are weighted decreasingly from 1 to 3 to prefer traces with a higher distance to the surface and then added to G.

Aligning conductive wires with the perimeter extrusions has an undesirable effect when the number of perimeter extrusions n_p is odd. In fig. 5.9 the conductive trace is correctly aligned at a distance of three perimeters, but since perimeter extrusions surround both the wire and the object, only an even number of loops is printable without a gap This effect can obviously be avoided by choosing an even number of perimeters.

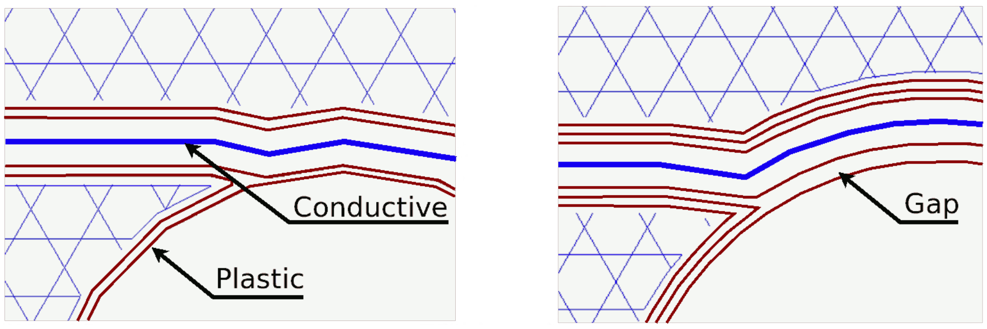

Figure 5.9 – Effect of wire aligned to an even number (**left**) and an odd number of perimeter extrusions, resulting in a gap (**right**).

5.2.3 Direct Connections

A second information which is immediately available is the direct connection l between A and B. Both points are always added as corresponding vertices s and t to G, as they are required as start- and endpoint of the search. In the trivial case where A and B both lie within the infill region of a single layer and a straight conductive line would not touch or cross any perimeters or other wires, an edge $e(s,t)$ is added as shortest possible connection.

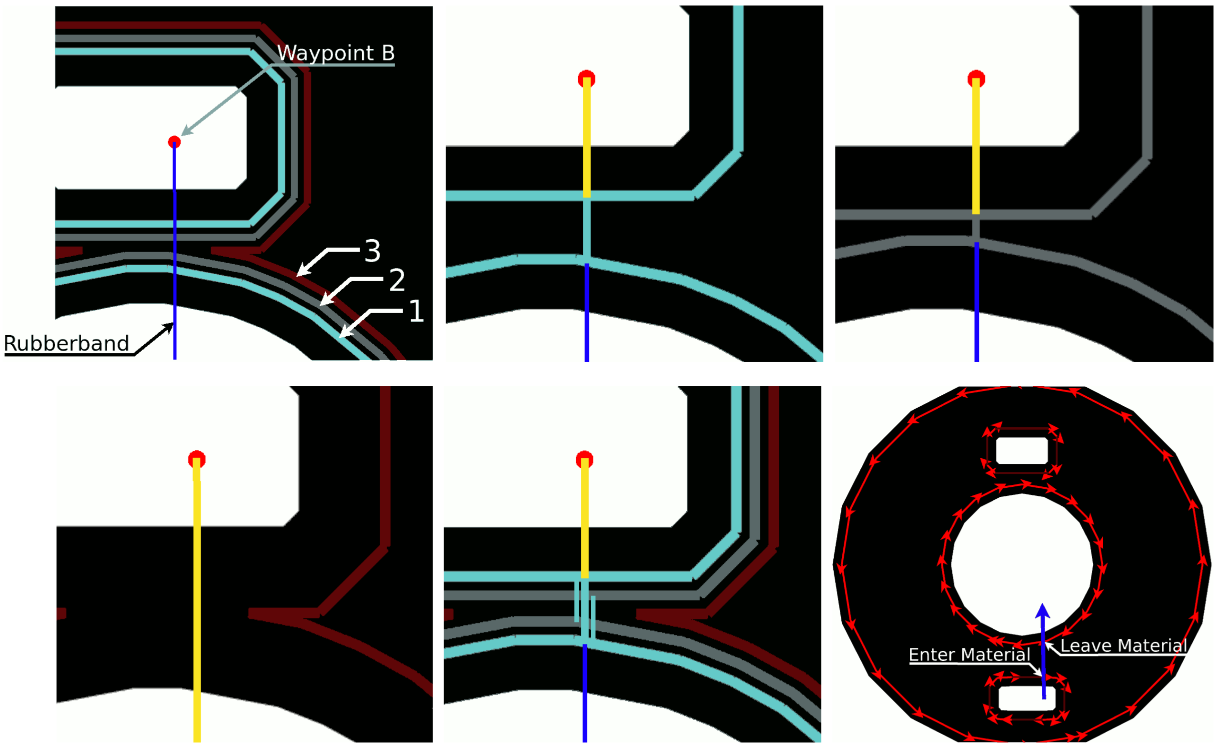

Figure 5.10 – Generation of *shortcut* edges if rubberbands are touching or crossing perimeter extrusions. **TL**: Rubberband potentially crossing all three designated perimeter-aligned wire extrusions with decreasing weight from 1 to 3. Intersection points with the first (**TC**), second (**TR**) and third (**BL**) extrusion path are computed individually and the resulting segments are appended to the graph. Weights are inherited from the perimeter polygons. A high weight (yellow) is assigned to edges outside of the material. **BC**: In a final step, all combinations of start- and endpoints of the resulting edges are appended to G as well to enable connections between the different path options.
BR: Orientation of contour polygons: outer perimeters (CCW) and inner perimeters (CW).

For the general case, intersections of the line l with all deflated surfaces generated in the last section are computed and fragments are added to the graph as *skip links* or *shortcuts* to accelerate the search and to provide direct connections between the perimeter traces of adjacent holes.

Consider the example given in Figure 5.10, where the direct connection l (blue) crosses the layer boundary twice. To find all shortcut connections, we iteratively compute the intersection of l with all deflated surfaces. For each intersection found, a new point is inserted into the polygon and added to the graph, along with a set of matching edges.

The shortcuts are weighted either with the weighting factor of the current inflated slice if the segment is inside of the material or with a (high) `hole_routing_factor` if not (yellow). The weight assignment is determined by computing the orientation of the current intersection with the deflated polygon as illustrated in fig. 5.10 *BR*. By definition, the outside of the object is always on the right side of a contour. Hence, the orientation of an intersection indicates whether the following section lies in a hole or outside of the object as depicted by the blue arrow.

The result without any further steps would be similar to the Bug2 algorithm described in [A58] (fig. 5.11 right).

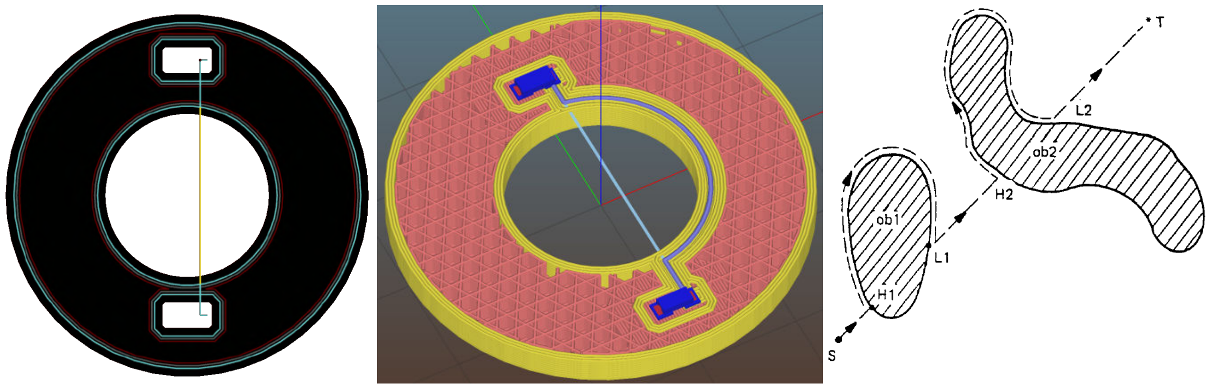

Figure 5.11 – Visualization of the routing graph with perimeter and direct connection edges (**left**). The route at this stage is bound to the static graph connections (**center**), resulting in trajectories similar to the Bug2 algorithm [A58] (**right**). (Image from [A58], fig. 4.)

5.2.4 Expanding Grid Search

Once the graph representation of Layer L_i is assembled, a variety of common search algorithms can be applied to find the most optimal route for a printed wire. We use a priority queue based implementation [B2] of the A* algorithm [A32] to conduct the search as outlined in Alg. 1.
The right-aligned comments serve two purposes: they informally describe the function of important steps and indicate visitor event points of the boost implementation, where the algorithm can be extended.
In the pseudocode, $d(v)$ is the distance of vertex v from the start vertex s. $f(v)$ denotes the estimated cost of the best path from s over v to the goal vertex t, by combining the distance to v and the estimated distance to the goal: $f(v) = d(v) + h(v)$. Q is a queue, holding all open vertices, ordered by their f-value. $p(v)$ points to the predecessor of v and represents the resulting path after execution of the search algorithm.

Two core concepts are highlighted in red: the *heuristic* h in line 1 and the *examine_vertex* visitor event point in line 12. The basic realization of both concepts is explained in the following. More details for the final implementation, covering the full 3D-space, are provided later in their respective sections 5.3.2 and 5.3.3.

```
A* (G, s, h)
    foreach vertex u in V do                              // initialize vertex $u$
        $d[u] := f[u] := \infty$;
        $color[u] :=$ WHITE;
        $p[u] := u$;
    end
    $color[s] :=$ GRAY ;                                 // initialize start-vertex $s$
    $d[s] := 0$;
    $f[s] :=$h($s$);
    Insert($Q$, $s$) ;                                    // discover vertex $s$
    while $Q \neq \emptyset$ do
        $u \leftarrow$ Extract-Min($Q$);                  // examine vertex $u$
        foreach vertex v in Adj[$u$] do                   // examine edge ($u, v$)
            if w($u, v$) $+ d[u] < d[v]$ then
                $d[v] :=$ w($u, v$) $+ d[u]$;
                $f[v] := d[v]+$ h($v$);
                $p[v] := u$;
                if $color[v] =$ WHITE then
                    $color[v] :=$ GRAY;
                    Insert($Q, v$);                       // discover vertex $v$
                end
                else if $color[v] =$ BLACK then
                    $color[v] :=$ GRAY;
                    Insert ($Q, v$);                      // reopen vertex $v$
                end
            end
        end
        color[u] := BLACK ;                               // finish vertex $u$
    end
end
```

Algorithm 1: The basic A* algorithm, used for searching an optimal wire route in G based on the formulation from the Boost Graph Library documentation [B2] which was used for the implementation.

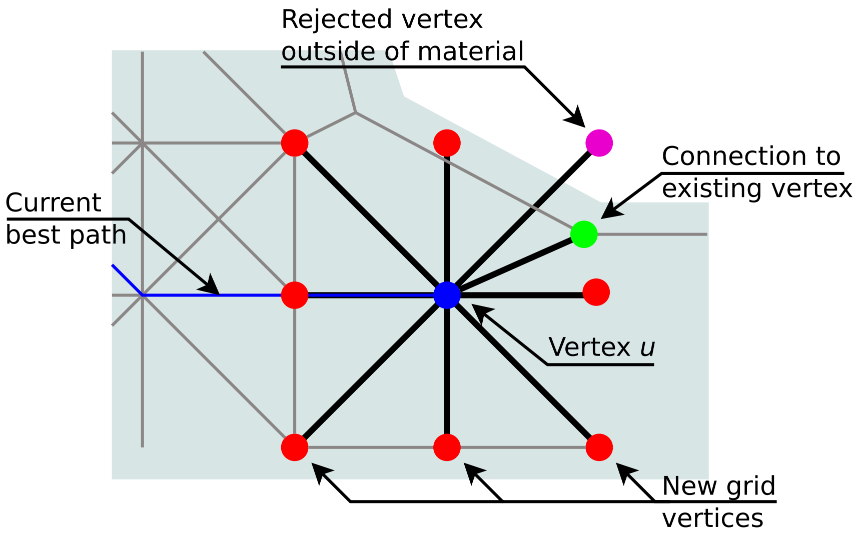

Figure 5.12 – Dynamic generation of new grid vertices. Upon examination of the current vertex (blue), new vertices (red) are generated in 45°steps with a distance of ν (`grid_step_distance`). Existing vertices within a radius of ν are connected in a second step (green).

So far, the search would be bound to the perimeters and straight connections, with trajectories "jumping" from obstacle to obstacle as illustrated in fig. 5.11. To also cover infill regions, an exploring grid is generated dynamically during the search. Upon examination of the current vertex u (Alg. 1, line 12), new vertices v_k are inserted in 45° steps around the current vertex during the examination step as illustrated in fig. 5.12. The 8 neighbor points are generated on a rectangular grid with configurable `grid_step_distance` ν, aligned to the object origin. In a subsequent step, it is tested whether the new vertices lie within an infill area by testing if they are contained by the deflated surface polygon of L_i (fig. 5.12, purple vertex). Valid new vertices are added to G and connected to u by an edge $e = \{u, v_k\}$. Additionally, existing vertices are connected by new edges if they lie within the grid step distance, to also establish contacts between perimeter traces and the grid (fig. 5.12, green vertex). Grid edges are weighted with the same factor as the most outside perimeter edges (cf. equation 5.2). With a number of n_p perimeters and the perimeter factor α, the grid weight w_g amounts to:

$$w_g = 1.0 + n_p \cdot \alpha \tag{5.3}$$

The R-tree index is utilized to efficiently select all existing vertices within a box of size ν (`grid_step_distance`).

Figure 5.13 demonstrates how the graph dynamically grows during the search. In the simple cylindric demonstration object, the resulting route is actually the same as the route shown in fig. 5.11 without grid generation. The two components are located very close to the inner perimeter, therefore following this perimeter is actually optimal. However, the difference is clearly visible in the second, slightly more complex object in fig. 5.11.

The key feature and main difference between A* and Dijkstra's algorithm is the use of a heuristic. Instead of only considering the minimum distance from the current node to the source, A* uses the sum of the distance from the source node s to the current node u and the estimated

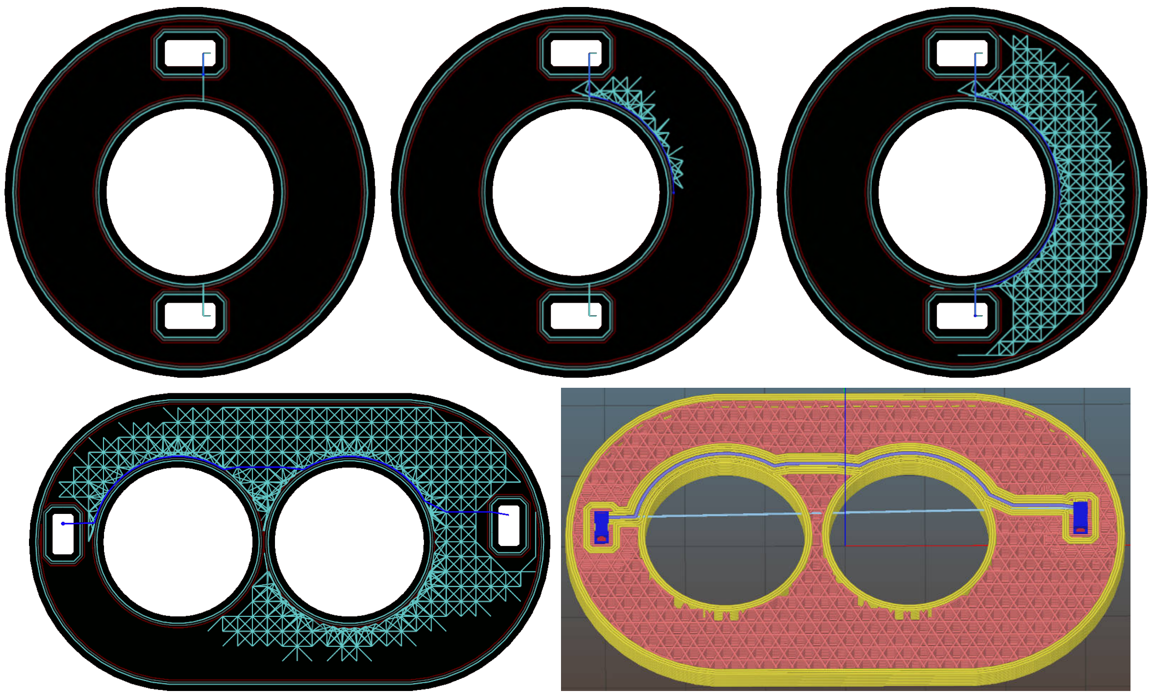

Figure 5.13 – **Top**: Development of the graph during a routing step. In infill areas, a grid is dynamically generated during the search process. **Bottom**: Demonstration of the same effect with an object where the wire actually crosses an infill region.

distance to the goal t to significantly accelerate the search by providing additional information about the general direction to the goal (alg. 1, line 16).
A heuristic is said to be *admissible* if it never overestimates the actual minimal cost between u and t. A* is optimal if the heuristic also is monotonic, meaning that for every pair of adjacent vertices x and y, h must satisfy the condition:

$$h(x) \leq d(x, y) + h(y)$$

However, even with a monotonic, admissible heuristic, all equally suitable paths with the same distance to the current fringe must be evaluated. The search can be accelerated by relaxing the admissibility criterion and slightly overestimating the actual distance. By adding a factor ε ($\varepsilon > 1$) to the heuristic, the search is performed faster, producing a non-optimal result. However, the result is still guaranteed to have a cost of at most ε times the optimal path [A63].

For the simplified 2D-routing problem, a Euclidean distance is used as heuristic to guide the search:

$$h(v) = \sqrt{{d_x}^2 + {d_y}^2} \cdot \varepsilon \tag{5.4}$$

where d_x is the distance between the current vertex and the goal vertex along the x-axis: $p(t).x - p(v).x$, d_y respectively. ε is a user-defined factor to adjust the processing speed versus routing quality. Due to the nature of the 8-connected grid, the Euclidean distance is not optimal in regions where the wire crosses only infill, resulting in an underestimation of the actual cost and causing the algorithm to evaluate more nodes than necessary. An optimal heuristic for infill areas would be the *octile distance*:

$$h(v) = (d_x + d_y) + (\sqrt{2} - 2) \cdot \min(d_x, d_y)$$

However, the octile distance overestimates the remaining distance if it is possible to travel along an inner perimeter and therefore would break admissibility.
Further details on the heuristic used for the 3D-case, including inter-layer connections are provided in section 5.3.3.

5.3 Inter-Layer Connections

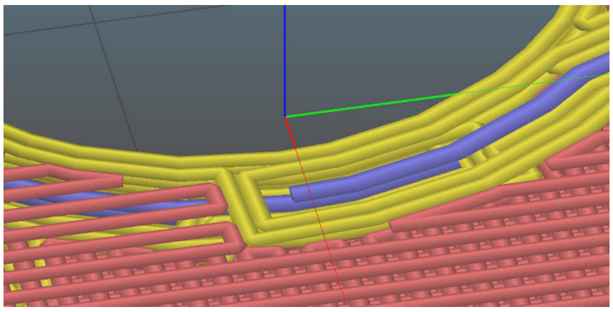
Figure 5.14 – Overlapping inter-layer connection, aligned with the object perimeter.

Generally, a wire is not horizontally aligned with a single layer, but crosses several layers. In the previous section, only those parts of each wire were used which intersect the current layer, as described in sec. 4.5.1 and [A92]. The start- and endpoint A and B of the current segment were both located on the same layer and the routing was also constrained to this layer.
For the A*-algorithm it makes no difference whether it operates on a 2D or 3D-graph to find optimal routes. The graph that was sketched in section 5.2 already contains the full 3D-representation of all layers. However, the challenge is to ensure proper overlapping of extrusions when the wire jumps to the next layer to ensure conductivity by creating a “staircase” while maintaining the alignment to perimeters as demonstrated in fig. 5.14. The required length of overlap when jumping from one layer to the next is given by a user-defined parameter `interlayer_overlap`. This problem can be solved by finding equal sequences of vertices pairwise in adjacent layers where the length of the sequence is higher than `interlayer_overlap`. Finding all possible combinations of graph segments for two adjacent layers is computationally expensive and therefore considered to be not feasible.
To reduce the complexity, we try to only search for combinations with a high probability of being used by the final route trajectory. In a first step, direct connections between A and B along the rubberband are added to the graph prior to the routing step to ensure the shortest path is always available (sec. 5.3.1). Then, to find eligible positions for overlapping, yet optimal inter-layer connections, the exploring vertex examination step (alg. 1, line 12) is used again to only consider candidates with a high probability of being used (sec. 5.3.2).

5.3.1 Direct Linear Connections

In section 5.2.3, it is described how the shortest, direct connection is always inserted to the graph before the actual routing step is executed. Since computing all intersections with perimeter polygons is not directly applicable for the 3D-case, the approach is extended with inter-layer connections.

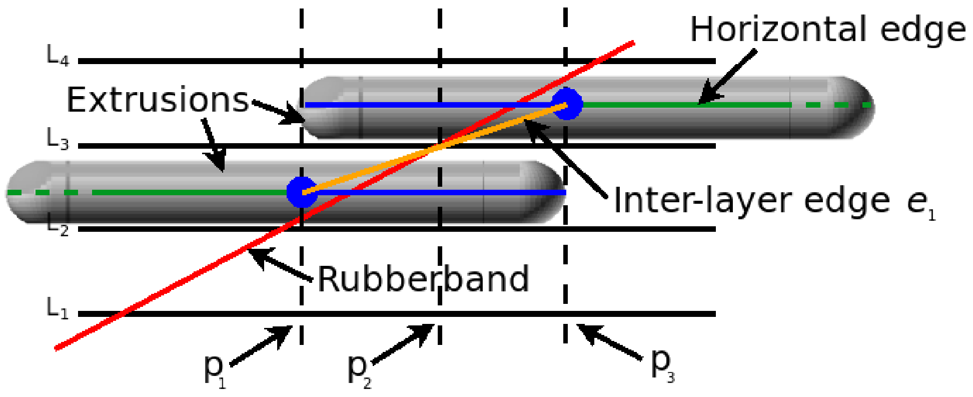

Figure 5.15 – Generation of overlapping sections for linear inter-layer connections. The rubberband (red) intersects the layer boundary of L_3 at p_2. Coming from the right, the upper horizontal edge (green) would end at p_2. It is extended to p_1 to achieve an overlap with the lower layer, but the new inter-layer connection edge is inserted starting at the point at p_3 (orange). The resulting route would traverse green, orange, green. The blue lines are additionally stored in an overlap-segments map and inserted later to achieve an overlapping electric connection. The resulting conductive traces are indicated in gray.

Each rubberband is split into a set of segments, one for each layer, as described in sec. 4.5.1 for static routing. Modeling overlapping sections in the graph is difficult. Simply connecting the endpoints of two segments on adjacent layers by a direct, vertical edge (at the p_2 line in fig. 5.15) would not create a stable electric connection, as the overlap is too short. To solve this issue, overlapping sections are modeled explicitly. The matching endpoints of two extrusions at the layer boundary are not extended as described for the static routing in sec. 4.5.1, but cropped by `interlayer_overlap`/2 as depicted in fig. 5.15. Both new endpoints (blue dots) are then inserted to G as new vertices u and v and connected by a direct edge $e = \{u, v\}$ (orange) which closes the gap and provides a connection between the layers. The new edge is horizontally aligned with the rubberband, but jumps to the next layer before the end of the current segment is reached, leaving a short "dead end" (fig. 5.15, blue line) in the routing graph. However, this is actually printed in the resulting G-code as overlapping connection. The weight of the new edge e is set to the weight of one original segment (fig. 5.15, blue), plus an additional static factor Γ. The effective cost of switching to the next layer is therefore equal to the actual horizontal distance. The double extrusion is not included, but the layer change is penalized by the static cost factor which typically is higher than the horizontal distance and implicitly controls how strongly layer changes should be avoided.

Figure 5.16 illustrates how all overlapping sections are stored in an external key-value data structure `overlap-map`. Each interlayer-edge is mapped by its vertex-ID to a sequence of 2D-points, representing the overlapping portion of two extrusions at the layer boundary, omitting the z-information. For the example in fig. 5.15, a direct line between the cropped endpoints is stored (edge e_1). After the routing step, each edge with $a.z \neq b.z$ is replaced by the corresponding sequence of points from the `overlap-map`. The sequence is inserted twice, with different z-values for both affected layers, such that the end of an extrusion is repeated on the next layer to close the electric connection.

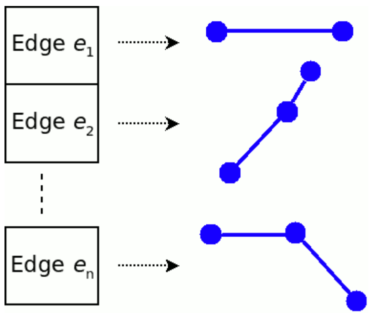

Figure 5.16 – The overlap-segments map is a key-value store, mapping vertex-IDs from inter-layer edges in the graph to actual point sequences of the original path which are later inserted into the G-code to generate overlapping extrusions.

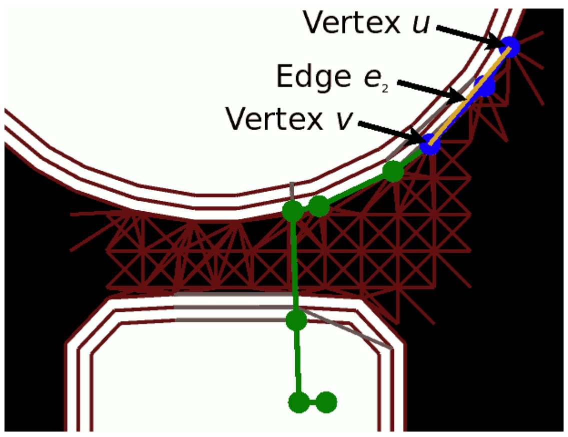

Figure 5.17 – Dynamic generation of inter-layer connections. The current optimal route (green) is traversed back during the vertex examination step. For all blue points on this path, a matching vertex was found on the adjacent layer, the blue segment is therefore stored in the overlap-segments map and a direct edge e (orange) is inserted to establish a connection between both layers.

5.3.2 Dynamically Exploring Connections

To efficiently find inter-layer connections in arbitrary regions, the exploring vertex examination step (alg. 1, line 12) is exploited again. During the A* search, the current front vertex u is tested for its suitability as an inter-layer connection point. Figure 5.17 shows how the current best path to u is traversed back, until the distance is higher than `interlayer_overlap` + `grid_step_distance`. This threshold was chosen to ensure that at least one single grid step is a valid candidate, even if the `interlayer_overlap` value ist very small. If every point on this path has a matching point on an adjacent layer, an inter-layer edge is added between the first matching point on the path v and the point corresponding to u in the previous (u_p) or next (u_n) layer respectively. The resulting edges e_p, e_n (e_2 in fig. 5.15 and fig. 5.17) are aligned with the current best path and open routes with the same horizontal distance but terminating on a different layer. Both edges are also appended to the `overlap-map` introduced in the previous section. The weight $w(v, u_n)$ of e_n is set to the sum of the weights of all edges from u to v plus a constant factor $\mathit{\Gamma}$:

$$w(v, u_n) = \sum_{k=u}^{v} w(k, p(k)) + \mathit{\Gamma}$$

where $p(k)$ denotes the predecessor of k. $\mathit{\Gamma}$ is exposed to the user interface as a parameter to control how much layer changes should be avoided. The factor directly determines how far the algorithm explores horizontally around an obstacle before it considers searching at the next layers. Inter-layer connections tend to be less reliable than extrusions on one layer and require additional toolchanges. Depending on the geometry of the individual object and the machine characteristics, layer changes can be either favored or avoided.
While the basic idea is straightforward, a number of important details must be taken into consideration for practical applications. In most cases, u is a front vertex, and in infill regions the grid vertices at adjacent layers are not yet generated. A set of 9 new vertices is therefore created for both adjacent layers as described in sec. 5.2.4, including the points u_p (previous) and u_n (next) at the same horizontal position as u. After the validation check, u_p and u_n are also connected to their surrounding valid vertices.

Grid vertices are well aligned and a mapping between vertices at the same horizontal position on adjacent layers can be done in constant time via the *point-vertex-index* by replacing the z component of the point $p(u) = (x, y, z)$, since they are generated in scaled coordinates and numerically stable. The *spatial-index* is used to map vertices derived from perimeter polygons or rubberband intersections which are subject to slights offsets and floating point deviations.

The newly generated edge $e_2(v, u_p)$ is not directly connected to front vertex u and will therefore not be evaluated during the current examination step in alg. 1, line 13. Vertex v is already on the closed list (marked as *black*) and will also not be evaluated again, leaving e_2 as a dead branch in the original formulation of A*. To enforce a re-evaluation, v is inserted into the queue Q again, by repeating the steps from line 16 and 18 to 25 without updating the predecessor map p, re-inserting or pushing v to the correct queue position. In the next iteration, v is examined again with u_p and u_n being in the adjacency list, correctly appending them to the fringe if their relaxation is successful.

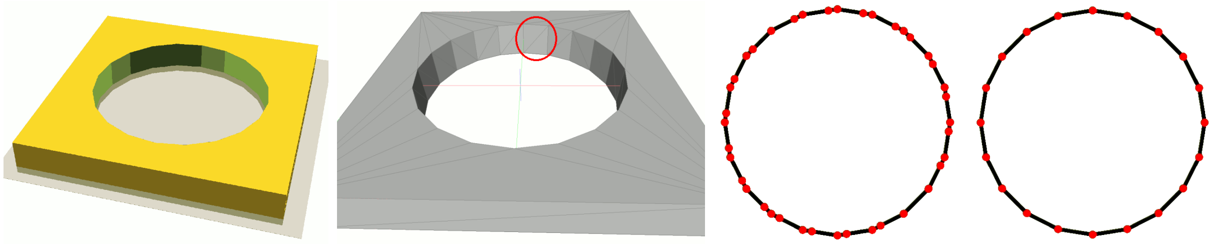
Figure 5.18 – Removing redundant collinear points. From left to right: **1**: Typical object with many rectangular surfaces, sectional plane indicated in gray. **2**: Tesselated representation, all surfaces are composed of 2 or more triangles. **3**: Resulting polygon in the slicing process on the indicated layer, containing a number of collinear points from the additional triangle edges (red marker in 2). **4**: Same polygon after collinear points were removed.

The triangle-based representation of 3D-models introduces another type of ambiguity. Figure 5.18 shows a typical example, where the rectangular surfaces of the cylindric cutout are represented by two triangles. The resulting contour polygon of a single layer contains a number of redundant, collinear points, which are on a different, slightly shifted position for each layer, as the triangle edges are intersected at different heights (red marker). An otherwise matching segment for an inter-layer connection would be interrupted by a misaligned redundant point. To avoid this, collinear points are removed immediately after the tessellated model is sliced into contour polygons with the algorithm depicted in alg. 2. For each consecutive set of 3 points p_1, p_2, p_3, the distance between the mid point p_2 and the line $[p_1, p_3]$ is computed. If the distance is below a threshold ε, p_2 is skipped and p_1 is tested against the next pair of points.

```
input  : A polygon $P$ and tolerance $\varepsilon$
output: Simplified Polygon $P$
$pp[1 .. \texttt{Size}(P)] := P.points$;
$pp[\texttt{Size}(P) + 2] := P.points.first$;       // Append first and last
$pp[0] := P.points.last$;                            // point to cover boundaries
Clear($P$);
while $i <$ ( Size($pp$) $- 2$) do
    $k := i + 1$;
    while $k <$ ( Size($pp$) $- 1$) do
        $l :=$ Line($pp[i]$, $pp[k+1]$);
        if Distance($l$, $pp[k]$) $< \varepsilon$ then
            $k$++;
        else
            if $i > 0$ then                          // implicitly removes
                Append($P$, $pp[i]$);                // duplicated first point
            end
            $i := k$;
            break;
        end
    end
    if $k >$ (Size($pp$) $+ 2$) then
        break;                   // Remaining points must be collinear
    end
end
Append($P$, $pp[i]$);
```

Algorithm 2: Remove all collinear, redundant points from a polygon.

As a side effect, removing collinear points often significantly improves the general performance of the entire slicing process as all subsequent operations must respect the redundant information. The implementation was therefore merged into the general version of Slic3r[1].

Contrary to the problem of redundant collinear points, a low density of points on the perimeter polygons also poses an issue. The distance between each two adjacent points p_i and p_{i+1} must

[1]Issue and related code are documented at https://github.com/slic3r/Slic3r/issues/4726

be smaller than `interlayer_overlap`, otherwise the search for an inter-layer connection would be aborted as the overlapping segment becomes too long. This is particularly relevant for technical objects with long, straight surfaces as demonstrated in fig. 5.19.
Two strategies were considered to solve this issue:

- Insertion of additional (redundant) points into the contour polygons to achieve sufficient density, resulting in a graph where the length of each edge is guaranteed to be below `interlayer_overlap` length.
- Dynamic generation of new vertices during back traversal of the current best path.

Since the second option raises a number of subsequent problems with the implementation of the search algorithm (particularly the predecessor map would be invalidated), the first approach was implemented.

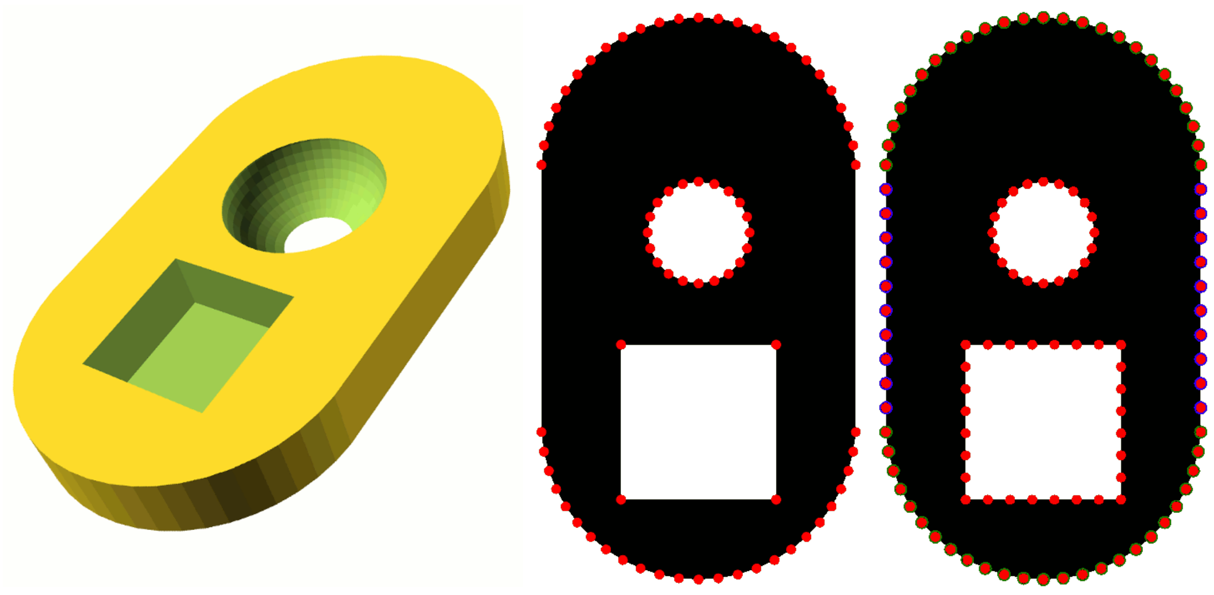

Figure 5.19 – Alignment and upsampling of contour polygon points to guarantee maximum edge length constraint for inter-layer connections. The contour of a single layer (**center**) is compared pointwise against all points of the previous layer. **Right**: matching points with slight deviations are aligned (green), points matching the contour are inserted (blue). In a final step, additional points are inserted where the distance between two points is higher than `interlayer_overlap` (at the rectangular cutout).

Additionally inserted polygon points should be aligned with corresponding points on adjacent layers. The upsampling steps are depicted in fig. 5.19. For a given Layer L_i all polygon points are compared to the points in L_{i-1}. In a first step, coincident points are aligned and points occurring in L_{i-1} but not in L_i are projected upwards (green and blue points in fig. 5.19). In a second step, all polygons are "upsampled" by inserting new points e.g. at the rectangular cutout in fig. 5.19 which did not exist in the previous layer. Typically, adjacent contours are very similar and the point density is sufficient after the projection step, such that the upsampling occurs only a few times for each object at strong contour changes.

The bowl-shaped cutout in fig. 5.19 is an example of an inclined surface where an overlapping inter-layer connection which follows the contour could still be printed with sufficient overlap. Given an extrusion width δ_c for a conductive trace, a layer height h and a surface inclination angle θ, the offset τ of two such traces amounts to:

$$\tau = \tan(\theta) \cdot h \tag{5.5}$$

Requiring a minimal overlap of $2/3 \cdot \delta_c$, inter-layer connections are printable at surfaces with a maximum inclination of:

$$\theta < \tan^{-1}(\frac{\delta_c}{3 \cdot h}) \tag{5.6}$$

With typical values of $\delta_c = 0.5\,\text{mm}$ and $h = 0.2\,\text{mm}$ inclinations up to $\sim 40°$ are printable ($0°$ is vertical).

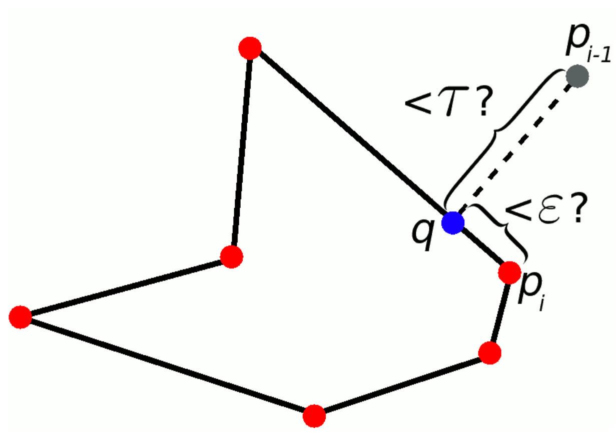

Figure 5.20 – A point p_{i-1} is projected onto the polygon as q. If $|q - p_i| < \varepsilon$, p_i is aligned to the projection p. Otherwise, if $|q - p_{i-1}| < \tau$, q is inserted as projected point into the Polygon.

Alignment and projection of points at inclined surfaces is achieved by projecting a point p_{i-1} from L_{i-1} to the current polygon P as depicted in fig. 5.20. If the projection q is within a distance of ε to an existing point p of P, the points are aligned by setting $P = q$. Otherwise, if the distance between p_{i-1} and q is below τ, a new point is inserted into P at the position of q. The algorithm is provided as pseudocode in alg. 3.

All the steps outlined in this section are executed per layer, bottom up, on each set of deflated surfaces, before the contours are converted into the graph representation.

Figure 5.21 shows a rendering of a tool path generated with the demonstration object from fig. 5.19. The wire is automatically routed through the object, crossing several layers, without any additional waypoints. The trace is aligned to both the inclined surface at the spherical cutout, where the overlapping segments slightly deviate from layer to layer to follow the changing contour, and to the featureless vertical surface of the cubic cutout.

```
// prev_p :  set of all points from previous layer $L_{i-1}$
// polygons :  all polygons in this layer $L_i$
// $\varepsilon$ :  equality threshold
// $\tau$ :  inclination threshold
foreach $p$ in prev_p do
    foreach $pg$ in polygons do
        $q$ := ProjectOnto($p$, $pg$);
        if Distance($p$, $q$) $< \tau$ then
            $n$ := Nearest($q$, $pg$);
            if Distance($n$, $q$) $< \varepsilon$ then
                $n := p$;
            else
                Insert($q$, $pg$);
            end
        end
    end
end
```

Algorithm 3: Projection of points from previous layer L_{i-1} and alignment of existing points in the current Layer L_i.

5.3.3 Heuristic Guidance

The direct Euclidean heuristic introduced in section 5.2.3, eq. 5.4 can easily be extended to three dimensions:

$$h(u) = \sqrt{{d_x}^2 + {d_y}^2 + {d_z}^2} \cdot \varepsilon \tag{5.7}$$

This heuristic is admissible, but often significantly underestimates the remaining z-distance due to the additional constant cost factor Γ which prevents the algorithm from generating unnecessary inter-layer connections (cf. sec. 5.3.2). If start and goal vertex are located on different layers, too many edges are evaluated. For a more accurate estimation of the z-distance, the number of layer changes must be counted (the layer thickness is not fixed and can vary through-

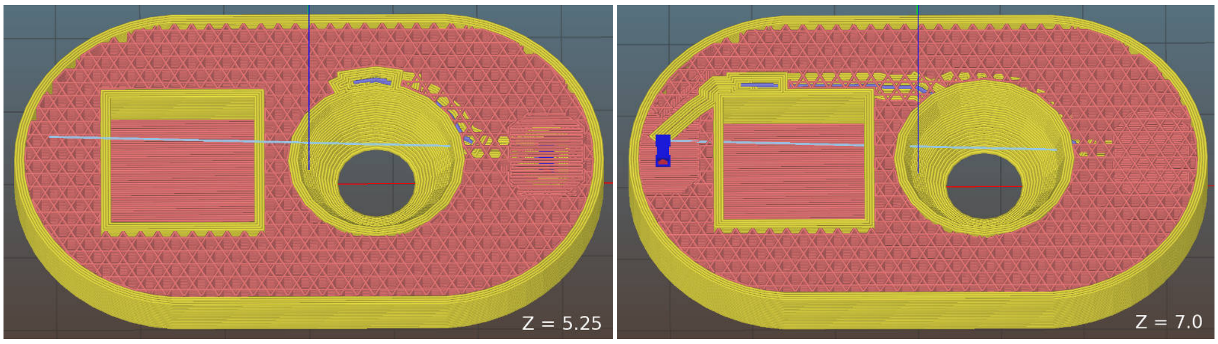

Figure 5.21 – Rendering of a tool path where the wire automatically follows the contour of both an increasingly inclined surface (bowl) and a long straight vertical surface (cube). Several layer changes occur along both structures. Note that the wire is intentionally covered with sparse infill only for transparency.

out the object). With $||d_z||$ denoting the number of layer hops, the actual distance is estimated as:

$$h(u) = \left(\sqrt{{d_x}^2 + {d_y}^2 + {d_z}^2} + ||d_z|| \cdot \mathit{\Gamma}\right) \cdot \varepsilon \tag{5.8}$$

It is generally preferable to equally distribute layer transitions along the trace and avoid local "stacks" of short extrusions. To support a uniform distribution, the heuristic is further extended with an adaptive factor:

$$z_\alpha = \left|\left(\frac{d_{xy}}{D_{xy}} - \frac{d_z}{D_z}\right) \cdot \nu\right| \tag{5.9}$$

D_{xy} is the horizontal Euclidean distance between start and goal vertex. $\frac{d_{xy}}{D_{xy}}$ therefore describes the remaining portion of the horizontal distance in the range $[0..1]$, accordingly for the vertical ratio. The difference of both ratios is exactly zero along the direct line between both vertices. In other words: the difference becomes a positive value if the z-distance is too small or too large in relation to the remaining xy-distance. The result is a dimensionless number and must be scaled to match the dimension of the grid. It is therefore multiplied with the `grid_step_distance` ν, so the additional estimated value does not exceed one grid step. The resulting heuristic is implemented for the A* algorithm as:

$$h(u) = \left(\sqrt{{d_x}^2 + {d_y}^2 + {d_z}^2} + ||d_z|| \cdot \mathit{\Gamma} + z_\alpha\right) \cdot \varepsilon \tag{5.10}$$

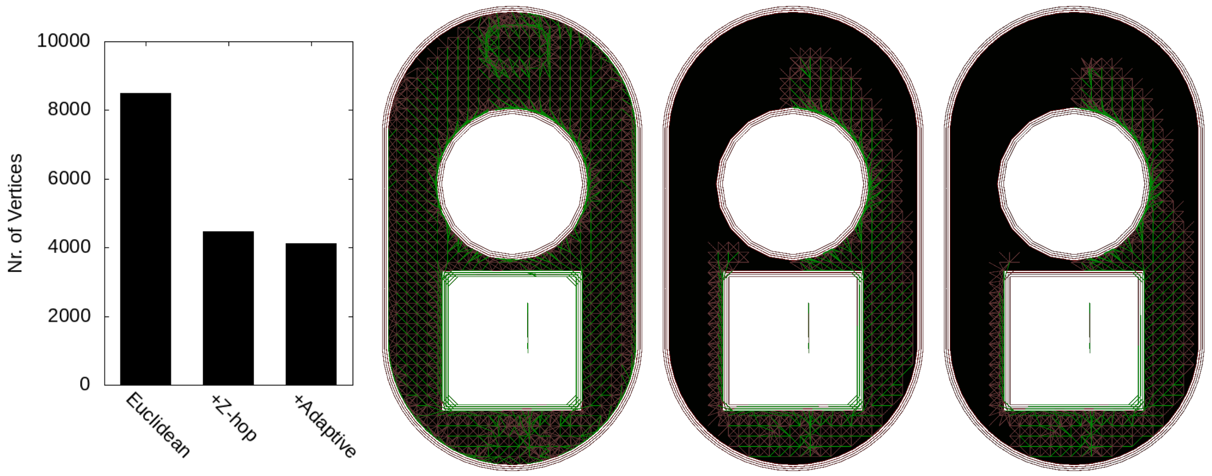

Figure 5.22 – Effect of improved heuristics on the evaluation complexity, measured by the amount of vertices generated during the search. **Left**: number of required vertices for routing the wire in the test object from fig. 5.21. **Right**: corresponding final graph at layer z = 6.5 mm with Euclidean, z-corrected and adaptive heuristic.

Figure 5.22 shows how a well-tuned heuristic reduces the processing complexity and run-time. Underestimating the remaining z-distance causes the search algorithm to increase the evaluation radius by $||d_z|| \cdot \mathit{\Gamma}\,\mathrm{mm}$, often resulting in fully covered layers as pictured in the first graph. The adaptive factor only has a small effect on the complexity by "pruning" some paths with similar cost but different inter-layer connection positions.

In cases where the inclination between A and B is too high to form a straight, step-wise connection, the routing algorithm is forced into a meandering trajectory to elongate the trace until it is long enough for the required number of layer transitions, as illustrated in fig. 5.23. To avoid sharp edges or even vertical stacks of extrusions, the heuristic is further extended to not only consider the current vertex u, but also the two predecessors $p(u)$ and $p(p(u))$ if they exist. The angle θ between these three points is computed as:

$$\theta = \arccos\left(\frac{\vec{AB} \cdot \vec{BC}}{||\vec{AB}|| \cdot ||\vec{BC}||}\right)$$

Acute angles are penalized by a higher estimated remaining distance. As the grid is arranged in 45°steps, the heuristic $h(u)$ is adjusted in 4 discrete steps:

$$h'(u) = \begin{cases} h(u) + 0 & \text{if } \theta \leq 1/4\pi & // \leq 45^\circ \\ h(u) + \nu \cdot \alpha_1 & \text{if } 1/4\pi < \theta \leq 1/2\pi & // > 45^\circ - < 90^\circ \\ h(u) + \nu \cdot \alpha_2 & \text{if } 1/2\pi < \theta \leq 3/4\pi & // \geq 90^\circ - < 135^\circ \\ h(u) + \nu \cdot \alpha_3 & \text{if } \theta \geq 3/4\pi & // \geq 135^\circ \end{cases}$$

The factor α can be used to progressively assign higher distances to sharper angles.
It was stated above that the Euclidean distance fulfills the admissibility criterion and therefore guarantees an optimal solution. This is also true for the corrected z-distance introduced with eq. 5.8, which only gives a better estimation of the previously underestimated z-distance. However, both the adaptive z factor (eq. 5.9) and the penalization for sharp angles can break admissibility in certain cases, namely if a very good, direct connection exists along a low-weighted perimeter. The adaptive z guidance can cause a maximum extension of one grid step length ν over the entire routed path, which is considered acceptable. Enforcing low angles might add a significant distance, but in this case a longer trajectory is explicitly preferred to improve the mechanical printability.

5.4 Wire Collisions

Avoiding wire crossings while minimizing the length of each wire is the main goal of traditional routing algorithms for electric circuits. In the routing approach presented in this thesis, basic collision avoidance is inherently achieved by processing one wire after the other. For each individual net, the routing graph is updated and only regions not yet occupied by previously routed wires are considered. The required information is collected upon construction of the

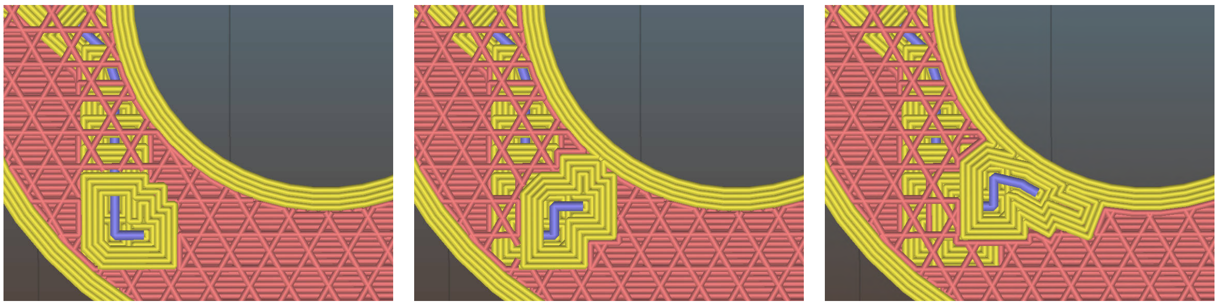

Figure 5.23 – Routing of a wire with high vertical distance between the waypoints. The horizontal distance is not sufficient for the required number of inter-layer overlaps, resulting in a non-direct route to increase the trace length.

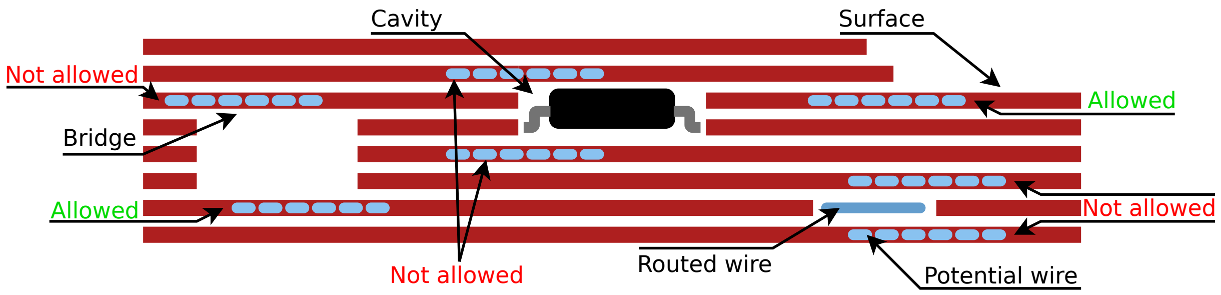

Figure 5.24 – Classification of regions at object surfaces, bridges, component cavities and already routed wires.

static routing graph in two steps, covering the previous and following few layers. Given a required shell thickness of k layers, the contour polygon of the current layer is modified by the following steps:

Previous layers must be included anyway, to avoid generation of non-supported wires e.g. when printing on bridges. This is achieved by computing the intersection of k layer contours below the current layer, which already contain the channels from previously routed wires.

Subsequent layers would also contain wire channels, but at this point it is not possible to distinguish a wire channel from a hole or a surface. Since printing on or close to surfaces is a frequent valid use case, channel polygons for routed wires on the next k layers are generated again by offsetting the trajectory (cf. sec. 4.5.2) and only those polygons are removed from the current layer's contour.

Figure 5.24 illustrates how the region above a routed wire can be classified equally to a region on top of a bridge; both are not supported by plastic. In contrast, the region below a routed wire must be removed from the graph to avoid electric shorts while routing at an internal or external surface is unproblematic. Cavities for electronic components are basically treated equally as wires, with only minor differences in the implementation.

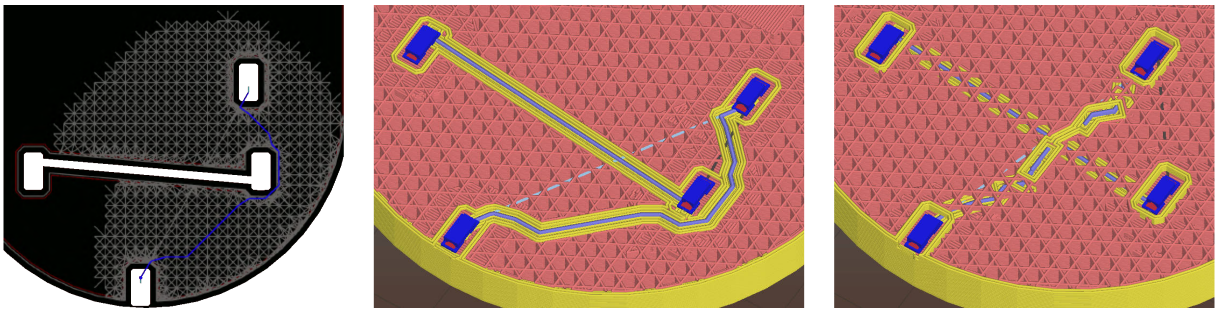

Figure 5.25 – Wire collision resolved by detouring on the same layer (**center**) and by switching to a higher layer (**right**). Note that the position of the upper right component is different in both cases, resulting in the respective shortest path.

Figure 5.25 shows the resulting graph of a layer with colliding wires. Depending on the wire geometry, the currently routed wire is detoured around an existing route or evades a collision by moving to a higher or lower layer. A main factor to control this behavior is the static inter-layer weight factor Γ. With a high value, long detours on the same layer are preferred.

While collisions are inherently avoided by routing wires sequentially, often the resulting length is not optimal. Figure 5.26 illustrates a case where the order of wire processing strongly influences the quality. To mitigate this effect, a heuristic is used to optimize the order of the rubberbands prior to the routing step.
The general approach is simple and common in literature:

1. For each net, count the number of collisions with other nets, assuming that all connections are realized as straight lines. Sort nets ascending by number of collisions.
2. In a second step, order nets with an equal number of collisions by their length, starting with the shortest.

The actual implementation of the net ordering heuristic raised practical challenges. First, the collision of the wires represented by a one-dimensional line is insufficient, as the extrusion and channel around the wire have a certain extent. This is solved by first inflating all other wires to the channel diameter and computing intersections with the inflated polygons. Inflating the wires is also important if a wire ends inside the perimeter of a second wire, which then has more intersections and will therefore circumvent the first. Second, if the nets comprise multiple layers, 3D-intersections must be computed to correctly identify collisions. This is solved by slicing the rubberbands according to the set of layers, inflating each individual segment and accumulating the intersections from all layers.
The aspect of collision avoidance for 3D-wires bears a huge potential for further optimization. Counting the intersection of unrouted wires obviously does not yield optimal results. It is expected that typical methods from VLSI and PCB design are applicable at this point, e.g. Rip-Up and Reroute (RRR), to cover situations where the object geometry prevents straight traces.

5.5 Algorithms Summarized

After going through the algorithmic details of all routing steps individually, this section gives a short summary of the contents of this chapter to provide a comprehensive overview. The handling of electronics is integrated into the overall slicing process mainly as two additional steps

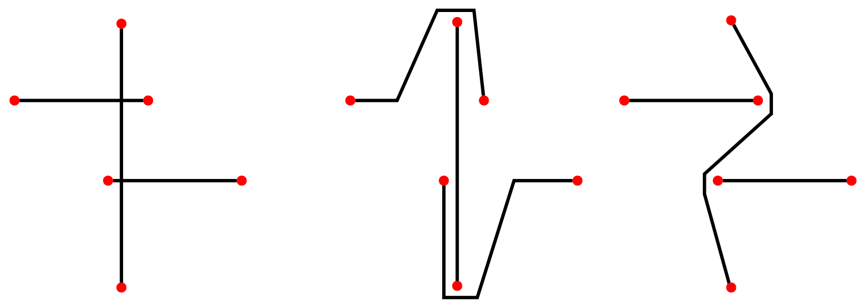

Figure 5.26 – Effect of net order in wire routing. Processing the vertical connection first results in long, detoured routes for the other wires (**center**). The accumulated length of all nets is optimal when processing the horizontal wires first (**right**).

to modify the layer surface polygons:

- Re-slicing is triggered by changing a net or moving a component.
- The first two steps of the conventional slicing process are executed: the position of all layers is determined and a vector of nested polygons (*LayerParts*) is computed, describing the outline of each layer (sec. 4.2.3).
- Component cavities are inserted by removing their hull polygons from affected layers.
- Wires are generated. The resulting channels are also removed from the layer polygons. Extrusion paths for the conductive material are computed, stored per layer and integrated into the G-code during export.
- The normal slicing process continues with perimeter and infill generation. The alignment of wires, beds and the generation of solid surfaces to support electronics in sparse infill areas is implicitly done, only based on the modified polygons.

This chapter covered the step of generating wire trajectories between fixed, given waypoints (item 4 in the list above). The most simple option is to insert direct channels from waypoint to waypoint, resulting in very predictable routing. However, this is often not optimal or requires setting a high number of waypoints. The technical details of implementing the required basic functions for this strategy were introduced in chapter 4. Building on this fundamental functionality, a first approach to auto-routing was implemented to achieve good solutions in complex object geometries with low manual effort.
While the individual steps were presented in the order they were technically implemented, introducing the basic concepts first and building up towards more general solutions (2D $\rightarrow$ 3D), the following pseudocode gives an informal overview over all steps in the order they are executed:

```
Route (Layers, Schematic)
    // Pre-process polygon based layer representations
    foreach Layer l in Layers do
        foreach Polygon p in l do                          // sec. 5.3.2
            RemoveCollinearPoints(p);
            AlignToLayer(p, $l_{-1}$);
            UpsamplePoints(p);
        end
    end

    // Prepare graph data structure, compute optimal routes
       along the perimeters
    $G :=$ new Graph;
    foreach Layer l in Layers do                           // sec. 5.2.2
        Insert($G$, DeflatePolygons($l$.polygons));
    end

    // Change execution order to minimize collisions
    foreach Net n in Schematic do                          // sec. 5.4
        // Number of intersections with other nets, if they
           were routed as straight connections
        CountIntersections(n, Schematic.nets);
    end
    Sort nets by number of collisions and length;

    // Execute actual routing step segment by segment
    foreach Net n in Schematic do
        foreach Segment s in n do
            Insert direct connection into $G$ ;            // sec. 5.2.3
            A*($G$, $s$) ;                                 // secs. 5.2.4, 5.3.2
            Remove resulting channels from contour polygons ;   // sec 4.5.2
            Reset $G$ to intital state, update affected layers by re-generating them from
              the modified contour polygons;
        end
    end

    // Generate extrusion commands
    foreach Layer l in Layers do                           // sec. 4.5.2
        Sort routed wire fragments;
        Apply overlaps;
    end
end
```

From line 2, the contour representations of all layers are re-structured, such that the points are well aligned over all layers and the distance between adjacent points is neither too low, which would generate unnecessary extra vertices, nor too high, which would prevent the algorithm from finding inter-layer connections. The pre-processed polygons are then converted into the graph representation by multiple offsetting. The resulting graph contains edges which are positions such that a wire trajectory would exactly follow the object contour along the perimeters. In the following step starting at line 15, the nets are pre-ordered to minimize wire collisions.

The actual routing step is executed for each wire segment individually. The segment is inserted into the graph as a direct connection (line 22). Then the A* algorithm is executed, dynamically growing a grid in infill regions of the object and gradually establishing inter-layer connections along the search direction, where a sufficient overlap is possible. Once a trajectory is found, it is stored as polyline-segments per layer and the resulting channels are cut from the contour polygons. The graph is reset to the contour representation from line 13, but all layers affected by the route of the current segment are updated to respect the new channels.

In a final step (line 29) all wire fragments are accumulated per layer and converted into volumetric extrusions for the G-code export.

Figure 5.27 shows an application of the algorithms introduced in this chapter. Three LED are integrated into the boat as navigation lights, connected to a microcontroller. A few waypoints where manually set at the bow of the boat to achieve a small distance to the components, and two waypoints at stern for the power connection. The routing algorithm then generated the trajectories. It kept the wires within the material at the walls and avoided collisions with other wires and components.

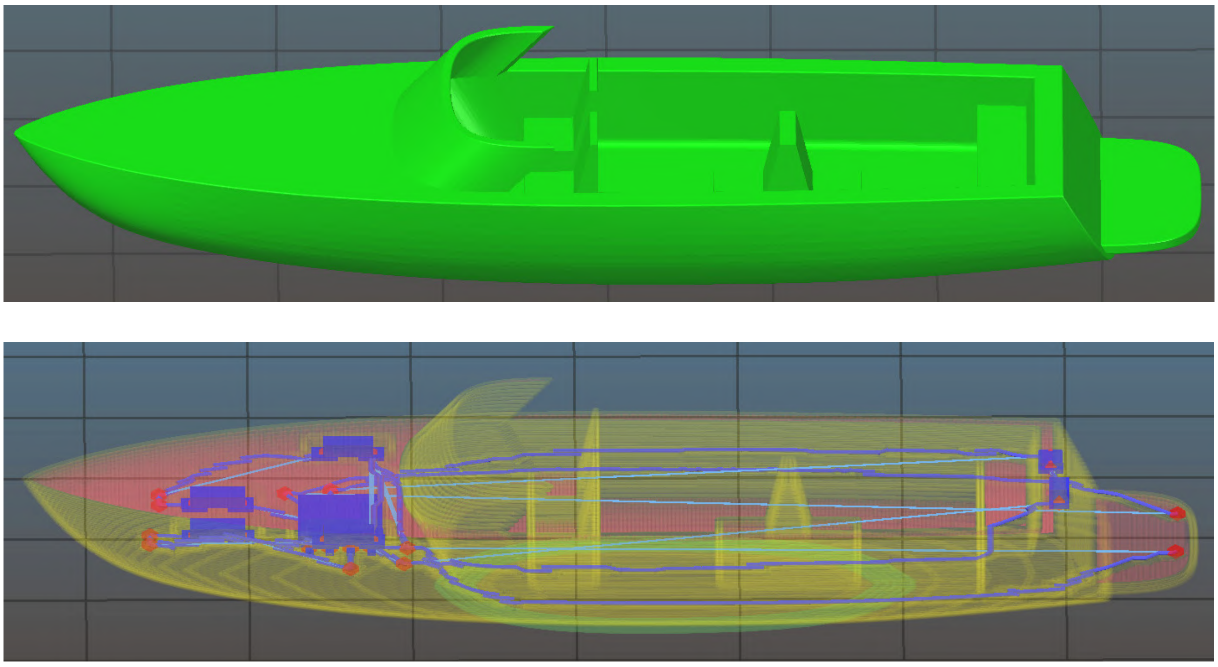

Figure 5.27 – Example 3D circuit generated with the autorouting algorithm. Model by Maxlarsen under CC BY 3.0 license.

Chapter 6

Process Documentation and Verification

Except for the camera-guided placing of electronics components described in sections 3.1.4 and 3.2 and thermal control, the entire build process runs in an open loop control. This is common for most additive processes, but an increasing demand for quality assurance, documentation and verification of the build process is conveyed from the industry to enable integration into production processes. This is particularly important for the integration of electronic circuits which are composed of complex but very small SMD components, requiring thorough monitoring and verification in the production process even for comparably reliable traditional 2D PCBs. The additive process introduces a number of additional uncertainties, primarily related to the inhomogeneous results of material deposition of both structural and conductive material.

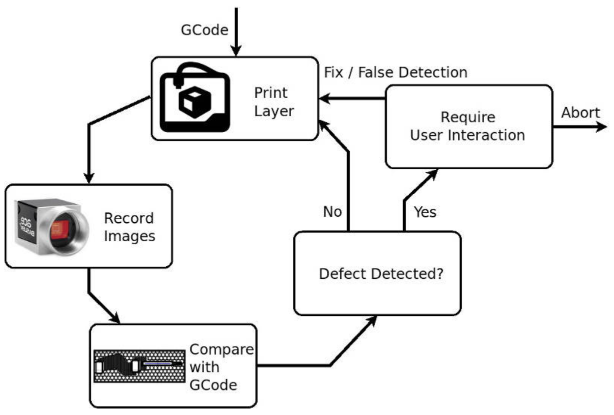

Figure 6.1 – General workflow for the verification approach. Once a layer has been completed, a set of images is recorded and stitched together, classified into categories (electronics, ink, plastics) and compared with the expected geometries from the G-code file to detect possible defects.

The final step of this work therefore aims to partially close the control-loop by automatically incorporating feedback during the print [A93]. To achieve this, the head camera, originally intended to guide the picking of components, is also used to take images of the workpiece during the print. The general idea is sketched in fig. 6.1. When a layer is completed, the camera is used to take a set of images of the surface. The tiles are stitched into one large image which already serves as a layer-wise documentation of the print process. The image is then compared with the G-code, ink and plastic regions are identified and the printjob is paused if a possible defect was found. A human operator is then asked to fix the issue and continue or abort the job.

The documentation and verification software is implemented as an OctoPrint plug-in [B37] and can be configured for every OctoPrint-controlled printer with a suitable camera. It relies on the OctoPNP camera control interface for encapsulated hardware access. Technical documentation of the plug-in is provided in the repository.

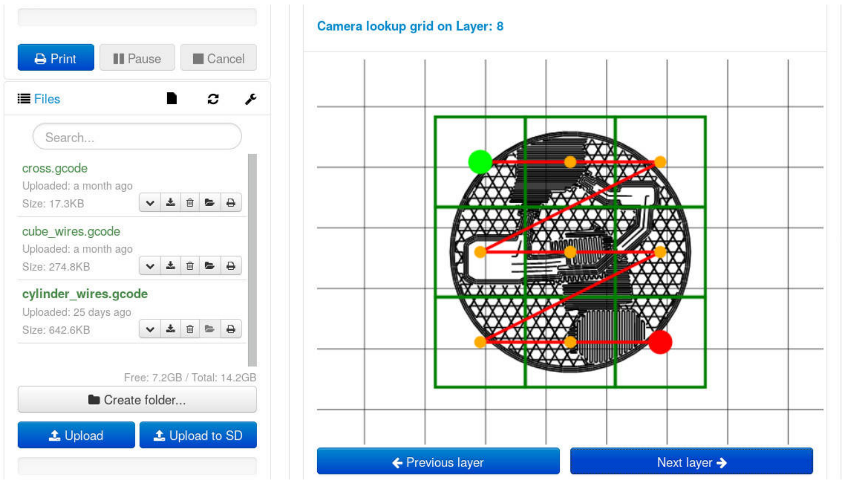

Figure 6.2 – Screenshot of the OctoCameraDocumentation software.

6.1 Image Recording during the Print-process

To obtain images with sufficient resolution and low distortion, only a small area can be covered by a single image recorded with the camera. Except for very small objects, documenting an entire layer requires taking several images which are stitched together as a first processing step. To cover only regions where material was deposited in the current layer, the tool analyzes the G-code and generates a grid with optimal coverage for each individual layer as illustrated in fig. 6.2.

A resulting set of tiles for one layer is given in fig. 6.3. Unfortunately, simple stitching of the tiles into one image proved to be inadequate for our belt-driven gantry systems. A resulting set of tiles for one layer is given in fig. 6.3. Unfortunately, simple stitching of the tiles into one image proved to be inadequate for the belt-driven gantry system. In many cases, backlash effects and insufficient positioning precision caused significant offsets. To reduce stitching inaccuracies, tiles are recorded with a certain overlap and correlation-based image alignment is applied on the overlapping regions [A21]. New tiles are appended iteratively from bottom to top, left to right. For each new tile, the offset and correlation coefficient with the bottom and left tile are computed if they exist. The new position is the average of both offsets, weighted with the correlation coefficient to prefer corrections with higher confidence.

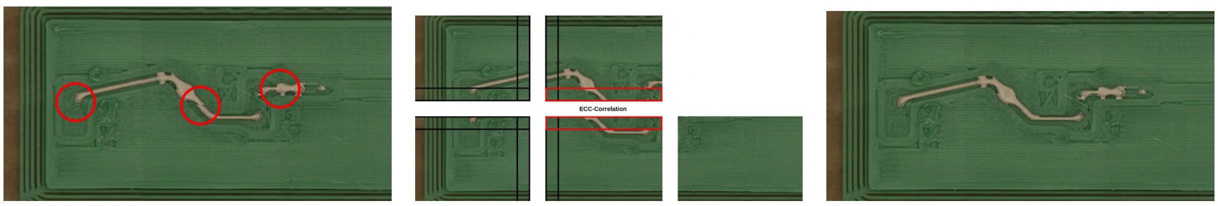

Figure 6.3 – Stitching of tiles into a composed layer image. **Left**: individual images as recorded are naively assembled with positioning inaccuracies highlighted in red. **Middle**: positions of tiles recorded with extended borders are corrected by pairwise correlation of overlapping regions **Right**: high-quality stitched layer image.

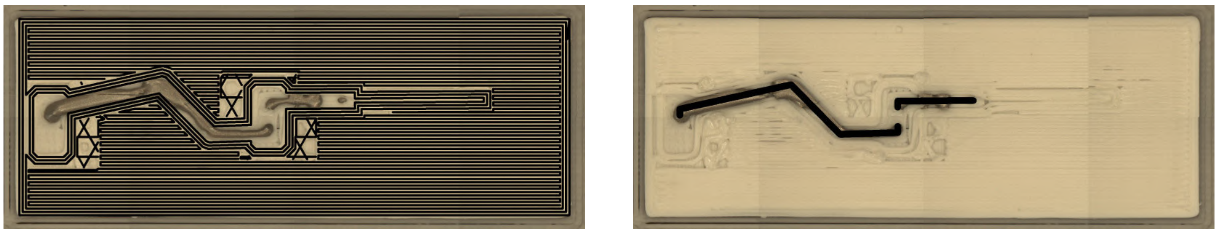

Figure 6.4 – Overlay of the raw image and G-code of a single layer. **Left**: all extrusions executed by the plastic extruder `T0` and **right**: conductive ink lines extruded by `T1`.

6.2 Feature Segmentation

A reliable and accurate segmentation of regions covered with conductive ink is essential to automatically detect wire defects. Since the desired geometry of both materials is encoded in the G-code, a mask can be created by parsing all positioning commands for a particular extruder which contain a positive amount of extrusion. The mask is converted to the known image coordinate system and applied as shown in fig. 6.4. This step also masks regions from previous layers, e.g. in sparse infill areas which are visible in the image.

Figure 6.5 left illustrates how the predetermined positions of all plastic pixels (top) and conductive ink pixels (bottom) are identified in the image by inverting the previously generated masks. Since each image typically contains several thousand pixels in each dimension, only a random subsample is extracted for each extruder to reduce the amount of data. Figure 6.6 clearly indicates that even a simple linear separation is sufficient to classify pixels based on their color values. The resulting dataset contains an equal number of labeled data points from both classes.

In a subsequent step, a Support Vector Machine (SVM) is trained with the labeled dataset and used to classify pixels in the image into the categories *plastic* or *ink* (fig. 6.5 right). For filament colors with a low distance to the ink color, a significant number of pixels is misclassified with this method (fig. 6.5, top right result). This is mainly caused by incorrect labels in the training data. The ink extrusion frequently shows slight over- or underextrusion and deviates from the intended path due to surface tension dragging the ink to the channel boundary. Most masked areas, therefore, contain a certain amount of pixels from the opposite class. To mitigate this

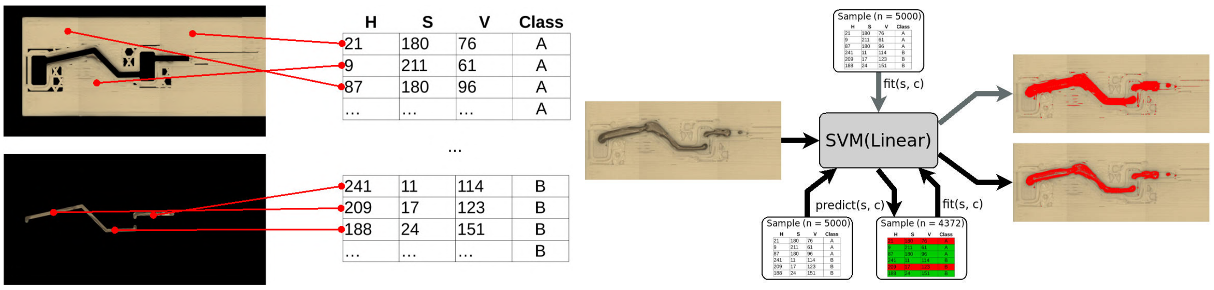

H	S	V	Class
21	180	76	A
9	211	61	A
87	180	96	A
…	…	…	A
…			
241	11	114	B
209	17	123	B
188	24	151	B
…	…	…	B

Figure 6.5 – SVM-based classification into plastic / conductive material. **Left**: a random subsample of plastic- and ink-pixels is extracted from the image after masking the respective tool paths. **Right**: an SVM is trained with the labeled dataset and used to classify all pixels in the image (top). The classification accuracy is significantly improved by self-filtering the training data. Entries which do not match the prediction of the SVM are removed and the classifier is re-trained with the reduced dataset (bottom).

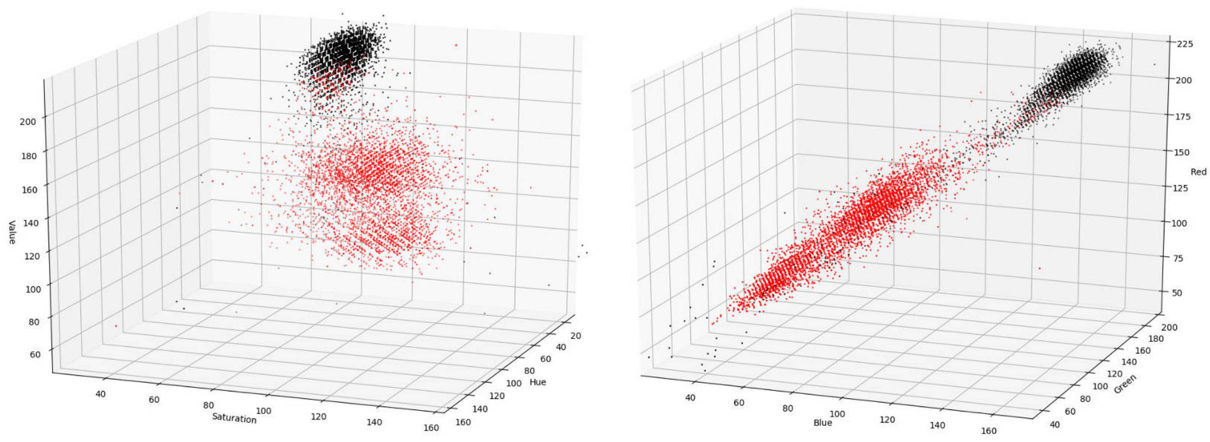

Figure 6.6 – Distribution of pixels in HSV (**left**) and BGR (**right**) color space. Black data points represent pixels from regions masked as plastic based on the G-code information, red data points were masked as conductive ink. Note that some pixels are misclassified due to over / unterextrusion of conductive material.

effect, the SVM is used to self-filter the training data. The classification is predicted for all elements of the training dataset, entries for which label and SVM prediction do not match are removed. The SVM is then re-trained on the filtered dataset, yielding a clearly improved classification result (fig. 6.5, right bottom).
To verify the classification step, a set of otherwise identical test objects with different plastic filament colors was printed (fig. 6.7). All colors with sufficient distance to gray showed satisfying results. For very similar colors (gray), reliable recognition becomes increasingly hard, even for humans.

6.3 Defect Detection

In a final analysis step, interruptions and strong deviations of the extrusion traces are automatically detected before printing the next layer. The test is implemented as a positive-coverage, sliding window detector as illustrated in fig. 6.8. A circular template matching the extrusion diameter d_e is moved along the intended ink-extrusion lines extracted from the G-code. The template is shifted by $d_e/2$ for each iteration step. If the ratio of pixels classified as ink vs.

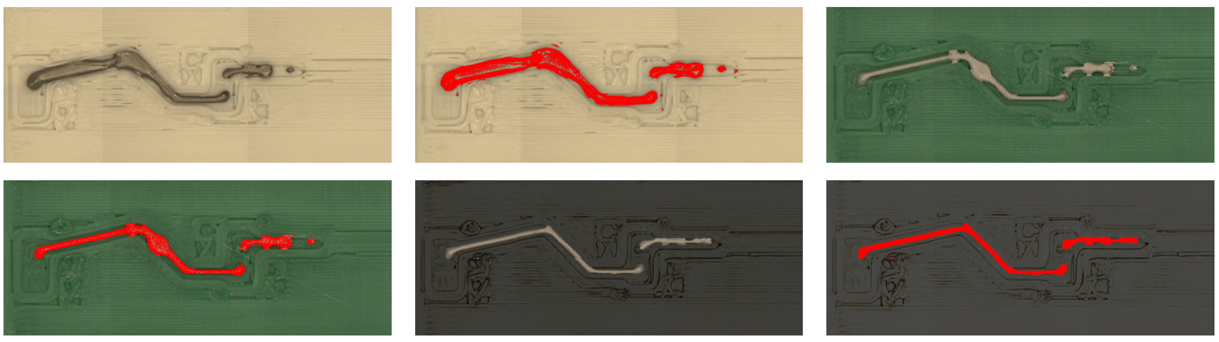

Figure 6.7 – Successful verification of the ink segmentation algorithm with different filament colors.

plastic falls below a threshold ε, the region covered by this template is flagged as *defect* (red markers in fig. 6.8 and 6.9).

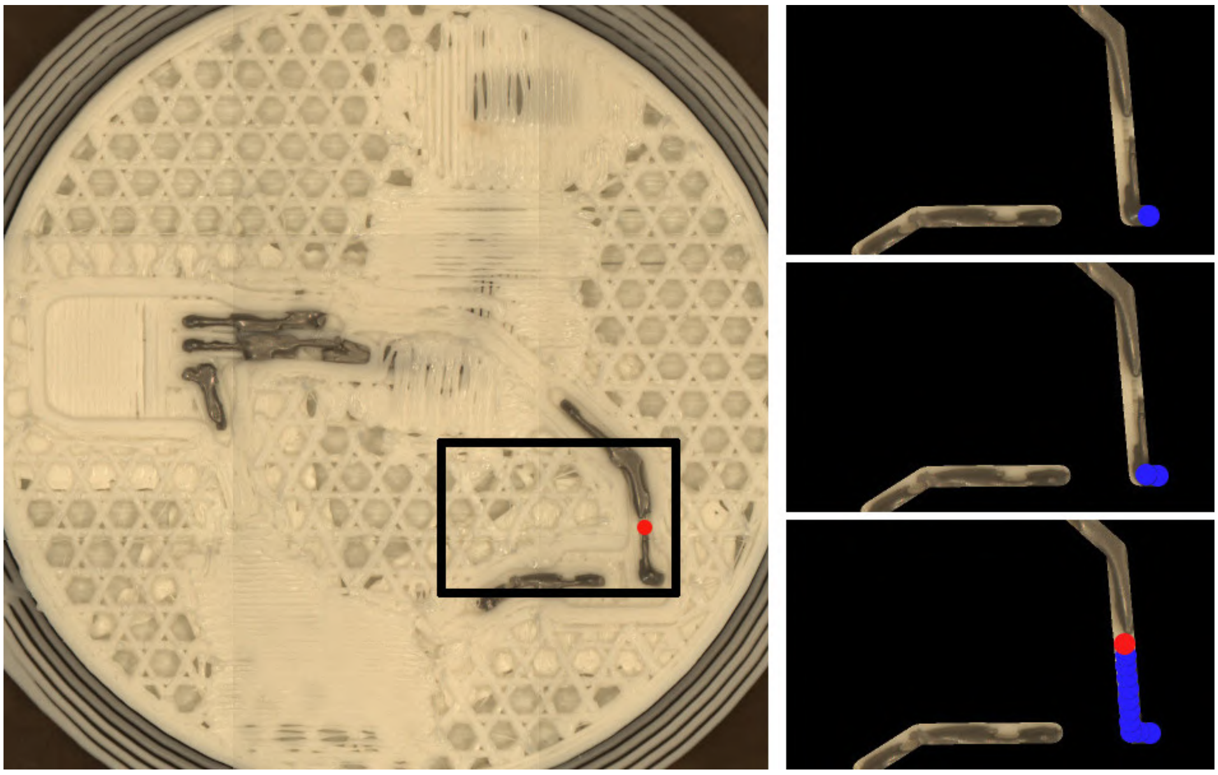

Figure 6.8 – A circular sliding window detector (blue), traversing the first ink extrusion line (top to bottom).

To evaluate the performance of the defect detection pipeline, and to test the integration into the printing process and the effect on execution time, a series of test objects were printed. Five specimens with different filament colors and object shapes were manufactured with a total number of 20 layers containing conductive traces. The syringe extruder was intentionally de-calibrated for these prints to increase the probability of defects to generate relevant test data. The recorded images were inspected and labeled manually, and then compared to the automatic detection results. All disruptions and trace deviations in the evaluation dataset were successfully detected, some relevant cases with highlighted defects are provided in fig. 6.9.

To be suitable as a monitoring tool, running continuously in the background during the daily business in a laboratory or production environment, the entire verification pipeline should be implemented efficiently so as not to excessively extend the overall printing-time.

Table 6.1 lists the amount of time required for the individual steps to print and verify a single layer on the test objects. The verification process (image stitching and analysis) requires approximately $\sim$1.0 % additional execution time per layer, which is considered reasonable. However, the image capturing step currently requires a significant amount of extra time ($\sim$10.0 % or 4.1 s per image). This is due to the positioning of the camera, followed by image capturing, cropping and import of the image on the (slow) CPU of the 3D printer. Interleaving the printhead motion and off-loading image processing to a (much faster) PC would reduce the reported time for image capture dramatically.

	Cube		Cylinder	
Tiles	8 (2x4)		9 (3x3)	
Printing	252.0 s	87.7 %	360.0 s	89.7 %
Image capturing	33.1 s	11.5 %	37.2 s	9.3 %
Stitching	0.8 s	0.3 %	2.7 s	0.7 %
Analyzing	1.5 s	0.5 %	1.6 s	0.4 %
Sum	287.4 s		401.5 s	

Table 6.1 – Processing time of a single layer, broken down into the steps of the verification pipeline

The sliding-window-based, negative coverage test introduced in this section is a fairly simple approach. Yet it proves the feasibility of the idea and already finds most of the defects which typically occurred during the experiments. Future work should consider the implementation of additional and more sophisticated defect detection methods.
This includes a negative coverage detector to identify overextrusions and short circuits by testing for absence of ink in a similar way. A check for sufficient ink extrusion, covering the connector footprint outline for all SMD components before placing them could also be implemented with a combination of both test approaches.
Another promising approach is a connected components detector which can be used to verify both an intact connection between two endpoints (one component) and an intact gap between two wires (two components). The basic idea is to define a set of two or more points which lie inside of an ink-covered region and then apply a flood-fill or similar algorithm to the classified pixels to identify the connected components.

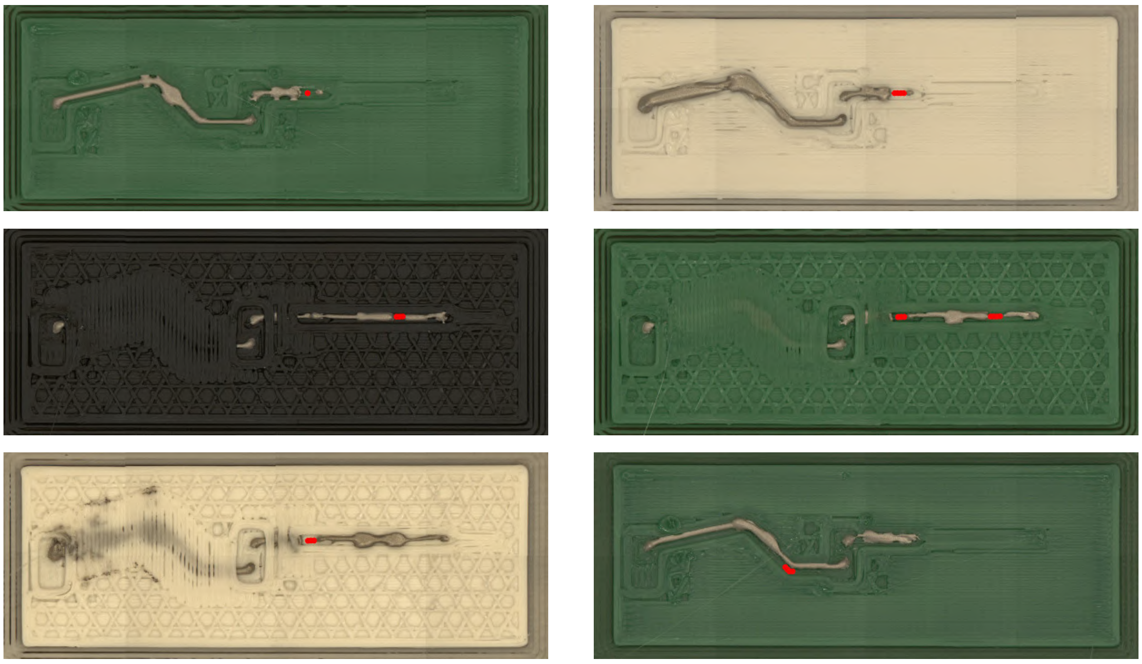

Figure 6.9 – Objects printed with intentionally de-calibrated syringe extruder to evaluate the detector performance. Defects automatically detected by the verification algorithm are highlighted in red. For this test dataset, the algorithm detected 100 % of all defects.

Chapter 7

Experimental Applications and Evaluation

This chapter summarizes several Experiences and results collected during the experiments with the hardware, software and materials. Section 7.1 provides an overview of different plastics used throughout the work on this thesis and assesses their suitability for this application. Several printed objects and case studies for potential applications of the technology developed in this work are presented in sec. 7.2. The chapter closes with a performance analysis of the slicing and routing algorithms.

7.1 Plastics

A broad range of different plastic base materials is a available for the FDM process. While this work is focused on the algorithmic and integration aspects of 3D printed electronics, basic requirements for material properties must be considered. Industrial applications often require high performance materials with high strength, thermal- and UV-stability and low hygroscopy. Integration of printed electronics partly has contradictory requirements. Important properties are:

Temperature High temperatures of both the extruded plastic and ambient conditions (heated chamber) result in faster curing of the conductive ink. This has a positive effect on wires which are partly sintered before the next layer is printed, but reduces adhesion of components placed into uncured ink.

Printbed Adhesion Good printbed adhesion is a general requirement. However, “overfilling” of the first layer to increase adhesion causes severe risks to printed electronics as the overfilling perpetuates over the first few solid layers, causing extrusions to spill into the channels.

Warping Low warping also is general requirement, but for printed electronics even small deviations induce defects e.g. by shifting the contact pins for SMD components.

Stringing Stringing occurs when the extrusion is stopped and the extruder jumps to a different position. The molten plastic does not shear-off clean but often pulls strings with very low diameter. Such strings were a frequent cause of defects in our experiments. Figure 7.1 illustrates the effect of conductive material extrusion crossing a plastic thread. This effect can be partly mitigated in software by tuning the retraction parameters, wiping during retraction moves and raising of the z-axis for travel moves, but material properties and extrusion temperature also have strong effects.

Bonding with Conductive Material Bonding of polymer based inks is excellent on all tested plastic materials but very low for eutectic metals.

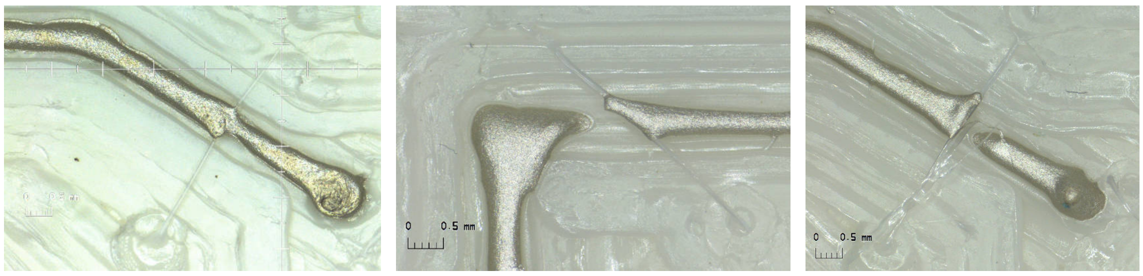

Figure 7.1 – Partly or fully interrupted conductive traces due to stringing from the plastic extruder. The threads are barely visible with naked eye.

Some common plastic filaments were evaluated regarding their suitability as base material for 3D printed electronics: PLA, ABS, PA (PA 6 / Nylon) and flexible filament (NinjaFlex). Carbon fiber reinforced filament was not tested, but is considered to be an interesting candidate.

PLA and ABS were both obtained in different colors and brands. Both materials show similar printing characteristics and are generally suitable to be combined with conductive material. However, PLA exhibits slightly stronger stringing effects and limits the temperature for post curing of conductive material due to its low glass transition temperature.

PA is printable on the machine but requires significant higher extrusion and ambient temperatures and is very sensitive to temperature fluctuations, e.g. when the build chamber is opened to manually insert a component. It is expected that PA materials can be used when the entire process is sufficiently stable and the hardware supports high temperatures e.g. by shielding the conductive material to avoid curing and clogging at the dispenser tip.

Flexible material is currently not suitable for printed electronics as the material flow cannot be controlled with sufficient precision. However, it is an interesting candidate as second material in multi extruder setups.

7.2 Demonstrators

Several demonstrator objects with different features and complexity have been fabricated over the course of this thesis to collect experience with the printer and the slicing software and to test the feasibility of implemented features. While the primary purpose of the first printed objects was testing of individual functionalities, calibration and integration, the user interface (sec. 7.2.2) and the instrumented object (sec. 7.2.3) are case studies where the methods developed in this thesis were applied to solve actual manufacturing problems.

7.2.1 Basic Functional Tests

Figure 7.2 shows one of the very first test objects, printed on the modified CNC milling machine. The design is purely done in OpenSCAD. Object and circuit are two separate volumetric models and printed as multi-material model where each material is assigned to one extruder. Sparse infill, channels, cavities and routing are not supported and were manually designed where required.
The circuit is based on a 8 bit ATmega ATtiny45-20SU microcontroller with two resistors and LEDs. The interface is mechanically compatible to a USB type-A connector. The USB protocol is not supported, instead the interface can be used to program the ATtiny with a customized ISP.

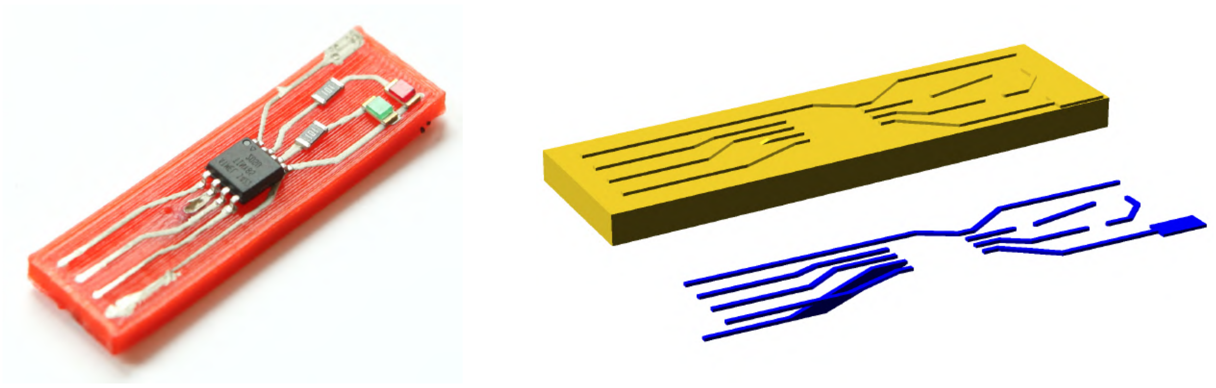

Figure 7.2 – Early test object with a programmable blinking circuit, manufactured on the modified CNC milling machine. The design was done manually as multi-material object composed of two individual volumetric models without software support for channel generation or wire routing.

The flash drive-shaped object shown in fig. 7.3 was mainly used to conduct rapid tests for parameter tweaking and component placing. One end fits the dimensions of a USB type-A connector and can be plugged into any standard USB slot to apply 5V power to the circuit.

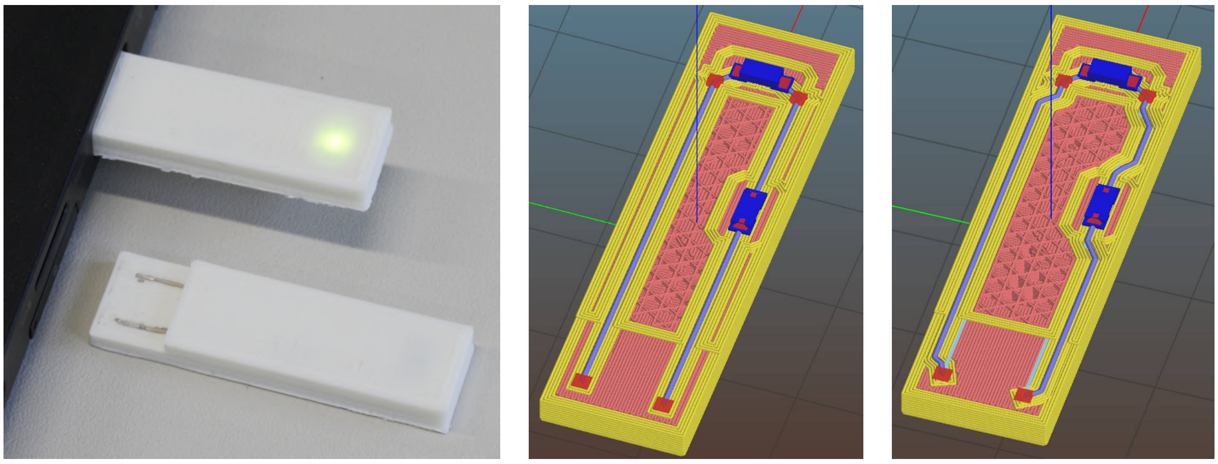

Figure 7.3 – Simple test object consisting of an LED and resistor, with all electronics on a single layer. Power is provided by any USB slot. This object is an example where automatic wire routing can have a negative effect (**right**) as the contact pins are required to follow the mechanic USB interface specifications.

The object in fig. 7.4 was designed to explore three specific aspects:

- The application of topology aware wire routing to a model where manual routing would require a high number of small linear approximations.
- Autonomous energy supply of printed objects with batteries.
- Manual insertion of components (battery) during the printing process which can not be handled by the printer's pick and place system.

The circuit only consists of a single LED and a coin cell battery. The battery is connected at the upper side by printing a conductive trace right onto the surface. A cantilever structure with an embedded wire is printed at the lower side with a small gap to the battery, serving as mechanical switch. Wire routing is achieved by setting only 4 waypoints, two of which are required to contact the battery with a straight line. The routing algorithm successfully finds a collision free path through the object while preserving surface integrity and avoiding gaps. Overlapping inter-layer connections were observed to be stable.

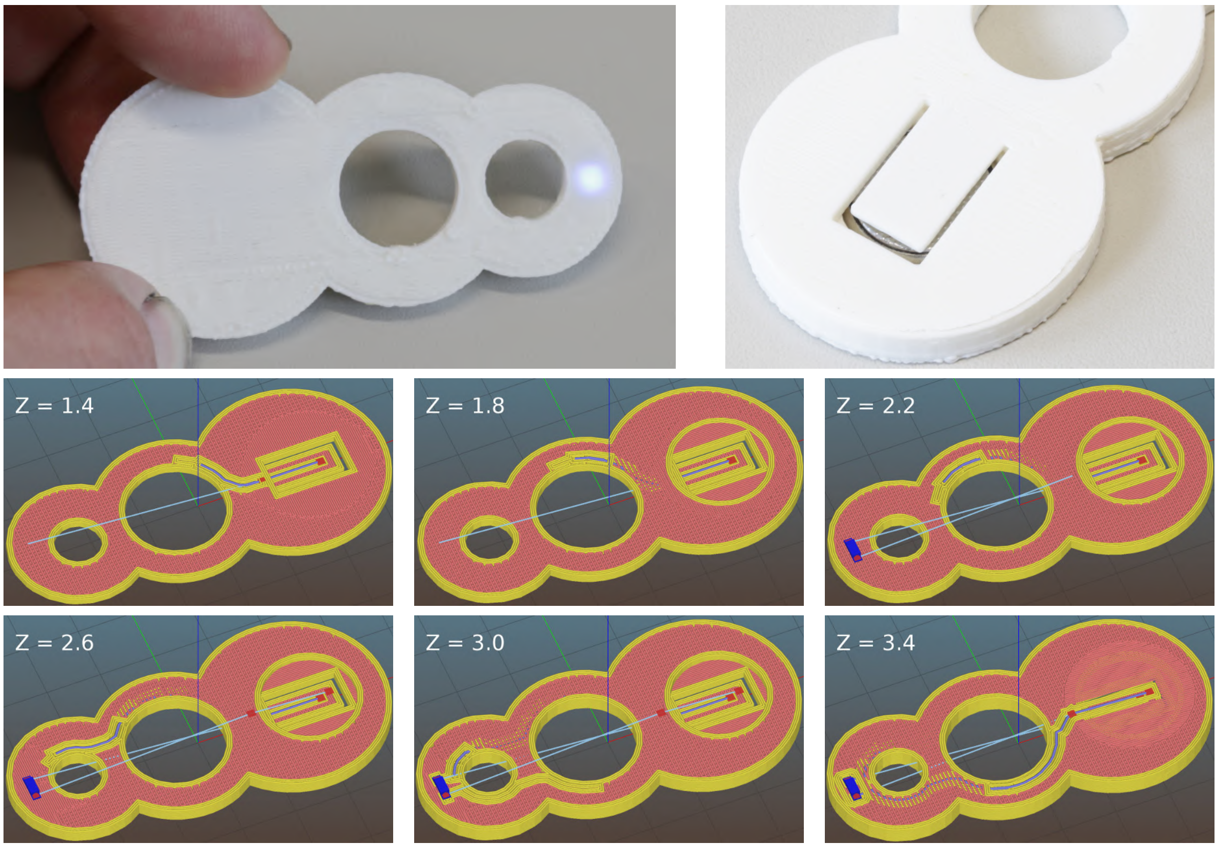

Figure 7.4 – Demonstrator object for topology aware wire routing. **Top**: successful print and detailed view of the printed switch. **Bottom**: Final 3D routing over multiple layers along the curved surface. The circuit contains a coin cell battery and a blue LED with matching voltage requirements. The wires directly contact the battery, with the lower attached to a lever structure, serving as a manual switch. Two additional waypoints are set to ensure a straight line to contact the battery. The images show every second layer of the final tool path. The wires are automatically routed along the surface over several layers, with overlapping sections to achieve stable inter-layer contact.

7.2.2 Case Study: Integrated User Interface

In cooperation with a partner from the industry a pilot study was conducted to evaluate the potential of 3D printed components with integrated electronics for industrial applications. The study was intended as an early feasibility test with a real application. It is anticipated that the process currently does not fulfill all technical requirements to fabricate a fully equal replacement for the current solution. Using specifications provided by an external party ensures that the task is not specifically adapted for the existing solution, but it still allows to adjust the design or selection of components to suit for the additive process.

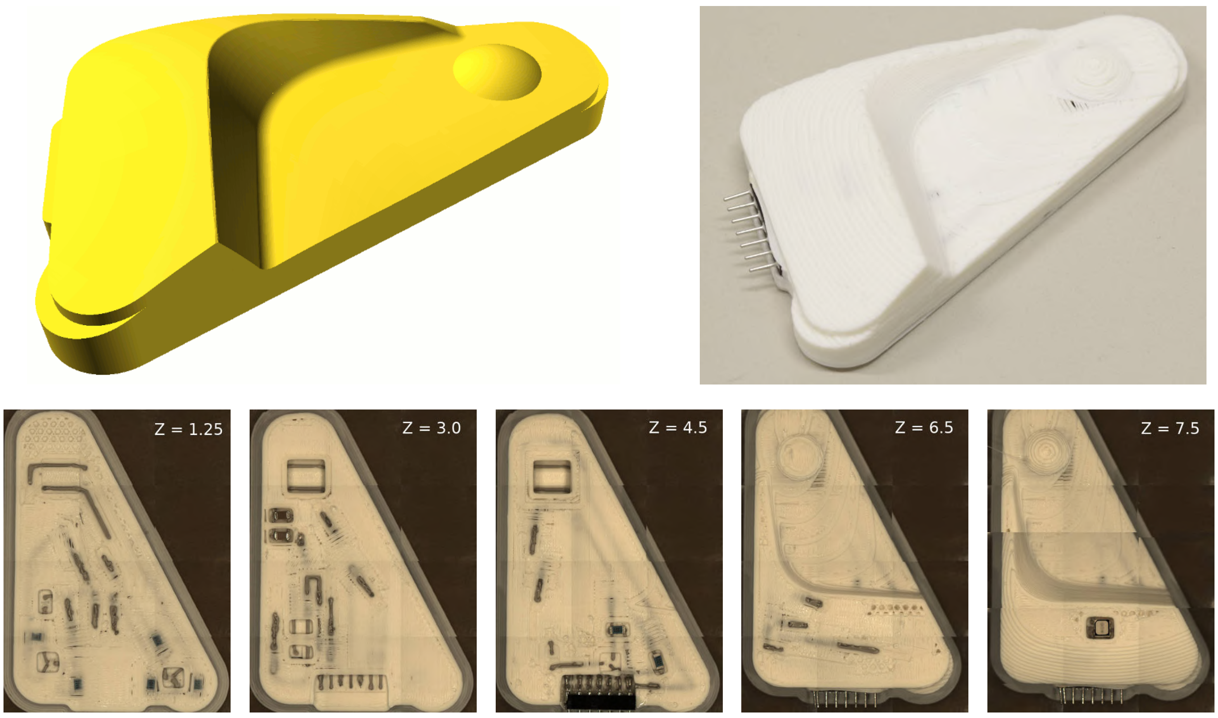

Figure 7.5 – User interface section cut out from a larger device for simplified testing. A mechanical switch and an RGB-LED are integrated into the closed free-form surface. Several additional components are required to connect the interface to the central controller. **Top**: 3D model and printed object with integrated circuit. **Bottom**: documentation of the print process. Note that the images are partially assembled after the print as documentation covers only those parts of the current layer where material was deposited.

The aim of this study was to replace a simple user interface for a communication system, mainly consisting of an RGB-LED and a switch, with a part that can be additively manufactured in a single process step. Figure 7.5 shows a cutout of the free-form surface where the interface is integrated (left), the printed result, including the full circuit (right), and the manufacturing process (bottom). The LED, switch, and the pins for the connection to a controller are positioned at different heights. To a certain level, both the inside of the part and the circuit must be protected against liquids from the outside, requiring the surface to be closed and not interrupted by electronic components. Several additional electronic components are required to amplify the current for the LED and to debounce the switch (detailed list below). One requirement, therefore, was to integrate the entire circuit into the printed surface to eliminate an additional circuit board.

The circuit contains a total of 19 components:

Qty	Type	Package
1	SMD Pinhead	2.0 mm flat
1	APEM DTSJW65NV mechanical switch	Custom
2	Resistor $220\,\Omega$	1206
1	Resistor $470\,\Omega$	1206
6	Resistor $1.0\,\mathrm{k}\Omega$	1206
2	Capacitor $10\,\mathrm{nF}$	1206
2	Capacitor $100\,\mathrm{nF}$	1206
1	Osram LRTB GVTG RGB-LED	PLCC-6
3	SSM3K339R MOSFET	SOT-23F

Several iterations of the part where printed. The complexity was gradually increased. Beginning with simple isolated component tests, more individual components were integrated into one object in each manufacturing step.

A printed mechanical switch was already successfully tested with the “flashlight” object from fig. 7.4. This approach was not directly applicable here, as it requires a gap around the elastic cantilever structure. We therefore attempted to use a common mechanical SMD-switch, covered by a thin elastic layer of plastic. Figure 7.6 (1) shows the isolated test object. Actuating the switch required a high amount of force ($\sim 50\,\mathrm{N}$) due to the rigid elevated surface and narrow cavity. Increasing the cavity offset improved the result, but the soft filament surrounded the small button to an extent where it prevented the switch from triggering (2 and 3). As a countermeasure, a thin plate was attached to the switch to increase the filament support area (4). Additionally, a cutout was added to the model at the upper boundary of the switch (5). This causes a large membrane-area and at the same time allows to use narrow cavity offsets, such that the space around the switch can be used for other components. The improved version still requires $\sim 20\,\mathrm{N}$ to trigger the switch, which is at the upper limit of subjective acceptance reported by several test persons. The cutout can currently not be modeled as part of the electronic component package, as only extruded 2D-shapes are supported. Full 3D-component models are considered an important future improvement of the slicing software.

Printed circuits are typically small, with minor complexity but at exactly the position where they are required, e.g., in-situ sensors or small interfaces. The printed parts commonly need a connection to a power source or a central computing device, requiring means to connect a cable. While small components are electrically connected and sufficiently affixed by the conductive paste and the enclosing cavity, larger connectors, e.g., pinheads or plug sockets would be teared off by a connected wire. A second test was conducted to mount a pinhead during the printing process. The pinhead was wetted with a two-component epoxy glue before insertion. Figure 7.6 shows the pinhead during the print process (6) and fully enclosed (7). Both mechanical and electrical connections were sufficiently stable to connect the required 7-core cable.

During the isolated component tests, a first version of the interface object with a reduced circuit without the LED-drivers was manufactured. Figure 7.7 (right) shows the result. At the design

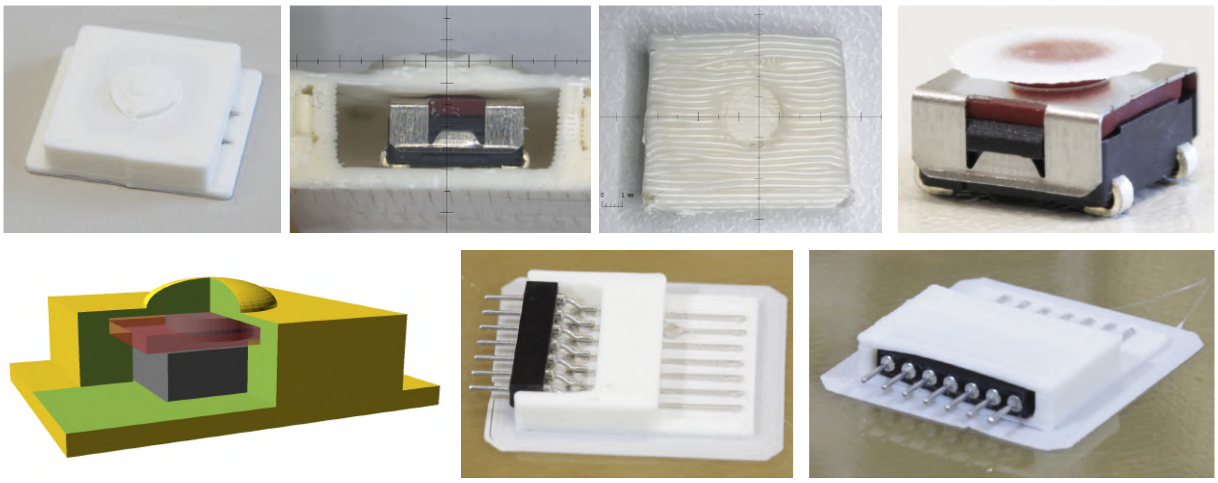

Figure 7.6 – Isolated testing of mechanical components. From top left to bottom right: **1**: SMD-switch in a minimal, printed housing. **2, 3**: Cross-section, clearly showing that the actuator is enclosed by sagging molten filament. **4**: Thin plate to extend the surface of the switch for better filament support. **5**: Extension of the cavity around the switch only for the topmost millimeter (indicated in red) to increase the flexible membrane area while maintaining an otherwise small cavity. **6**: Insertion of a glue-wetted pinhead during the print process. **7**: Resulting part with inset connector.

phase, it became evident that due to the limited space, some components had to be placed in close proximity, resulting in touching or even merged cavities. While placing multiple components in a single cavity worked well, Slic3r's bridging algorithm, which is used to cover the cavities with the first unsupported layer, turned out to be not well suited for this task. The effect is illustrated in fig. 7.7. The algorithm generally attempts to identify the primary orientation of a bridging area and aligns the extrusions with this direction to ensure a proper connection to the solid object at both ends of each line. With the irregular shapes induced by components with slightly different heights and orientations, the algorithm detects two or more principal directions and splits up the area into multiple bridging surfaces. When the extrusion line ends on top of a component, it a) does not stick to the plastic surface, resulting in a small clot of tangled filament, which then b) often shifts the component out of place.

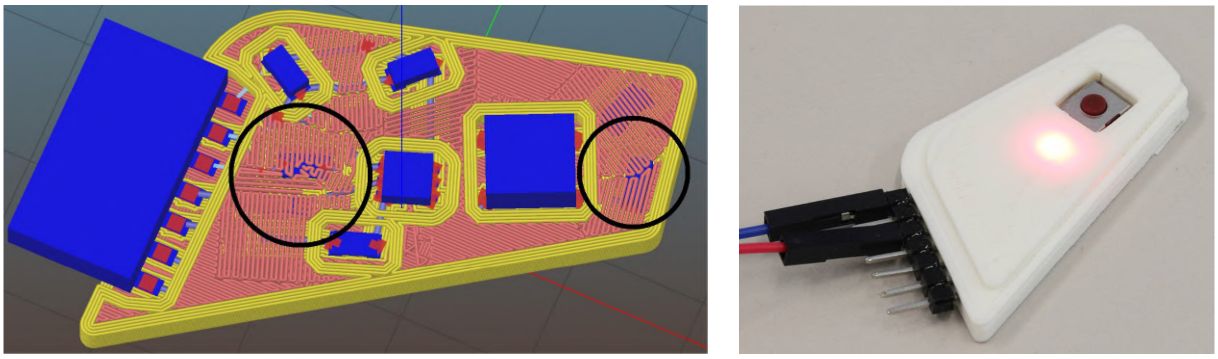

Figure 7.7 – **Left**: unsuitable result of the bridging algorithm when components are arranged in close proximity. **Right**: successful print after rearranging the components to avoid the bridging issues.

7.2.3 Case Study: Instrumented Object

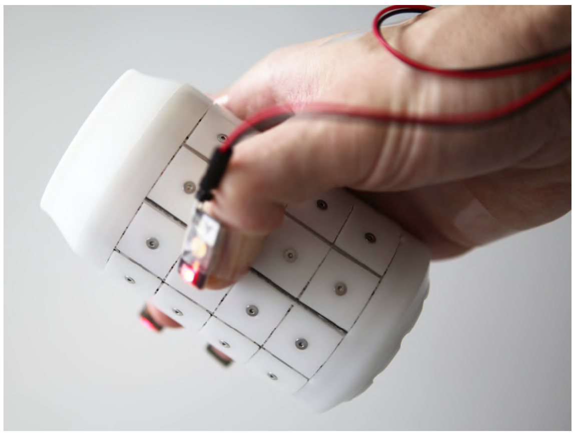
Figure 7.8 – Can-shaped tracking object with tactile feedback.

The instrumented object approach was initiated during the European project HANDLE FP7-236410 and further developed within the Transregio Project Crossmodal Learning, TRR 169 [B31]. The general idea is to accomplish in-hand manipulation of objects with robotic multi-finger grippers (e.g. Shadow Dexterous Hand [B28]) by generalization from recorded demonstration movements, executed by human persons [A9]. A setup of several precisely calibrated cameras and optical markers was used to record the demonstrator movements with high spatial and temporal resolution. However, external tracking suffers from two major drawbacks:

1. The object often is partly or fully covered by the hand during a manipulation, rendering external tracking very unreliable.
2. Contact forces between hand and object are crucial information which cannot directly be obtained from optical observation. The location, amount and direction of force applied to the object at each contact point are of particular interest.

The proposed solution is an object with integrated active tracking and tactile sensing capabilities, mainly being a touch-sensitive surface to record forces, an Inertial Measurement Unit (IMU) for position tracking and a wireless connection to stream recorded data to an external storage system. The prototype illustrated in fig. 7.8 resembles a can, commonly used for beverages. The object consists of 40 individual tactile switches mounted on a massive metal frame. The switches are connected via 10 individual PCBs with a total of more than 300 electronic components. The manufacturing of this prototype required significant resources and the design turned out too be to large and too heavy for many dexterous manipulation tasks.

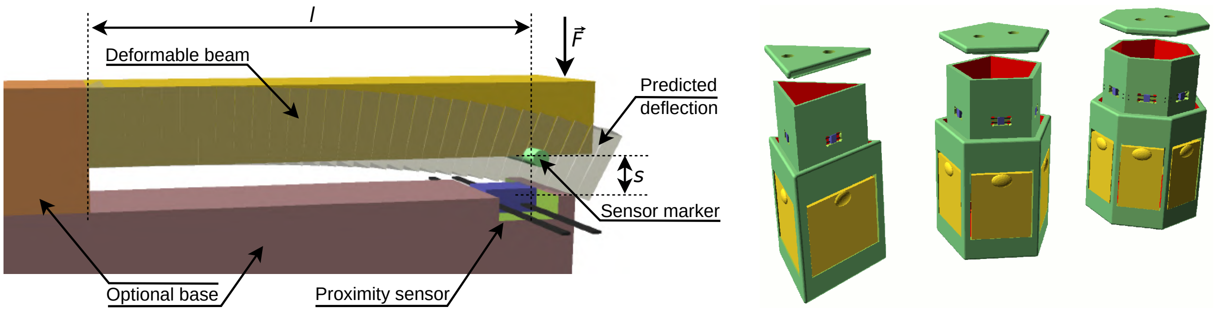

Figure 7.9 – **Left**: rendering of the basic one dimensional push-force sensor, with the deformable beam on top and above the optical proximity sensor. To help the designer to dimension and align the sensor, the rendering optionally also includes the sensor marker (green), the fully deflected beam (gray), and a model of the proximity sensor (blue). **Right**: variations of the instrumented object based on the same basic design.

Based on our previous research on printable force sensors [A94], a flexible design approach for printable instrumented objects was developed. Additive manufacturing allows to quickly produce objects of different shapes and sizes, evolving with the progress of recording a larger dataset of manipulation movements, without the requirement for expensive force sensors.

Figure 7.9 illustrates the (well known) basic principle of the printed force sensors based on a deformable cantilever. If the mechanical properties of the structure are known, the force inducing the deformation can be computed. Low-cost optical proximity sensors are used to measure the deflection. The sensor consists of an IR-LED transmitter and a photo-transistor, changing its resistivity depending on the reflection of emitted IR-light. Figure 7.9 (right) also shows how such cantilever structures are used as flexible surface of the instrumented objects, each with a proximity sensor below it, mounted on the surface of the inner structure. The inner part of the object contains all electronics and power supply. The force sensitive hull is printed as an individual component and can be quickly replaced to adjust the sensitivity by changing the thickness of the cantilever structures.

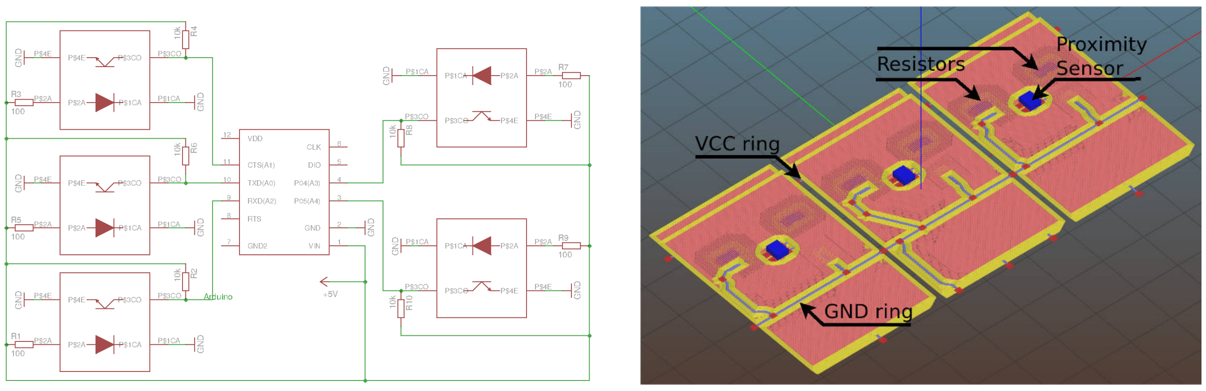

Figure 7.10 – **Left**: EAGLE schematic of an instrumented object with 5 force sensitive surfaces. **Right**: G-code for three of the five side plates with integrated electronic components.

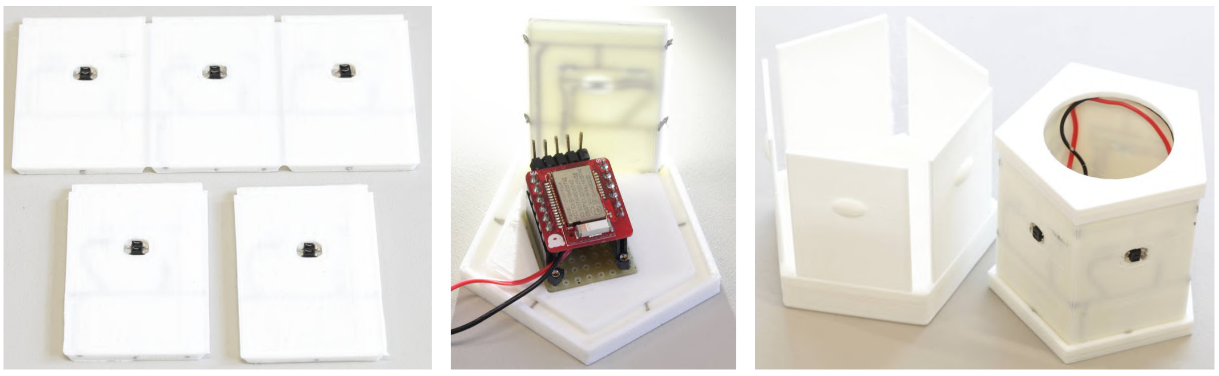

Figure 7.11 – Assembling of the instrumented object demonstrator. **Left**: three sides printed as a foldable object (top) and two single pieces (bottom). **Center**: base plate with microcontroller and first mounted side plate. **Right**: fully assembled object and deformable reflective hull.

Figure 7.10 shows the full schematic for a 5-sided instrumented object. The design contains a total of 16 electronic components:

Qty	Type	Package
1	Redbear BLE Nano / nRF52832 SoC	Breakout board
5	Resistor 100 Ω	1206
5	Resistor 10 kΩ	1206
5	Everlight ITR8307 proximity sensor	Custom

Each proximity sensor is individually connected to one of the built-in AD-converters of the BLE Nano board. The board itself is mounted to the printed base via a socket to allow re-programming which requires removal from the instrumented object.
Since placing of electronic components is currently only possible in one direction, on flat surfaces, the design was split into a base-plate, containing the microcontroller and Bluetooth connector (fig. 7.11, center) and a number of side-plates which fit into a notch (fig. 7.11, left). Individual parts are connected by wires terminating at the edges, physical contact is established by plugging the part into the notch. The side-plates can be printed individually or as a set, connected by a thin layer of plastic to be bent at the corners after printing to form a hull. Each plate contains the proximity sensor and two resistors, wired with a set of connections routed in 3 dimensions to avoid collisions.

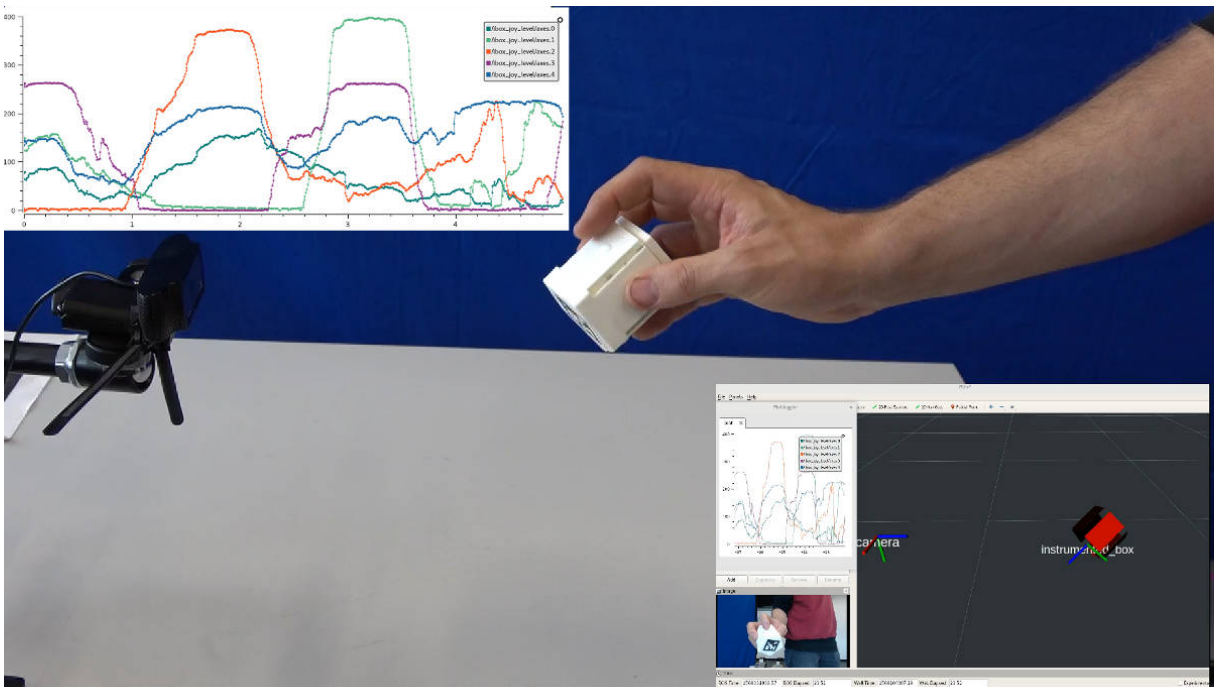

Figure 7.12 – Data recording with the printed instrumented object in a simplified tracking setup. The object position is optically tracked via visual marker. Force- and position-data are recorded, visualized and further processed with the Robot Operating System (ROS).

Figure 7.12 shows a first (simplified) data-collection experiment with the printed instrumented object. A camera provides absolute external reference for position tracking. Object position and current forces are visualized during the experiment in a 3D scene representation (RViz) and recorded for subsequent evaluation. Force sensor data are streamed as raw ADC values to the host computer and pre-processed to compensate different zero-points and to map from the non-linear proximity sensor characteristic to linear forces. The Bluetooth LE module currently allows a sampling frequency of approximately 140 Hz.

7.3 Performance

The amount of time to generate an executable G-code sequence from a model (seconds to minutes) is small compared to the time it takes to physically print the object (hours to days). Therefore, good optimization at the slicing step is generally worth some extra time if it reduces the risk of failure during the print process. However, since the slicing steps are frequently executed to provide an accurate preview of the result when the position of electronic components or wires is changed, the runtime of algorithms has a significant impact on the user experience.

To analyze the execution time, the designs of four of the objects introduced above where sliced without any electronics, with electronics but disabled routing and finally with contour following routing enabled. All objects where sliced with the same set of parameters on an Intel Core i5-8350U CPU. The relevant parameters used for the routing algorithm during this experiment were:

Grid resolution	ε (Heuristic)	Γ (Inter-layer cost)	α (perimeter weight)
1.0 mm	1.0	1.5	0.1

The results are presented in fig. 7.13. The additional time required for the contour following routing algorithm is so dominant that the other two cases are only visible in the logarithmic representation (right).
A direct comparison is not always possible. Consider the batty light object. The slicing step was executed exactly with the waypoints shown in fig. 7.13. With this configuration, the static routing approach does not yield a printable result, but instead just creates straight wires, crossing both holes.

As expected, the runtime also heavily depends on the A* graph search parameters and object shape. To estimate the effect, the battery light object was also processed with a combination of different parameters:

	Grid resolution	ε (Heuristic)	Γ (Inter-layer cost)	Runtime
Baseline	1.0 mm	1.0	1.5	28.7 s
Resolution	**1.5 mm**	1.0	1.5	17.6 s
	2.0 mm			20.1 s
	3.0 mm			18.3 s
ε	1.0 mm	**1.1**	1.5	25.4 s
		1.3		24.4 s
Γ	1.0 mm	1.0	**0.0**	35.3 s
			3.0	24.7 s
			5.0	18.9 s
Combined	**1.5 mm**	1.0	**5.0**	11.2 s

For each row, the altered parameter is highlighted in bold text. All other parameters are fixed, the baseline is identical with the parameters in the execution time analysis in fig. 7.13.

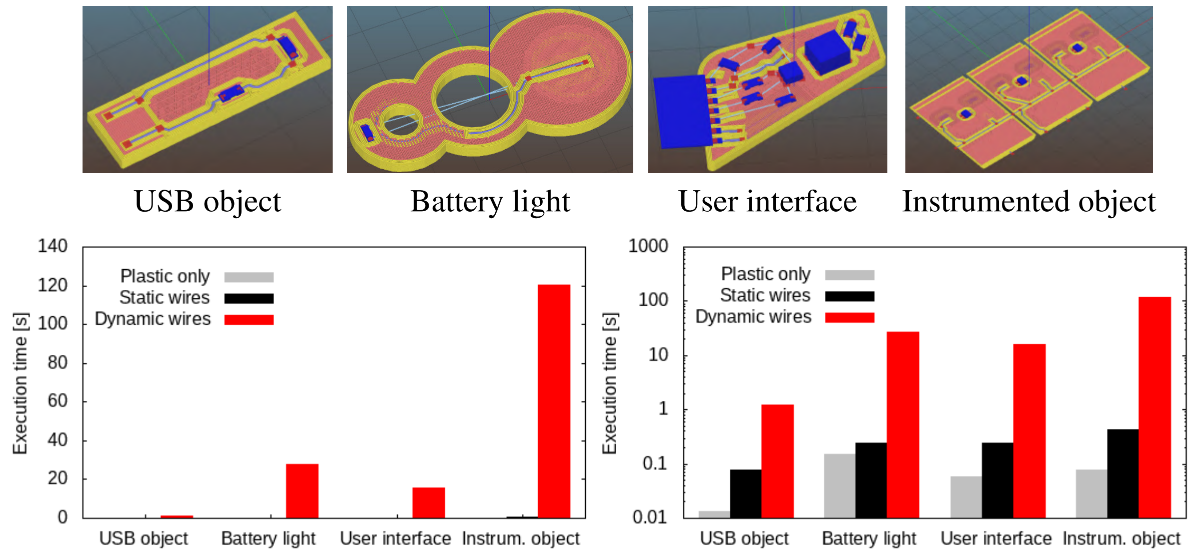

Figure 7.13 – Execution time to generate the G-code of the four objects without electronics (grey), with static (black) and contour following wire routing (red). The left diagram shows the actual execution time in seconds, the right diagram presents the same data at a logarithmic scale.

Reducing the grid resolution decreases the runtime as expected. For the object used in this experiment, the effect is limited as the infill area is small compared to the object's surface. The sampling along the perimeter must be high enough to ensure overlapping inter-layer connections. The number of evaluated perimeter vertices is therefore significantly higher than the number of infill vertices.

Increasing the heuristic factor ε yields slightly lower runtimes at the cost of less optimal trajectories.

The layer-changing cost Γ also significantly affects the runtime. A low value prefers horizontal exploration, including several adjacent layers while a high value minimizes the number of layer changes for the potential cost of longer in-layer detours. The special case of $\Gamma = 0$ eliminates layer changing costs at all, often resulting in an "undulating" trajectory, jumping up and down between the layers.

In a second step the code execution time was profiled to identify critical sections with high potential for optimization. All performance relevant parts of the code are written in C++, but executed through Perl's XS-mechanism, complicating the insertion of instrumentation code. Therefore the `perf` profiling tool, included in the Linux kernel, was used for statistical profiling. The accuracy of this method is limited, as the process is only polled at certain intervals, but good enough to identify hot-spots. The combined three side plates design for the instrumented object (fig. 7.11, left) was used for analysis to record a sufficient amount of statistical data.

The result is provided in fig. 7.14. Only functions with a high share of the runtime are shown. The routing algorithm accounts for ~95 % of the total runtime. Within the routing subroutine, 79.6 % of the time is allotted to the `Point::projection_onto` function, which is used to test if a point is inside a polygon or on the polygon boundary and by the perimeter alignment step described in sec. 5.3.2 (cf. fig. 5.20).

Further optimization steps should focus on the handling of polygon representations. Promising approaches are caching of results or representation with an R-tree based data structure for efficient spatial indexing.

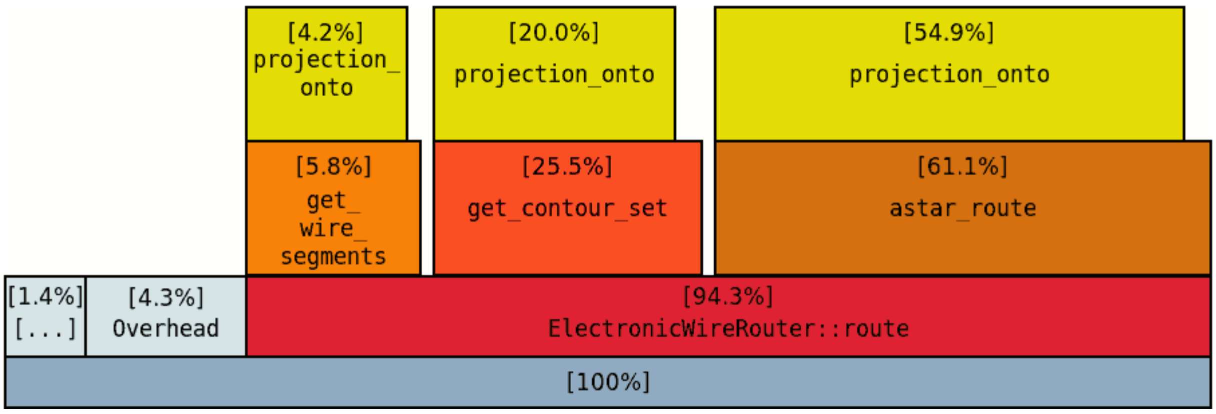

Figure 7.14 – Runtime profiling results for G-code generation with topology aware routing enabled, visualized as simplified flame graph. The share of execution time is given in percent. Only functions with high contribution are shown for clearance. The routing subroutine accounts for $\sim 95\%$ of the computing time.

Chapter 8

Conclusions and Outlook

In this thesis a full toolchain for additive manufacturing of objects with integrated electronics was developed and successfully used to print several working demonstrators.
In conclusion, the research questions from sec. 1.3 can be answered as follows:

Mechanical Engineering & Integration: Two iterations of 3D printers were developed to integrate extrusion capabilities for plastic and conductive material and automatic component handling. A set of software tools was developed to calibrate and control the machine with vision feedback. Several types of plastic and conductive substances were evaluated and suitable materials were identified.

3D-Electronics Design: A combination of mCAD and eCAD data was achieved by combining them within the slicing software. Electronic components and wires are visualized in a graphical representation of the tool path which would be generated by this arrangement. This representation gives the user an immediate and realistic impression of the result.

2D & 3D Wire Routing Algorithms: A printable G-code is generated based on a graph-based routing algorithm and polygon manipulations utilizing the existing mechanisms for tool path generation and surface detection. The algorithm minimizes layer changes and aligns the trajectories with existing contours where possible, based on the process parameters of each individual print.

Process Verification: The quality and correctness of circuits immersed in plastic is documented and verified by taking high-resolution images with the printer's camera and comparing them with the G-code by means of image processing to automatically detect defects.

The core contribution of this work is an approach to combine the volumetric 3D structure of an object and an electronic circuit with the parameters of the FDM printing process into a representation which can be utilized for well-known routing algorithms. This is achieved by modeling it as a combination of a graph data-structure and contour polygons, allowing to infer possible connections within and between layers. Several successful approaches have been made towards the physical integration of conductive materials into additive manufacturing processes in the last decade. The question of how to support and shape the design process to make efficient use of those approaches was widely recognized, but significant research only started in recent years, now coming up with the first useful results.

8.1 Limitations

Despite the successful and very promising results presented throughout the previous chapters, some issues currently prevent a broader commercial application of the technology discussed in this thesis.

The mechanical positioning accuracy and reliability of the machines used for our experiments is still insufficient, requiring frequent calibration and minor offset corrections and limiting the resolution achievable. The usage of syringe extruders for direct write application of conductive ink is another limitation for both reliability and resolution. A promising alternative could be contactless dispensing via a piezo-driven jetting nozzle. A commercial product solving this problem, as it is already done in many other areas, was not available at the beginning of this work. Only recently are hardware manufacturers starting to develop integrated solutions. With sufficient investments the technology should be available within few years.

The efficiency and overall usability of the user interface and routing algorithms still needs improvement. Waiting up to several minutes for the updated preview after a design change for a circuit with only a few components is sufficient for an experimental prototype, but not acceptable in a production scenario.

True 3D circuits are possible and have been demonstrated with this thesis. However, the staircase approach limits the angle, near vertical wires are currently not possible. The same problem occurs for the positioning of components which is currently limited to z-rotations. Multi-axis manufacturing systems and non-planar slicing approaches both have the potential to solve this issue, particularly for connections and components following curved surfaces.

Eventually, a very fundamental question is: will the FDM approach be suitable as the base technology in the long run? Miniaturization is technically limited with extrusion based processes. Many manufacturers also report that other additive processes are better suited to fulfill their requirements on stability, surface quality and scaling for mass production. However, neither powder- nor resin-based approaches currently have the maturity and stability to be used in productive manufacturing setups within the next few years.

8.2 Future Research

The usability and efficiency of the routing algorithm and the user interface can and should be further improved. Several low-hanging fruit developments can be implemented with low effort. The most important requirements, collected while fabricating the demonstrator objects in sec. 7.2, are:

User Interface The user interface is currently rather simple. All important operations can be executed, but more natural ways of interaction would certainly simplify the design process. This includes: placing of elements on grid to facilitate alignment, drag and drop shifting of components, better labeling of component with relevant information, e.g. value of a resistor.

3D Component Models SMD components are currently represented based on their 2D shape from the EAGLE libraries, which is not sufficient e.g. for the mechanical switch or pinhead used for the user interface in sec. 7.2.2.

Wire Thickness currently, wires are modeled as a single line of extrusion. For high-current applications (e.g. motors) thicker wires would be required. This could be achieved with multiple extrusion lines, but the graph representation currently does not support it.

Support Material Support material generation is not aware of electronic components. This is a problem if parts of a circuits are protruding the perimeter, e.g. connectors.

Coordinate System Registration Electronic components are positioned relative to the object's center of mass. If the 3D model is modified such that the CoM changes, repositioning of all components is necessary.

Component Referencing Oftentimes, component models have to be slightly modified in the schematic, as they are originally intended for usage on PCBs. Saving a deviated model with a different name removes the component from the 3D design entirely.

The routing algorithm can be further improved in terms of efficiency. This could probably achieved by utilizing index-based data-structures as indicated in sec. 7.3. A second option would be to make the routing algorithm itself more adaptive. Adapting the grid size to the topology of the current object or starting with a coarse grid with iterative refinements only in sections affected by the search are promising approaches.
Another option would be backtracking and partial replanning of routes. This could also considerably contribute to improved collision avoidance. Similar techniques, e.g. Rip-Up and Reroute (RRR) have a long tradition in conventional wire routing.

Finally, overcoming the 3-axis limitation is an important research field to evolve from the stacking of two-dimensional layers to even more three-dimensional fabrication. Promising approaches are 4- or 5-axis machines as they are commonly used for machining. While the hardware already exists, collision avoidance and G-code generation for additive processing still pose major challenges. Other options is the combination of a common 3-axis gantry system to print the plastic part with a robotic arm for ink deposition along free-form surfaces and component handling.

References

[A1] Max K. Agoston. *Computer Graphics and Geometric Modelling*. Springer, 2005. ISBN: 9781852338183.

[A2] Daniel Ahlers. “Development of a Software for the Design of Electronic Circuits in 3D-Printable Objects”. Bachelor Thesis. University of Hamburg, 2015. URL: https://tams.informatik.uni-hamburg.de/publications/2015/BSc_Daniel_Ahlers.pdf.

[A3] Daniel Ahlers, Florens Wasserfall, Norman Hendrich, and Jianwei Zhang. “3D Printing of Nonplanar Layers for Smooth Surface Generation”. In: *Proceedings of the 15th IEEE Conference on Automation Science and Engineering (CASE)*. Vancouver, 2019, pp. 1737–1743.

[A4] Kimball Andersen, Yue Dong, and Woo Soo Kim. “Highly Conductive Three-Dimensional Printing With Low-Melting Metal Alloy Filament”. In: *Advanced Engineering Materials* 19.11 (2017), p. 1700301. DOI: 10.1002/adem.201700301.

[A5] Markus Ankenbrand, Yannic Eiche, and Jörg Franke. “Mechatronic Integrated Devices”. In: *2019 International Conference on Electronics Packaging (ICEP)* (2019), pp. 273–278.

[A6] Callum Bailey, Efrain Aguilera, David Espalin, Jose Motta, Alfonso Fernandez, Mireya A. Perez, Christopher Dibiasio, Dariusz Pryputniewicz, Eric MacDonald, and Ryan B. Wicker. “Augmenting computer-aided design software with multi-functional capabilities to automate multi-process additive manufacturing”. In: *IEEE Access* 6 (2017), pp. 1985–1994. DOI: 10.1109/ACCESS.2017.2781249.

[A7] Sandra Balzereit, Friedrich Proes, Volker Altstädt, and Claus Emmelmann. “Properties of copper modified polyamide 12-powders and their potential for the use as laser direct structurable electronic circuit carriers”. In: *Additive Manufacturing Journal* 23 (2018), pp. 347–354. DOI: 10.1016/j.addma.2018.08.016.

[A8] Jacob Bayless, Mo Chen, and Bing Dai. *Wire Embedding 3D Printer*. 2010.

[A9] A. Bernardino, M. Henriques, N. Hendrich, and J. Zhang. “Precision grasp synergies for dexterous robotic hands”. In: *2013 IEEE International Conference on Robotics and Biomimetics (ROBIO)*. Dec. 2013, pp. 62–67. DOI: 10.1109/ROBIO.2013.6739436.

[A10] Marc Bestmann, Bente Reichardt, and Florens Wasserfall. "Hambot: An Open Source Robot for RoboCup Soccer." In: *19'th RoboCup international Symposium, Hefei*. 2015. DOI: 10.1007/978-3-319-29339-4_28.

[A11] Marc Bestmann, Florens Wasserfall, Norman Hendrich, and Jianwei Zhang. "Replacing Cables on Robotic Arms by Using Serial via Bluetooth". In: *Proceedings of the IEEE Conference on Robotics and Biomimetics (ROBIO)*. Macao, 2017, pp. 189–195. DOI: 10.1109/ROBIO.2017.8324416.

[A12] Xiaorui Chen and Sara McMains. "Polygon offsetting by computing winding numbers". In: *Proceedings of the ASME international design engineering technical conferences and computers and information in engineering conference* 2 (2005), pp. 565–575.

[A13] Keun-Ho Choi, JongTae Yoo, Chang Kee Lee, and Sang-Young Lee. "All-inkjet-printed, solid-state flexible supercapacitors on paper". In: *Energy & Environmental Science* (2016). DOI: 10.1039/C6EE00966B.

[A14] Chris Chu and Yiu-Chung Wong. "FLUTE: Fast Lookup Table Based Rectilinear Steiner Minimal Tree Algorithm for VLSI Design". In: *IEEE Transactions on Computer-Aided Design of Integrated Circuits and Systems* 27.1 (2008), pp. 70–83. DOI: 10.1109/TCAD.2007.907068.

[A15] Thomas H. Cormen, Charles E. Leiserson, Ronald L. Rivest, and Clifford Stein. *Introduction to Algorithms*. MIT Press, 2009. ISBN: 9780262032933.

[A16] Erick De Nava, Misael Navarrete, Amit Lopes, Mohammed Alawneh, Marlene Contreras, Dan Muse, Silvia Castillo, Eric Macdonald, and Ryan Wicker. "Three-Dimensional Off-Axis Component Placement and Routing for Electronics Integration using Solid Freeform Fabrication". In: *Proceedings of the 19th International Solid Freeform Fabrication Symposium* (2008), pp. 362–369.

[A17] Ugandhar Delli and Shing Chang. "Automated Process Monitoring in 3D Printing Using Supervised Machine Learning". In: *Procedia Manufacturing* 26 (2018), pp. 865–870. DOI: 10.1016/j.promfg.2018.07.111.

[A18] Christian Emmer, Arnulf Fröhlich, Volker Jäkel, and Josip Stjepandić. "Standardized Approach to ECAD / MCAD Collaboration". In: *Proceedings of the 21st ISPE Inc. International Conference on Concurrent Engineering* (2014). DOI: 10.3233/978-1-61499-440-4-587.

[A19] David Espalin, Danny W. Muse, Eric MacDonald, and Ryan B. Wicker. "3D Printing multifunctionality: Structures with electronics". In: *International Journal of Advanced Manufacturing Technology* 72 (2014), pp. 963–978. DOI: 10.1007/s00170-014-5717-7.

[A20] Alejandro H. Espera, John Ryan C. Dizon, Qiyi Chen, and Rigoberto C. Advincula. “3D-printing and advanced manufacturing for electronics”. In: *Progress in Additive Manufacturing* (2019). DOI: 10.1007/s40964-019-00077-7.

[A21] Georgios D. Evangelidis and Emmanouil Z. Psarakis. “Parametric image alignment using enhanced correlation coefficient maximization”. In: *IEEE Transactions on Pattern Analysis and Machine Intelligence* 30.10 (2008), pp. 1858–1865. DOI: 10.1109/TPAMI.2008.113.

[A22] Matthias Faes, Wim Abbeloos, Frederik Vogeler, Hans Valkenaers, Kurt Coppens, Toon Goedemé, and Eleonora Ferraris. “Process Monitoring of Extrusion Based 3D Printing via Laser Scanning”. In: *ArXiv* abs/1612.02219 (2014). URL: http://arxiv.org/abs/1612.02219.

[A23] Jörg Franke, ed. *Three-Dimensional Molded Interconnect Devices (3D-MID): Materials, Manufacturing, Assembly and Applications for Injection Molded Circuit Carriers*. Hanser, 2014.

[A24] Harry Gao and Nicholas A. Meisel. “Exploring the Manufacturability and Resistivity of Conductive Filament Used in Material Extrusion Additive Manufacturing”. In: *Proceedings of the 28th Solid Freeform Fabrication Symposium* (2017), pp. 1612–1626.

[A25] Ian Gibson, David Rosen, and Brent Stucker. *Additive Manufacturing Technologies*. 2nd Edition. Springer, 2015. ISBN: 9781493921126.

[A26] Johannes Heinrich Glasschröder. “Additiv gefertigte Werkstücke mit integrierten elektrischen Schaltungen unter Nutzung des 3D-Druckprozesses”. PhD thesis. Technische Universität München, 2018.

[A27] Johannes Glasschroeder, Emanuel Prager, and Michael F. Zaeh. “Powder-bed based 3D-Printing of function integrated parts”. In: *Proceedings of the International Solid Freeform Fabrication Symposium*. 2014, pp. 775–792.

[A28] Guo Liang Goh, Shweta Agarwala, Guo Dong Goh, Heang Kuan Joel Tan, Liping Zhao, Tong Kuan Chuah, and Wai Yee Yeong. “Additively manufactured multi-material free-form structure with printed electronics”. In: *International Journal of Advanced Manufacturing Technology* 94.1-4 (2018), pp. 1309–1316. DOI: 10.1007/s00170-017-0972-z.

[A29] Cassie Gutierrez, Rudy Salas, Gustavo Hernandez, Dan Muse, Richard Olivas, Eric MacDonald, Michale D. Irwin, Ryan Wicker, K. Churck, M. Newton, and Brian Zufelt. “CubeSat Fabrication through Additive Manufacturing and Micro-Dispensing”. In: *Proceedings from the IMAPS Symposium* (2011). DOI: 10.4071/isom-2011-THA4-Paper3.

[A30] Antonin Guttman. "R-Trees a dynamic index structure for spatial searching". In: *Proceedings of the ACM SIGMOD international conference on Management of data*. 1984, pp. 47–57. DOI: 10.1145/602259.602266.

[A31] M. Hanan. "On Steiner's Problem with Rectilinear Distance". In: *SIAM Journal on Applied Mathematics* 14.2 (1966), pp. 255–265. DOI: 10.1137/0114025.

[A32] P. E. Hart, N. J. Nilsson, and B. Raphael. "A Formal Basis for the Heuristic Determination of Minimum Cost Paths". In: *IEEE Transactions on Systems Science and Cybernetics* 4.2 (1968), pp. 100–107. DOI: 10.1109/TSSC.1968.300136.

[A33] Martin Hedges and Aaron Borras Marin. "3D Aerosol Jet Printing - Adding Electronics Functionality to RP/RM". In: *Direct Digital Manufacturing Conference* (2012).

[A34] Johannes Hoerber, Johannes Glasschroeder, Michael Pfeffer, Johannes Schilp, Michael Zaeh, and Jörg Franke. "Approaches for additive manufacturing of 3D electronic applications". In: *Procedia CIRP* 17 (2014), pp. 806–811. DOI: 10.1016/j.procir.2014.01.090.

[A35] Mohammad Shojib Hossain, Jose A. Gonzalez, Ricardo Martinez Hernandez, Mohammad Arif Ishtiaque Shuvo, Jorge Mireles, Ahsan Choudhuri, Yirong Lin, and Ryan B. Wicker. "Fabrication of smart parts using powder bed fusion additive manufacturing technology". In: *Additive Manufacturing* 10 (2016), pp. 58–66. DOI: 10.1016/j.addma.2016.01.001.

[A36] Vikram Iyer, Justin Chan, and Shyamnath Gollakota. "3D Printing Wireless Connected Objects". In: *ACM Trans. Graph.* 36.242 (2017). DOI: 10.1145/3130800.3130822.

[A37] Ron Jamieson and Herbert Hacker. "Direct slicing of CAD models for rapid prototyping". In: *Rapid Prototyping Journal* 1.2 (1995), pp. 4–12. DOI: 10.1108/13552549510086826.

[A38] Rhys Jones, Patrick Haufe, Edward Sells, Pejman Iravani, Vik Olliver, Chris Palmer, and Adrian Bowyer. "RepRap – The replicating rapid prototyper". In: *Robotica* 29.1 spec. issue (2011), pp. 177–191. DOI: 10.1017/S026357471000069X.

[A39] Andrew B. Kahng, Jens Lienig, Igor L. Markov, and Jin Hu. *VLSI Physical Design: From Graph Partitioning to Timing Closure*. Springer, 2011. DOI: 10.1007/978-90-481-9591-6.

[A40] Yoshihiro Kawahara, Steve Hodges, Benjamin S. Cook, Cheng Zhang, and Gregory D. Abowd. "Instant inkjet circuits: Lab-based Inkjet Printing to Support Rapid Prototyping of UbiComp Devices". In: *Proceedings of the ACM International Joint Conference on Pervasive and Ubiquitous Computing* (2013), pp. 363–372. DOI: 10.1145/2493432.2493486.

[A41] Mojtaba Khanzadeh, Prahalada Rao, Ruholla Jafari-Marandi, Brian K. Smith, Mark A. Tschopp, and Linkan Bian. “Quantifying Geometric Accuracy With Unsupervised Machine Learning: Using Self-Organizing Map on Fused Filament Fabrication Additive Manufacturing Parts”. In: *Journal of Manufacturing Science and Engineering* 140 (2017), p. 031011. DOI: 10.1115/1.4038598.

[A42] Chiyen Kim, Alejandro Cuaron, Mireya A. Perez, David Espalin, Eric MacDonald, and Ryan B. Wicker. “Cooperative Fabrication Methodology for Embedding Wire on Curved Surfaces”. In: *Proceedings of the International Solid Freeform Fabrication Symposium* (2014), pp. 185–196.

[A43] Chiyen Kim, David Espalin, Alejandro Cuaron, Mireya A. Perez, Eric MacDonald, and Ryan B. Wicker. “Unobtrusive In Situ Diagnostics of Filament-Fed Material Extrusion Additive Manufacturing”. In: *IEEE Transactions on Components, Packaging and Manufacturing Technology* 8.8 (2018), pp. 1469–1476. DOI: 10.1109/TCPMT.2018.2847566.

[A44] Min-Saeng Kim, Won-Shik Chu, Yun-Mi Kim, Adrian Paulo Garcia Avila, and Sung-Hoon Ahn. “Direct metal printing of 3D electrical circuit using rapid prototyping”. In: *International Journal of Precision Engineering and Manufacturing* 10 (5 2010), pp. 147–150. DOI: 10.1007/s12541-009-0106-0.

[A45] Felix Kolwa. “A computer vision Based pick and place solution for 3D printers”. Bachelor Thesis. University of Hamburg, 2019. URL: https://tams.informatik.uni-hamburg.de/publications/2019/BSc_Felix_Kolwa.pdf.

[A46] Yong Lin Kong, Ian A. Tamargo, Hyoungsoo Kim, Blake N. Johnson, Maneesh K. Gupta, Tae-wook Koh, Huai-an Chin, Daniel A. Steingart, Barry P. Rand, and Michael C. McAlpine. “3D Printed Quantum Dot Light-Emitting Diodes”. In: *Nano Letters* 14.12 (2014), pp. 7017–7023. DOI: 10.1021/nl5033292.

[A47] Thomas Krebs and Blaženk Šegmanović. “Integrating the CAD Worlds of Mechanics and Electronics with NEXTRA”. In: (2013). Ed. by Josip Stjepandić, Georg Rock, and Cees Bil, pp. 777–788. DOI: 10.1007/978-1-4471-4426-7_66.

[A48] Dennis Krupke, Florens Wasserfall, Norman Hendrich, and Jianwei Zhang. “Printable modular robot: an application of rapid prototyping for flexible robot design”. In: *International conference on Climbing and Walking Robots (CLAWAR)*. 2014.

[A49] Dennis Krupke, Florens Wasserfall, Norman Hendrich, and Jianwei Zhang. “Printable modular robot: an application of rapid prototyping for flexible robot design”. In: *Industrial Robot: An International Journal* 42.2 (2015), pp. 149–155. DOI: 10.1108/IR-12-2014-0442.

[A50] Sen Wai Kwok, Kok Hin Henry Goh, Zer Dong Tan, Siew Ting Melissa Tan, Weng Weei Tjiu, Je Yeong Soh, Zheng Jie Glenn Ng, Yan Zhi Chan, Hui Kim Hui, and Kuan

Eng Johnson Goh. “Electrically conductive filament for 3D-printed circuits and sensors”. In: *Applied Materials Today* 9 (2017), pp. 167–175. DOI: 10.1016/j.apmt.2017.07.001.

[A51] Jean-Claude Latombe. *Robot motion planning*. Boston: Kluwer, 1991.

[A52] J Ledesma-Fernandez, C Tuck, and R Hague. “High Viscosity Jetting of Conductive and Dielectric Pastes for Printed Electronics”. In: *Proceedings of the 26th International Solid Freeform Fabrication Symposium* (2015), pp. 40–55.

[A53] Yung-Cheng Lee. “An Algorithm for Path Connections and Its Applications”. In: *IRE Transactions on Electronic Computers* EC-10.3 (1961), pp. 346–365. DOI: 10.1109/TEC.1961.5219222.

[A54] Simon J. Leigh, Robert J. Bradley, Christopher P. Purssell, Duncan R. Billson, and David A. Hutchins. “A Simple, Low-Cost Conductive Composite Material for 3D Printing of Electronic Sensors”. In: *PLoS ONE* 7.11 (Nov. 2012). DOI: 10.1371/journal.pone.0049365.

[A55] Ji Li, Yang Wang, Gengzhao Xiang, Handa Liu, and Jiangling He. “Hybrid Additive Manufacturing Method for Selective Plating of Freeform Circuitry on 3D Printed Plastic Structure”. In: *Advanced Materials Technologies* 4.2 (2019), pp. 1–10. DOI: 10.1002/admt.201800529.

[A56] Amit Joe Lopes, Eric MacDonald, and Ryan B. Wicker. “Integrating stereolithography and direct print technologies for 3D structural electronics fabrication”. In: *Rapid Prototyping Journal* 18 (2012), pp. 129–143. ISSN: 1355-2546. DOI: 10.1108/13552541211212113.

[A57] Lu Lu, Jian Zheng, and Sandipan Mishra. “A Layer-to-Layer Model and Feedback Control of Ink-Jet 3D Printing”. In: *IEEE/ASME Transactions on Mechatronics* 20 (2015), pp. 1056–1068. DOI: 10.1109/TMECH.2014.2366123.

[A58] Vladimir J. Lumelsky and Alexander A. Stepanov. “Path-Planning Strategies for a Point Mobile Automaton Moving Amidst Unknown Obstacles of Arbitrary Shape”. In: *Algorithmica* (1987), pp. 403–430.

[A59] Eric MacDonald, Rudy Salas, David Espalin, Mireya Perez, Efrain Aguilera, Dan Muse, and Ryan B. Wicker. “3D Printing for the Rapid Prototyping of Structural Electronics”. In: *IEEE Access* (Mar. 2014), pp. 234–242. DOI: 10.1109/ACCESS.2014.2311810.

[A60] Eric MacDonald and Ryan Wicker. “Multiprocess 3D printing for increasing component functionality”. In: *Science* 353 (2016), aaf2093–aaf2093. DOI: 10.1126/science.aaf2093.

[A61] Richard Olivas, Rudy Salas, Dan Muse, Eric MacDonald, Ryan Wicker, Mike Newton, and Ken Church. "Structural Electronics through Additive Manufacturing and Micro-Dispensing". In: *International Symposium on Microelectronics* 2010.1 (2010), pp. 940–946. DOI: 10.4071/isom-2010-tha5-paper6.

[A62] Neeraj Panhalkar, Ratnadeep Paul, and Sam Anand. "A Novel Additive Manufacturing File Format for Printed Electronics". In: *ASME 2013 International Mechanical Engineering Congress and Exposition* (2013), pp. 1–7. DOI: 10.1115/IMECE2013-64678.

[A63] Judea Pearl. *Heuristics: Intelligent Search Strategies for Computer Problem Solving*. Boston, MA, USA: Addison-Wesley Longman Publishing Co., Inc., 1984. ISBN: 0-201-05594-5.

[A64] Blake K. Perez and Christopher B. Williams. "Combining Additive Manufacturing and Direct Write for Integrated Electronics – A Review". In: *Proceedings of the International Solid Freeform Fabrication Symposium* (2013), pp. 962–979.

[A65] Raf Ramakers, Kashyap Todi, and Kris Luyten. "PaperPulse: An Integrated Approach for Embedding Electronics in Paper Designs". In: *Proceedings of the 33rd Annual ACM Conference on Human Factors in Computing Systems - CHI '15* (2015), pp. 2457–2466. DOI: 10.1145/2702123.2702487.

[A66] Stephen J. Rock and Michael. J. Wozny. "Utilizing Topological Information to Increase Scan Vector Generation Efficiency". In: *Proceedings of the International Solid Freeform Fabrication Symposium* (1991).

[A67] H.-J. Rothermel and D. A. Mlynski. "Automatic Variable-Width Routing for VLSI". In: *IEEE Transactions on Computer-Aided Design of Integrated Circuits and Systems* 2.4 (1983), pp. 271–284. DOI: 10.1109/TCAD.1983.1270045.

[A68] Roozbeh (Ross) Salary, Jack P. Lombardi, Prahalad K. Rao, and Mark D. Poliks. "Online Monitoring of Functional Electrical Properties in Aerosol Jet Printing Additive Manufacturing Process Using Shape-From-Shading Image Analysis". In: *Journal of Manufacturing Science and Engineering* 139.10 (2017), p. 101010. DOI: 10.1115/1.40 36660.

[A69] Roozbeh (Ross) Salary, Jack P. Lombardi, M. Samie Tootooni, Ryan Donovan, Prahalad K. Rao, Peter Borgesen, and Mark D. Poliks. "Computational fluid dynamics modeling and online monitoring of aerosol jet printing process". In: *Journal of Manufacturing Science and Engineering* 139.2 (2017), p. 021015. DOI: 10.1115/1.4034591.

[A70] John Sarik, Alex Butler, Nicolas Villar, James Scott, and Steve Hodges. "Combining 3D printing and printable electronics". In: *TEI 2012 Works in Progress*. ACM, 2012.

[A71] Valkyrie Savage, Ryan Schmidt, Tovi Grossman, George Fitzmaurice, and Björn Hartmann. "A Series of Tubes : Adding Interactivity to 3D Prints Using Internal Pipes".

In: *Proceedings of the 27th annual ACM symposium on User interface software and technology* (2014). DOI: 10.1145/2642918.2647374.

[A72] Martin Schmitz, Mohammadreza Khalilbeigi, Matthias Balwierz, Roman Lissermann, Max Mühlhäuser, and Jürgen Steimle. "Capricate: A Fabrication Pipeline to Design and 3D Print Capacitive Touch Sensors for Interactive Objects". In: *Proceedings of the 28th Annual ACM Symposium on User Interface Software & Technology - UIST '15* (2015), pp. 253–258. DOI: 10.1145/2807442.2807503.

[A73] Edward Sells and Adrian Bowyer. *Rapid Prototyped Electronic Circuits*. Tech. rep. University of Bath, Department of Mechanical Engineering, 2004.

[A74] Corey Shemelya, Luis Banuelos-chacon, Adrian Melendez, Craig Kief, David Espalin, and Ryan Wicker. "Multi-functional 3D Printed and Embedded Sensors for Satellite Qualification Structures". In: *2015 IEEE SENSORS* (2015), pp. 1–4. DOI: 10.1109/ICSENS.2015.7370541.

[A75] Roland Siegwart. *Introduction to autonomous mobile robots*. 2nd edition. Cambridge, Massachusetts: MIT Press, 2011.

[A76] Nandkumar Siraskar, Ratnadeep Paul, and Sam Anand. "Adaptive Slicing in Additive Manufacturing Process Using a Modified Boundary Octree Data Structure". In: *Journal of Manufacturing Science and Engineering* 137 (2015), p. 011007. DOI: 10.1115/1.4028579.

[A77] George O. Smith. *Venus Equilateral*. Ballantine Books, 1947.

[A78] P. J. Smith, D.-Y. Shin, J. E. Stringer, B. Derby, and N. Reis. "Direct ink-jet printing and low temperature conversion of conductive silver patterns". In: *Journal of Materials Science* 41.13 (2006), pp. 4153–4158. DOI: 10.1007/s10853-006-6653-1.

[A79] Christian Staudigel, Matthias Hoffmann, Georg Schwalme, Ulrich Mohr-Matuschek, and Peter Heidemeyer. "Additive Manufacturing of Electric Circuits Based on Graphene Polymer Nanocomposites". In: *Proceedings of the 12th International Congress of Molded Interconnect Devices (MID)* (2016), pp. 2–6.

[A80] Neil Stephenson. *The Diamond Age*. Bantam Books, 1995.

[A81] Jeremy Straub. "Initial work on the characterization of additive manufacturing (3D printing) using software image analysis". In: *Machines* 3.2 (2015), pp. 55–71.

[A82] Jonathan Stringer, Talal M. Althagathi, Christopher C.W. Tse, Van Duong Ta, Jonathan D. Shephard, Emre Esenturk, Colm Connaughton, Thomas J. Wasley, Ji Li, Robert W. Kay, and Patrick J. Smith. "Integration of additive manufacturing and inkjet printed electronics: a potential route to parts with embedded multifunctionality". In: *Manufacturing Review* 3 (2016). DOI: 10.1051/mfreview/2016011.

[A83] John P. Swensen, Lael U. Odhner, Brandon Araki, and M. Aaron. “Injected 3D Electrical Traces in Additive Manufactured Parts with Low Melting Temperature Metals”. In: *Proceedings of the International Conference on Robotics and Automation (ICRA)*. 2015, pp. 988–995. DOI: 10.1109/ICRA.2015.7139297.

[A84] Tung D Ta, Fuminori Okuya, and Yoshihiro Kawahara. “LightTrace : Auto-router for Designing LED Based Applications with Conductive Inkjet Printing”. In: *Proceedings of SCF* (2017). DOI: 10.1145/3083157.3083160.

[A85] M. Samie Tootooni, Ashley Dsouza, Ryan Donovan, Prahalad K. Rao, Zhenyu Kong, and Peter Borgesen. “Classifying the Dimensional Variation in Additive Manufactured Parts From Laser Scanned Three-Dimensional Point Cloud Data Using Machine Learning Approaches”. In: *Journal of Manufacturing Science and Engineering* 139 (2017), p. 091005. DOI: 10.1115/1.4036641.

[A86] Spyros G. Tzaphestas. *Introduction to mobile robot control*. 1st edition. Amsterdam: Elsevier, 2014.

[A87] Bala R. Vatti. “A Generic Solution to Polygon Clipping”. In: *Communications of the ACM* 35.7 (1992), pp. 56–63. ISSN: 0001-0782. DOI: 10.1145/129902.129906.

[A88] T. Wasley, J. Li, D. Ta, J. Shephard, J. Stringer, P. Smith, E. Esenturk, C. Connaughton, and R. Kay. “Additive Manufacturing of High Resolution Embedded Electronic Systems”. In: *Proceedings of the 26th Annual International Solid Freeform Fabrication Symposium* (2016), pp. 1838–1855.

[A89] Florens Wasserfall. “Adaptive Slicing Algorithmen für Low-Cost 3D-Drucker mit mehreren Extrudern”. Master Thesis. University of Hamburg, 2014. URL: https://tams.informatik.uni-hamburg.de/publications/2014/adaptive_slicing_wasserfall.pdf.

[A90] Florens Wasserfall. “Embedding of SMD populated circuits into FDM printed objects”. In: *Proceedings of the 26th International Solid Freeform Fabrication Symposium*. Austin, 2015, pp. 180–189.

[A91] Florens Wasserfall. “Topology-Aware Routing of Electric Wires in FDM-Printed Objects”. In: *Proceedings of the 29th International Solid Freeform Fabrication Symposium*. Austin, 2018, pp. 1649–1659.

[A92] Florens Wasserfall, Daniel Ahlers, Norman Hendrich, and Jianwei Zhang. “3D-Printable Electronics - Integration of SMD Placement and Wiring into the Slicing Process for FDM Fabrication”. In: *Proceedings of the 27th International Solid Freeform Fabrication Symposium*. Austin, 2016, pp. 1826–1837.

[A93] Florens Wasserfall, Norman Hendrich, and Daniel Ahlers. “Optical In-Situ Verification of 3D-Printed Electronic Circuits”. In: *Proceedings of the 15th IEEE Conference on Automation Science and Engineering (CASE)*. Vancouver, 2019, pp. 1302–1307.

[A94] Florens Wasserfall, Norman Hendrich, Fabian Fiedler, and Jianwei Zhang. “3D-Printed Low-Cost Modular Force Sensors”. In: *Proceedings of the 20th Intl. Conference on Climbing and Walking Robots (CLAWAR)*. Porto, 2017, pp. 485–492. ISBN: 978-981-3231-03-0.

[A95] Florens Wasserfall, Norman Hendrich, and Jianwei Zhang. “Adaptive Slicing for the FDM Process Revisited”. In: *Proceedings of the 13th IEEE Conference on Automation Science and Engineering (CASE)*. Xi’an, 2017, pp. 49–54. DOI: 10.1109/COASE.2017.8256074.

[A96] Ryan B. Wicker, Francisco Medina, Eric MacDonald, Danny W. Muse, and David Espalin. “Methods and Systems For Connecting Inter-Layer Conductors and Components in 3D Structures, Structural Components, and Structural Electronic, Electromagnetic and Electromechanical Components/Devices”. US20140268607A1. 2016.

[A97] Ryan B. Wicker, Francisco Medina, Eric MacDonald, Danny W. Muse, and David Espalin. “Methods and Systems For Embedding Filaments in 3D Structures, Structural Components, and Structural Electronic, Electromagnetic and Electromechanical Components/Devices”. US20140268604A1. 2014.

[A98] Ran Zhang. “A Study of Routing Algorithms for PCB Design”. PhD thesis. Waseda University, 2016.

[A99] Zicheng Zhu, Vimal G. Dhokia, Aydin Nassehi, and Stephen T. Newman. “A review of hybrid manufacturing processes – state of the art and future perspectives”. In: *International Journal of Computer Integrated Manufacturing* 26.7 (2013), pp. 596–615. DOI: 10.1080/0951192X.2012.749530.

List of Web-Adresses

[B1] *Autodesk Project Wire*. Accessed: July 2018. URL: https://spark.autodesk.com/blog/autodesk-and-voxel8-make-3d-printed-electronics-reality/.

[B2] *Boost Graph Library documentation*. Accessed: January 2019. URL: https://www.boost.org/doc/libs/1_69_0/libs/graph/doc/.

[B3] *Bread slicer Github repository*. Accessed: October 2018. URL: https://github.com/nick-parker/Bread/.

[B4] Andres Campos and Victor Lamoine. *ros_additive_manufacturing project documentation*. Accessed: October 2018. URL: http://wiki.ros.org/ros_additive_manufacturing/.

[B5] *CuraEngine Github repository*. Accessed: October 2018. URL: https://github.com/Ultimaker/CuraEngine/.

[B6] *ECAD/MCAD Collaboration website*. Accessed: February 2019. URL: http://http://ecad-mcad.org.

[B7] Enrique. *Skeinforge toolchain documentation*. Accessed: May 2019. URL: https://reprap.org/wiki/Skeinforge/.

[B8] Ing. Buero Friedrich. *Target3001! product website*. Accessed: February 2019. URL: https://www.ibfriedrich.com/en/.

[B9] MECADTRON GmbH. *Nextra product website*. Accessed: February 2019. URL: http://www.mecadtron.de.

[B10] Gina Häußge. *Octoprint project website*. Accessed: September 2018. URL: https://octoprint.org.

[B11] Hot-World GmbH & Co. KG. *Repetier firmware Github repository*. Accessed: September 2018. URL: https://github.com/repetier/Repetier-Firmware/.

[B12] Autodesk Inc. *EAGLE product website*. Accessed: November 2018. URL: https://www.autodesk.com/products/eagle/overview/.

[B13] Voxel8 Inc. *Voxel8 company website*. Accessed: June 2019. URL: https://www.voxel8.com.

[B14] Angus Johnson. *Clipper Polygon Bibliothek*. Accessed: October 2018. URL: http://www.angusj.com/delphi/clipper.php.

[B15] Sylvain Lefebvre, Salim Perchy, and Cédric Zanni. *IceSL slicer project website*. Accessed: May 2019. URL: https://icesl.loria.fr.

[B16] Marius Kintel. *OpenScad CAD software project website*. Accessed: July 2019. URL: http://http://www.openscad.org.

[B17] *MatterSlice Github repository*. Accessed: October 2018. URL: https://github.com/MatterHackers/MatterSlice/.

[B18] Multi3D LLC. *Electrifi conductive filament product website*. Accessed: June 2019. URL: https://www.multi3dllc.com/product/electrifi/.

[B19] Neotech AMT GmbH. *Neotech AMT company website*. Accessed: June 2019. URL: http://www.neotech-amt.com.

[B20] Jason von Nieda. *Openpnp project website*. Accessed: September 2019. URL: http://openpnp.org.

[B21] *Open Source Hardware Definition*. Accessed: August 2018. URL: https://www.oshwa.org/definition/.

[B22] Optomec Inc. *Optomec company website*. Accessed: June 2019. URL: https://www.optomec.com/printed-electronics/aerosol-jet-technology/.

[B23] Amit Patel. *Amit's Thoughts on Pathfinding*. Accessed: May 2019. URL: https://theory.stanford.edu/~amitp/GameProgramming/.

[B24] RepRap Project. *RepRap original host and slicer repository*. Accessed: May 2019. URL: https://github.com/reprap/host/.

[B25] Protoplant Inc. *Proto-pasta conductive filament product website*. Accessed: June 2019. URL: https://www.proto-pasta.com/collections/exotic-composite-pla/products/conductive-pla.

[B26] Alessandro Ranellucci. *Slic3r project website*. Accessed: August 2018. URL: http://slic3r.org.

[B27] RoboCup Federation. *RoboCupSoccer Humanoid League*. Accessed: June 2019. URL: https://www.robocup.org/leagues/3/.

[B28] Shadow Robot Company. *Shadow Robot company website*. Accessed: August 2019. URL: https://www.shadowrobot.com.

[B29] *Slic3r Prusa Edition Github repository*. Accessed: October 2018. 2018. URL: https://github.com/prusa3d/Slic3r/.

[B30] The Spaghetti Detective. *The Spaghetti Detecitve product website*. Accessed: July 2019. URL: https://www.thespaghettidetective.com.

[B31] University of Hamburg. *Crossmodal Learning (CML) project website*. Accessed: August 2019. URL: https://www.crossmodal-learning.org.

[B32] Florens Wasserfall. *Modified Repetier firmware for our Demonstrator platforms*. Accessed: September 2018. URL: https://github.com/platsch/RepRap-Industrial-Firmware/tree/reprap-industrial-PNP/.

[B33] Florens Wasserfall. *OctoPNP Github repository*. Accessed: September 2018. URL: https://github.com/platsch/OctoPNP/.

[B34] Florens Wasserfall. *OctoPrint Autocalibration Github repository*. Accessed: September 2018. URL: https://github.com/platsch/OctoPrint-Autocalibration/.

[B35] Florens Wasserfall and Daniel Ahlers. *Repository with hardware modifications and components for the demonstrator platform printers*. Accessed: September 2019. URL: https://github.com/platsch/RepRapPNP/.

[B36] Florens Wasserfall and Daniel Ahlers. *Slic3r Electronics Github Repository*. Accessed: June 2019. URL: https://github.com/platsch/Slic3r/.

[B37] Florens Wasserfall and Dennis Struhs. *OctoCameraDocumentation Github repository*. Accessed: April 2019. URL: https://github.com/platsch/OctoPNP/.

List of Figures

List of Tables

Glossary

ABS Acrylonitrile Butadiene Styrene

CAD Computer Aided Design

CNC Computerized Numerical Control

CSG Constructive Solid Geometry

DXF Drawing Exchange Format

EBM Electron Beam Melting

eCAD electronic Computer Aided Design

mCAD mechanic Computer Aided Design

DFS Depth First Search

DLP Digital Light Processing

DOD Drop On Demand

FDM Fused Deposition Modelling

FFF Fused Filament Fabrication

ICA Isotropic Conductive Adhesive

ILP Integer Linear Programming

IMU Inertial Measurement Unit

MID Molded Interconnect Device

PA PolyAmide

PCB Printed Circuit Board

PCL PolyCaproLactone

PETG PolyEthylene Terephthalate Glycol

PID Proportional Integral Derivative

PLA	Polylactic Acid
PP	Polypropylene
ROS	Robot Operating System
RSMT	Rectilinear Steiner Minimal Tree
RRR	Rip-Up and Reroute
SfS	Shape from Shading
SLA	Stereolithography
SLM	Selective Laser Melting
SLS	Selective Laser Sintering
SMD	Surface Mounted Device
STL	Surface Tesselation Language or Standard Triangulation Language
VLSI	Very Large Scale Integration

Eidesstattliche Erklärung

Hiermit erkläre ich an Eides statt, dass ich die vorliegende Dissertationsschrift selbst verfasst und keine anderen als die angegebenen Quellen und Hilfsmittel benutzt habe.
Ich versichere weiterhin, dass ich die Arbeit vorher nicht in einem anderen Prüfungsverfahren eingereicht habe und die eingereichte schriftliche Fassung der Fassung auf dem elektronischen Speichermedium entspricht.

Hamburg, den 8. Oktober 2019

Unterschrift